ANL-IFR-125

Integral Fast Reactor
Integral Fast Reactor
Integral Fast Reactor
Integral Fast Reactor
Integral Fast Reactor
Integral Fast Reactor
Integral Fast Reactor
Integral Fast Reactor
Integral Fast Reactor
Integral Fast Reactor
Integral Fast Reactor
Integral Fast Reactor
Integral Fast Reactor
Integral Fast Reactor
Integral Fast Reactor
Integral Fast Reactor
Integral Fast Reactor
Integral Fast Reactor
Integral Fast Reactor
Integral Fast Reactor
Integral Fast Reactor
Integral Fast Reactor
Integral Fast Reactor
Integral Fast Reactor
Integral Fast Reactor
Integral Fast Reactor
Integral Fast Reactor
Integral Fast Reactor
Integral Fast Reactor
Integral Fast Reactor
Integral Fast Reactor

IFR

Integral Fast Reactor Program
Summary Progress Report
FY 1985-FY 1989

Argonne National Laboratory, Argonne, Illinois 60439
operated by The University of Chicago
for the United States Department of Energy under Contract W-31-109-Eng-38

IFR Technical Memorandum
Results reported in the IFR-TM series of memoranda frequently are preliminary and subject to revision. Consequently they should not be quoted or referenced.

Integral Fast Reactor
Integral Fast Reactor
Integral Fast Reactor
Integral Fast Reactor
Integral Fast Reactor
Integral Fast Reactor
Integral Fast Reactor
Ir

January 1990 ANL-IFR-125

INTEGRAL FAST REACTOR PROGRAM
SUMMARY PROGRESS REPORT
FY 1985-FY 1989

Argonne National Laboratory
9700 South Cass Avenue
Argonne, IL 60439

Y. I. Chang	General Manager, IFR Program
L. C. Walters	Associate Program Director for Fuels
J. E. Battles	Associate Program Director for Pyroprocess
D. R. Pedersen	Associate Program Director for Safety
D. C. Wade	Associate Program Director for Core Design
M. J. Lineberry	Associate Program Director for Fuel Cycle

IFR TECHNICAL MEMORANDUM NO. 125

Results reported in the IFR-TM series of memoranda frequently are preliminary and subject to revision. Consequently they should not be quoted or referenced.

TABLE OF CONTENTS

TABLE OF CONTENTS
(Contd.)

TABLE OF CONTENTS
(Contd.)

LIST OF FIGURES

LIST OF FIGURES
(Contd.)

LIST OF FIGURES
(Contd.)

LIST OF TABLES

LIST OF TABLES
(Contd.)

INTEGRAL FAST REACTOR PROGRAM
SUMMARY PROGRESS REPORT
FY 1985-FY 1989

ABSTRACT

This report summarizes highlights of the technical progress made in the Integral Fast Reactor (IFR) Program from its inception through the end of FY 1989, with emphasis on more recent technical accomplishments. Technical accomplishments are presented in the following areas of the IFR technology development activities: (1) metal fuel performance, (2) pyroprocess development, (3) safety experiments and analyses, (4) core design development, and (5) fuel cycle demonstration.

I. IFR PROGRAM OVERVIEW

The Integral Fast Reactor (IFR) is an advanced reactor concept which capitalizes on the characteristics of metallic fuel and liquid metal cooling to offer significant improvements in reactor safety, operation, fuel cycle economics, environmental protection, and safeguards. This innovative concept, being developed at Argonne National Laboratory, has become the focus of the Civilian Reactor Development Program of the Department of Energy. Its primary features are being demonstrated in the facilities at ANL-West, utilizing EBR-II and the associated fuel cycle facility as an IFR prototype.

There are a number of technical features of the IFR which contribute collectively to its potential as a next-generation reactor. The IFR employs liquid metal cooling, which offers large safety margins and permits operation at low system pressures. This enables use of a pool-type reactor design configuration, with the large reservoir of coolant providing significant thermal inertia to accommodate a variety of off-normal events involving the heat transport system. The IFR fuel is a metallic fuel, which provides high fissile atom density, high thermal conductivity, and superior compatibility with the liquid metal coolant. The use of metallic fuel in turn makes possible the utilization of innovative fuel cycle processes (termed "pyroprocessing") which will permit fuel cycle closure with compact, low-cost reprocessing facilities, collocatable with the reactor plant if desired. The pyroprocessing method, in addition to its potential economic advantages, also makes the IFR responsive to long-term waste management issues: pyroprocessing involves only a few waste packaging operations, and actinide recycling is an inherent part of the fuel cycle.

Although based in large part on the technology which has resulted in the successful operation of Experimental Breeder Reactor II (EBR-II) for over 25 years, the IFR technology is new in many respects. When the IFR concept was conceived in the latter part of FY-1984, the IFR technology development and demonstration were planned in the following three phases, as shown in the overall program schedule, Fig. I.1.

Phase I:	Technical Feasibility	FY 1984-1986
Phase II:	Technology Development	FY 1987-1990
Phase III:	Technology Demonstration	FY 1991-1995

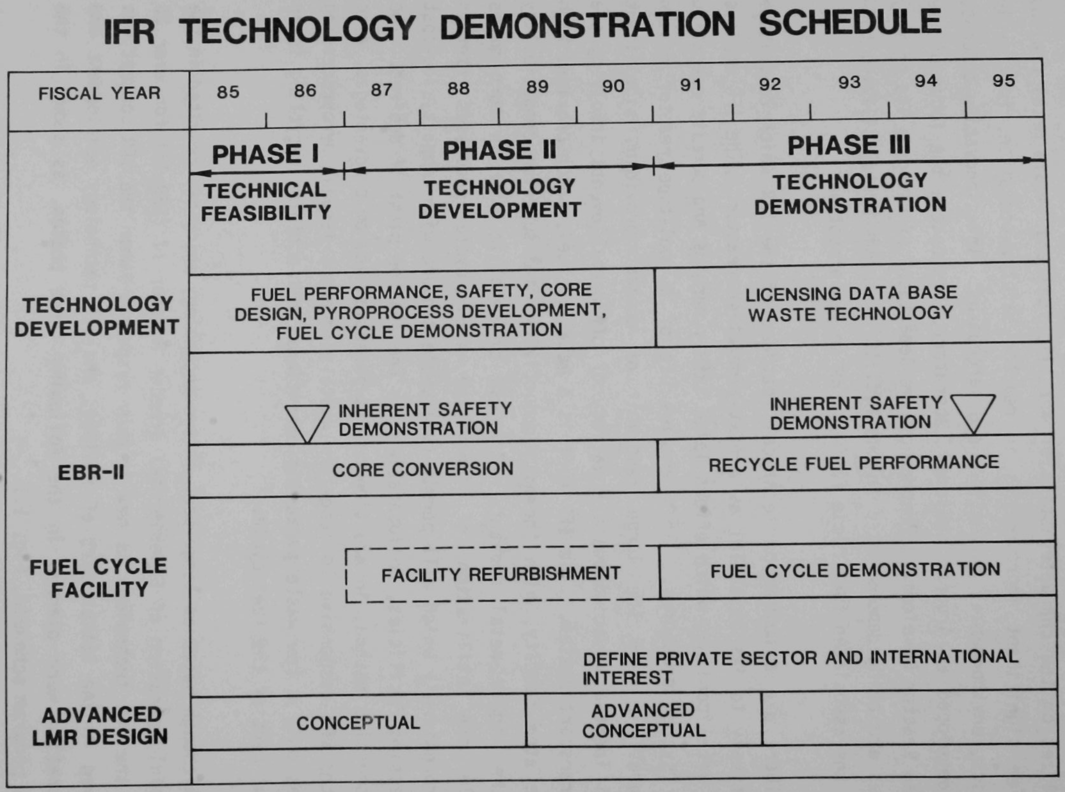

Fig. I.1. Overview Program Schedule for the Integral Fast Reactor Program

The goal during Phase I was to establish the technical feasibility of the concept. Phase I consisted largely of scoping tests, analyses and critical reviews, intended primarily to establish conclusively the feasibility of the concept.

During this period a landmark series of demonstration tests was carried out with EBR-II, clearly showing the passive inherent safety advances achievable with the IFR. Steady-state and transient testing of metallic fuels in EBR-II and TREAT further demonstrated the potential for improved reactor performance, both in normal and off-normal operation modes. Laboratory-scale experiments with pyroprocessing operations proved the feasibility of the electrorefining and injection casting processes. Reactor design studies resulted in the adoption of the key IFR features in the PRISM and SAFR design concepts. This was given additional credence with the findings of an independent, top-level review committee which asserted the technical feasibility of the IFR and recommended continued development as a high-priority effort. The University of Chicago Special Committee for the IFR concluded:

> "The Committee believes that the IFR concept is a highly attractive LMR concept which, if pursued effectively, could restore the leadership role and preeminence of the United States in the fast reactor field. More importantly, it believes that the IFR concept offers the potential for achieving greater safety and better economics than any other LMR reactor concept being considered anywhere in the world today. It enthusiastically and without reservation endorses continuation of the Phase I program into Phase II."

Major accomplishments during Phase I included:

- Feasibility demonstration of electrorefining on a laboratory scale.
- Inherent safety demonstration tests in EBR-II.
- Adaptation of the IFR concept in PRISM and SAFR designs.

The successful conclusion of the Phase I feasibility demonstration was followed by initiation of Phase II of the IFR Program, which is the period during which the detailed technology is being developed to enable a subsequent full-scope demonstration (Phase III). The Phase II technology development activities deal with all aspects of the IFR technology, from reactor design to waste disposal. Particular emphasis is placed on the characterization and performance evaluation for the binary and ternary (U-Zr and U-Pu-Zr) IFR fuel compositions. Also receiving major programmatic emphasis is work related to the design and testing of engineering-scale pyroprocessing unit operations systems, including electrorefining, fuel fabrication, pyroprocess flowsheet optimization, and waste management processes. Phase II activities include major facility modifications, principally in the Hot Fuel Examination Facility/South (HFEF/S) hot cells, to prepare for the demonstration phase. HFEF/S was originally constructed as the EBR-II Fuel Cycle Facility. Because EBR-II reactor operations comprise an important part of the integrated IFR technology demonstration, work in the reactor operations area continues to be directed toward evolution of IFR operational practices, incorporating advanced instrumentation and control systems technologies.

Phase II work in core design points toward further enhancement of core design and analysis capabilities and to the development of designs or operating strategies which utilize most effectively the unique features of the IFR. In preparation for increased activity in the area of safety analyses and interactions with licensing authorities, efforts are being extended during Phase II to update the safety data base and analytical models, with added emphasis placed on analysis of severe accident initiating events and consequences.

Major accomplishments expected during Phase II include:

- Demonstration of high burnup potential and fuel performance characterization.
- Engineering-scale demonstration of electrorefining.
- Development of safety data base to support PRISM interactions with NRC.
- EBR-II core conversion with the IFR U-Zr and U-Pu-Zr fuels.
- Refurbishment of the original EBR-II Fuel Cycle Facility (HFEF/S).

A final review of the accomplishments of Phase II and the status of the required technology development will be held at the end of FY-1990, whereafter the demonstration phase will begin. Further technology development requirements and activities will be dictated by experience accruing from the technology demonstration during Phase III of the Program.

Phase III, the IFR technology demonstration, is the most important period for the Program, because it is in this stage that the individual aspects of the IFR technology will be brought together and integrated to prove the overall systems performance. This phase of the Program will be centered upon the extended operation of EBR-II with IFR fuel. Core conversion is now complete, and the reactor is now operating with IFR fuel having a variety of fuel and cladding compositions. Reactor operation will provide a substantial fuel performance data base for future utilization. The spent fuel will be subjected to the full spectrum of pyroprocessing operations, using engineering-scale unit operations equipment installed in the modified Fuel Cycle Facility (FCF) at the ANL-W site. The performance of recycled fuel will be evaluated by irradiation of a number of EBR-II fuel subassemblies fabricated in the FCF with fuel compositions typical of steady-state recycle operation, and the influence of this fuel on various reactor passive inherent safety characteristics will be assessed by direct measurements. Waste handling and treatment practices representative of future IFR plant operations will be developed and tested as well during this demonstration phase.

A continuing activity during Phase III will be continued technical support of detailed design efforts, safety analyses, and licensing interactions for the Advanced LMR. Active interfaces will be maintained with design organizations for effective responsiveness to arising technical issues. Design of a commercial fuel cycle facility will proceed apace with the industrial reactor design activities, with a conceptual design for such a facility to be available by the end of FY-1991 for use in commercialization strategy planning.

Upon completion of Phase III, the IFR technology will be fully developed for commercial application. It is anticipated that during this period an Advanced LMR demonstration project will be formulated and that the IFR Program activities will then be integrated into such a project.

The end products of the IFR Program, scheduled to be completed by the end of FY-1995 as shown in Fig. I.1, are as follows:

- Fuel performance demonstration of recycled IFR fuel alloys up to 150,000 MWd/T burnup level.
- Demonstration of inherent safety potential of the IFR concept through actual EBR-II plant tests with recycled IFR fuels.
- Demonstration of the entire IFR fuel cycle on a prototype scale.
- Substantial progress in IFR waste form certification.
- Demonstration of actinide recycle capability.
- Licensing data base in support of the Advanced LMR project interactions with NRC.

II. METAL FUEL PERFORMANCE

A. Fuels Development Program

Metal fuel is key to realizing the safety potential of the IFR. In addition, metal fuel makes practical the compact pyroprocess fuel cycle. Therefore, the development of a complete technical data base on metal fuel performance is an essential element of the IFR program. The scope of this program includes an irradiation test program, which covers a wide range of design and operating conditions, and an out-of-reactor test and analytical program designed to establish the in-depth understanding of fuel performance for reactor design and licensing.

Early work on development of metal fuel for fast reactors was sponsored by the Atomic Energy Commission. Work involving plutonium metal fuels, however, was terminated in 1969. Even by that time, though, a number of important design features and performance characteristics had been established. To achieve high burnup, it was shown both theoretically and by experiment that a small reduction in smear density from 85% to about 75%, would allow release of fission gas by the time the fuel had swollen in contact with the cladding. The mechanism for the release was the interconnection of fission gas bubbles allowing a continuous flow path to an appropriately-sized plenum such that the gas pressure in the fuel element remained reasonably low. The porous fuel resulting after gas release not only provided a flow path for fission gas, but in addition, the porous fuel could plastically deform rather than stress the cladding as solid fission products accumulated.

An adequate solidus temperature of the fuel and compatibility of the fuel with the cladding were issues where some progress had been made in the 1960's. A uranium-plutonium alloy with a substantial plutonium content has both a low solidus temperature (melting temperature) and has the propensity to alloy with cladding components, such as iron, to form low melting eutectic compositions. A number of third element additions to the uranium/plutonium system were investigated as a means of solving the concerns. It was found that zirconium addition was somewhat unique in that both the solidus temperature of the fuel increased, and the compatibility of fuel with cladding was enhanced.

Irradiation tests of a number of U-Pu-Zr alloys with various cladding materials were conducted in the 1960's, but the program was terminated before the fuel elements could reach high burnup. Only a few fuel elements reached burnups as high as 6 at.%. Even though the burnup values were not high, the important performance features of expected gas release and lack of fuel cladding mechanical interaction were observed.

Some work on metal fuel development continued at EBR-II, since it continued to be fueled with metal. The EBR-II driver fuel used throughout the 1970's and early 1980's, was uranium - 5 wt % Fs*. Slight changes in design were instituted to achieve higher burnup with the major change being the conversion from the higher smear density (85%) MK-IA fuel to the lower smear density (75%) MK-II fuel that resulted in more than a factor of three increase in burnup to the range of 11 at.%. During this period more than 100,000 metallic fuel elements were irradiated in EBR-II under an extensive surveillance program that yielded substantial performance information.

Thus, when the IFR program was initiated and R&D was to resume on U-Pu-Zr fuel, a significant data base existed consisting of information from the late 1960's on U-Pu-Zr and other plutonium-containing alloys, and a great deal of fabrication and performance information on the U-5 wt % Fs EBR-II driver fuel.

At the beginning of the IFR program in 1984, the highest priority fuels activity was to begin to build a data base on the plutonium-bearing U-Pu-10 w/o Zr fuels. This first required construction of a glovebox facility in which such fuels could be fabricated, since the facilities available earlier had been dismantled. The Experimental Fuels Laboratory (EFL) was completed in 1984. The glove box contained a small injection-casting furnace, capable of casting about 10 fuel slugs from a 1 kg crucible charge, and all the equipment necessary to process the fuel slugs and load them into stainless-steel cladding. One of the early successes in the EFL was the injection casting of U-Pu-Zr fuel slugs from a crucible charge that was melted directly from the three individual elements. In the 1960's it was thought necessary to

---

*Fissium (Fs) is a mixture of alloying elements consisting of 2.4 wt % Mo, 1.9 wt % Ru, 0.3 wt % Rh, 0.2 wt % Pd, 0.1 wt % Zr, and 0.01 wt % Nb to obtain a total of 5 wt % of Fs in the fuel U-5Fs.

construct a U-Pu-Zr crucible charge from the two binary alloys, U-Pu and U-Zr, in order to prevent volatilization of the plutonium. In a short time, casting parameters were estabished that would yield homogeneous, full-length, U-Pu-Zr fuel slugs. Three lead EBR-II assemblies, which contained U-Pu-Zr fuel from the EFL, began their irradiation in February 1985. Since that time more than 40 irradiation tests with IFR fuel have been put under irradiation in EBR-II and FFTF. The EFL has supplied U-Pu-Zr fuel for a number of out-of-reactor property studies, as well.

Thus far, the irradiation test program has included a comprehensive range of design and operating parameters. The U-Pu-Zr fuel composition has varied from no plutonium to 28 wt % plutonium with zirconium variation from 2 to 14 wt %. Three cladding materials have been used, which include the two austenitic claddings, 316 and D9, and the ferritic cladding, HT9. In addition, the plenum-to-fuel ratio, smear density, linear power, and fuel and cladding temperatures have covered a wide range. The maximum burnup achieved to date is 18.4 at.%, which far exceeds that achieved earlier in the 1960's and is certainly comparable to other LMR fuel types. In general, the steady-state irradiation performance has been excellent.

The irradiation test program and out-of-reactor tests and analyses include an important component aimed at off-normal performance of the fuel. Fuel behavior after cladding breach as well as fuel performance during reactor transients and beyond-design-basis events require in-depth understanding.

The main question associated with off-normal performance is the temperature at which a liquid phase forms between fuel and cladding, and the rate at which cladding is penetrated once a liquid phase forms. This question is being studied in detail by several techniques. Sections of irradiated fuel and cladding are heated at various times and temperatures to determine the onset of melting and the penetration kinetics over a range of variables, including different fuel and cladding combination, steady-state burnup, and prior steady-state irradiation temperature. These studies will be complemented by tests where entire irradiated fuel elements will be heated in a furnace above the temperatures where a liquid phase forms between fuel and cladding.

The following sections discuss the progress made to date in some of the most important areas of the metallic fuel development program.

B. Steady-state Irradiation Performance

Initial performance testing of IFR fuel elements began in February 1985 with the irradiation of three 61-element subassemblies, X419, X420, and X421. With numerous interim reconstitution and postirradiation examinations (PIE), these lead tests have reached burnup levels of 11.9, 17.1, and 18.4 at.%, respectively, thus exceeding their design burnup of 10 at.%. The fuel tested included U-xPu-10Zr (x = 0, 8, 19 wt %), clad in 5.8 mm (0.23 in.) diameter, 20% CW D9. Fuel microstructure, fission gas release behavior, swelling, chemical redistribution, and cladding strains have been characterized as a function of burnup and fuel type. Fuel swelling and fractional gas release have similar burnup dependencies: a rapid rise to ~2% burnup when the clad/fuel gap closes, followed by a slowly increasing linear region out to the highest burnup measured (18%). The large fuel-to-plenum volume ratio in these aggressively-designed elements produces high plenum pressures, and so the peak cladding diametral strain increases rapidly from ~1% at 10% burnup to ~6.5% at 18% burnup. The fractional gas release asymptotically approaches ~80% at high burnup and is not a strong function of fuel type. Fuel swelling and chemical restructuring are Pu dependent, however, as discussed in a later section of this report.

A total of nine upper-weld breaches have occurred in the D9 clad elements in subassemblies X420 and X421 at burnups ranging from 13.5 to 17 at.%. A stress concentrator, which formed between the fusion zone of the TIG weld and the cladding inner wall, was found to be a crack initiator. End-plug redesign effectively eliminated this problem for later TIG-closure welds though a longer plenum section would certainly have extended the lifetimes. Subassembly X420 also suffered an additional four failures outside of the weld region at burnups between 15 and 17%. A fuel column breach just above core midplane in a U-19Pu-10Zr element at 16.8 at.% burnup produced the usual tag and fission gas signals, as well as delayed-neutron (DN) signals. While destructive PIE on this small crack has not yet begun, it appears that the DN signal (~20 min in duration) was not associated with significant fuel loss to the coolant but from the expulsion of DN emitters in the element bond sodium.

Three other failures occurred during the same reactor run and were presumably associated with a small crack in the plenum ~10 cm below the upper weld. Because X420 contained a large fraction of highly-strained elements, bundle-duct interaction or reconstitution damage may be a contributor to these breaches. All 13 of the metal-fuel breaches incurred in these two lead tests were totally benign in nature. Operation in the breach mode throughout the reactor run had no impact on reactor operation.

The lead HT9-clad experiment in EBR-II was subassembly X425. Consistent fuel behavior was observed with minimal cladding strain at 10% burnup (~0.4% $\Delta D/D_0$). No breaches have occurred to the current burnup level of 15.4 at.%.

A series of EBR-II experiments are being run to test specific effects of certain operating variables like fuel composition, smear density and cladding temperature. The X423 test included Pu contents ranging from 0 to 26 wt % and was used to characterize the progression of swelling and chemical restructuring from low to intermediate burnup (~0.5 to 5%). The low fuel and cladding operating temperature slowed chemical redistribution (interchange of U and Zr), and thereby eliminated the usual strong effect which Pu content has on axial growth.

The X430 test (now at 6.9 at.% burnup without breach) extends the HT9-clad-fuel data base to prototypical 7.4 mm (0.29 in.) diameter elements with high Pu contents (0, 19, 22, and 26 wt %). Laboratory furnace tests of the high Pu fuel preirradiated in X430 will determine their performance under high temperature off-normal events and will lead to a better understanding of low-melting eutectic formation in irradiated fuel.

In order to benchmark the metallic fuel performance code "LIFEMETAL", key operating variables have been systematically varied in the X441 experiment (now at 11.07 at.% burnup with no breach). Smear density has been varied (70%, 80%, and 85%), as well as fuel composition (U-19Pu-6, -10, -14Zr).

Because the HT9 alloy shows limited strength and may exhibit reduced fuel/clad compatibility at high temperature, a 660°C beginning-of-life (BOL) peak inside cladding temperature (PICT) was chosen for the X447 experiment (now at 6.5 at.% burnup with no breach). PIE at 4.7 at.% burnup showed ~100 μ of fuel/clad interaction and ~0.8% diametral strain in the hottest region of the cladding.

Large diameter blanket elements (9.4 mm. diameter) are now under irradiation in the X431/X432 tests. Low enrichment slugs of U-2Zr, U-6Zr, and U-10Zr were clad in HT9 at two levels of smear density (85 and 90%). These 19-element subassemblies have performed satisfactorily to date and are now at ~1.3 at.% burnup.

In order to generate a statistically significant data base with which to judge IFR-fuel reliability, the standard EBR-II driver-fuel alloy, "U-5Fs," has been steadily phased out even though fully reliable to its 8% burnup level. The EBR-II core conversion is now complete, using MK-III subassemblies of D9-clad, U-10Zr driver fuel, and 316 SS-clad U-10Zr safety/control rod fuel. The current MK-III driver-fuel burnup limit of 10% has been exceeded by X435 (13.5% burnup), one of the four qualification subassemblies.

Cladding availability prompted the next whole-core conversion to the 20% CW, 316 SS clad MK-IIIA fuel. Qualification testing with the four 61-element subassemblies has just begun in the EBR-II reactor. A parallel effort to qualify HT9 cladding (MK-IV) as a backup system is also under way. This effort will qualify not only U-10Zr clad in HT9 but provide U-26Pu-10Zr in HT9 cladding to ultimately be used as feedstock for the IFR fuel cycle demonstration.

Irradiation testing in FFTF was initiated to demonstrate that the data base generated with EBR-II's core height (34.3 cm) is directly applicable in gauging performance of commercial LMR cores approximately three times this height. Axial fuel growth might be expected to show some core-length dependence and was the main driving force for full-length element experiments in the FFTF. The irradiation testing of two 169-element experiments in FFTF is now complete. D9 cladding with U-0, -8, -19 Pu-10Zr fuel was tested in the IFR-1 subassembly, having reached its goal burnup of 10 at.%. HT9-clad U-10Zr fuel was tested to 4.8 at.% burnup in the MFF1A experiment. Neither test experienced breach and will soon undergo PIE. Follow-on tests of full length U-10Zr clad HT9 elements are now under irradiation at FFTF (MFF1, 2, 3, 4) and have achieved a maximum burnup of 9.0 at.% without breach.

In summary, the irradiation testing program to date has clearly demonstrated the feasibility of the IFR metallic-fuel system. Specific operating variables are now being tested, and fuel performance codes are being verified. Whole-core demonstrations of reliability are now in-process at EBR-II, while prototypic-sized elements show reliable performance at FFTF.

C. Run-Beyond-Cladding-Breach (RBCB) Performance

The RBCB program, used to test the performance of metallic fuel under breach conditions, utilizes artificially-induced breaches. This was accomplished by machining the cladding of a test element in a localized region and allowing it to breach under stress during irradiation.

Several tests were conducted using different fuel alloys of U-xPu-10Zr (x = 0-19 wt %) as well as D9 and Type-316 stainless-steel cladding materials (future tests will examine HT9 cladding). The initial scoping tests were designed around EBR-II driver fuel using 4.4 mm (0.174 in.) diameter fuel elements. Prototypical testing, upon completion of the scoping tests, used the IFR fuel design of 5.8 mm (0.23 in.) fuel element diameters. The test elements were previously irradiated to a range of burnups between 3 and 12 at.% burnup.

Steady-state irradiation and subsequent postirradiation-examination (PIE) of the RBCB tests have resulted in a large data base that has produced strong support of the fuel's predicted benign behavior under breach conditions. Table II.1 provides a description of the IFR RBCB program and its current status.

Analysis of the fuel system under breach conditions addressed several important items:

TABLE II.1. RBCB Test Program

	Scoping Tests			IFR Prototypical		
	XY-21/21A	XY-24	XY-27	X482	X428A	X---
Comp. (wt%)	U-5Fs	U-19 Pu-10 Zr	U-8 Pu-10 Zr	U-19 Pu-10 Zr	U-10 Zr	U-x Pu-10Zr
Cladding	316SS	316SS	316SS	D9	D9	D9
Burnup	-9.3 at.%	-7.5 at.%	-6.0 at.%	-12.2 at.%	-12.0 at.%	-12.0 at.%
Size	MK-II(0.130")	MK-II(0.130")	MK-II(0.130")	MK-III(0.173")	MK-III(0.173")	MK-III(0.173")
Run Time:						
Breached	54 days	233 days	131 days	168 days	Insert Runs 152-153	Insert Runs 154-155
MWD	3348	18,453	15,234	9200	---	---
Runs	136-139	143-146	144-146	149-150	152-153	154-155
Status	RT95 breached	J507 breached J516 no breached	J432 breached J486 breached	T139 breached	---	---
Wt Loss(g)	-2.0 g	2.7 g	-2.5 g/element	4.04 g	---	---
Facility	BFTF	FPTF	BFTF	Open Core	Open Core	Open Core

- Observe the RBCB characteristics of IFR metal fuel.
- Observe characteristics of the fuel/clad interaction of D9 and HT9 cladding under RBCB conditions.
- Characterize the delayed neutron and fission gas "signature" of a fuel column breach in an open core position.
- Characterize fission product release and fuel loss from elements during extended RBCB operation.

As indicated in Table II.1 artificially-induced breaches in the fuel column region of RBCB tests have operated in reactor for periods in excess of 200 days without deterioration of the breach site. Figure II.1 provides the basic release sequence of a breach in the fuel region.

In all the RBCB tests the same characteristic pattern was repeated in that only during the initial breach stage was any significant release of delayed-neutron precursor activity observed. After the sodium bond, cesium fission products, and accumulated fission gas expulsion, all activity ceased, with the exception of periodic small "burps" of gas.

Throughout the RBCB testing program, PIE of breached elements revealed that no crack widening and negligible fuel loss had occurred during the RBCB residence time. Figure II.2 shows a transverse metallographic section taken of the pre-thinned clad region of an IFR prototypical fuel element that underwent 170 days of irradiation after breach. Note that after the initial crack in the clad, no further widening had occurred.

The performance to date of IFR metallic fuel clearly indicates that this fuel system is reliable to high burnups and also shows negligible performance deterioration after element breach has occurred.

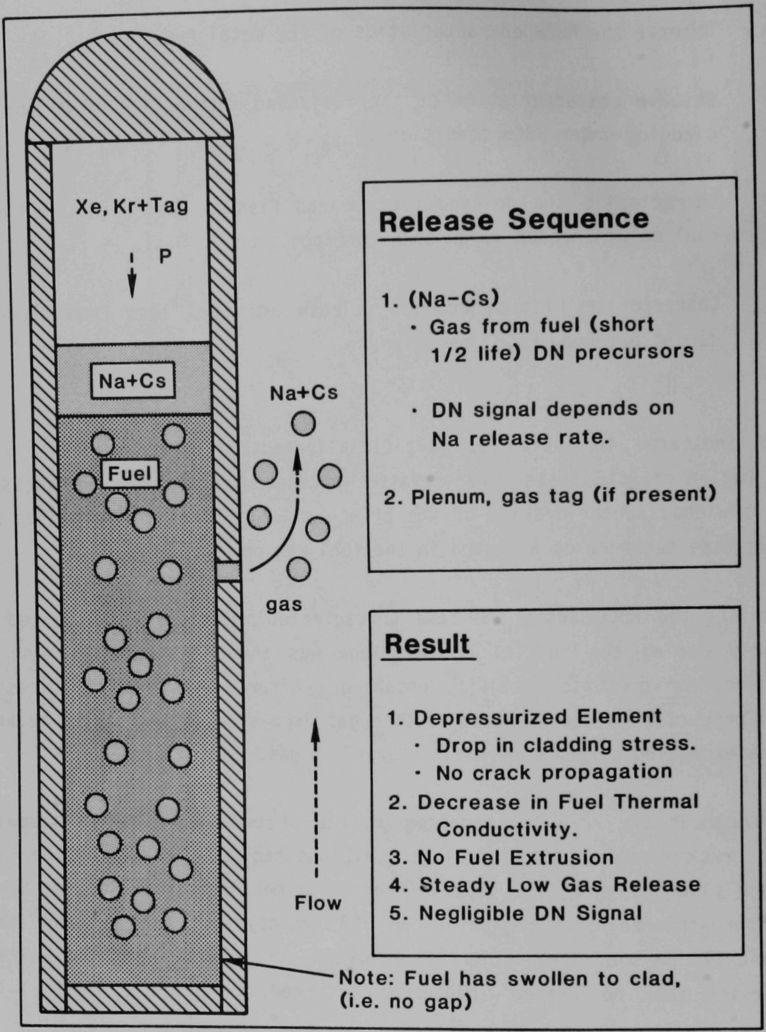

Release Sequence

1. (Na–Cs)
   - Gas from fuel (short 1/2 life) DN precursors
   - DN signal depends on Na release rate.
2. Plenum, gas tag (if present)

Result

1. Depressurized Element
   - Drop in cladding stress.
   - No crack propagation
2. Decrease in Fuel Thermal Conductivity.
3. No Fuel Extrusion
4. Steady Low Gas Release
5. Negligible DN Signal

Note: Fuel has swollen to clad, (i.e. no gap)

Fig. II.1. Breach Release Characteristics

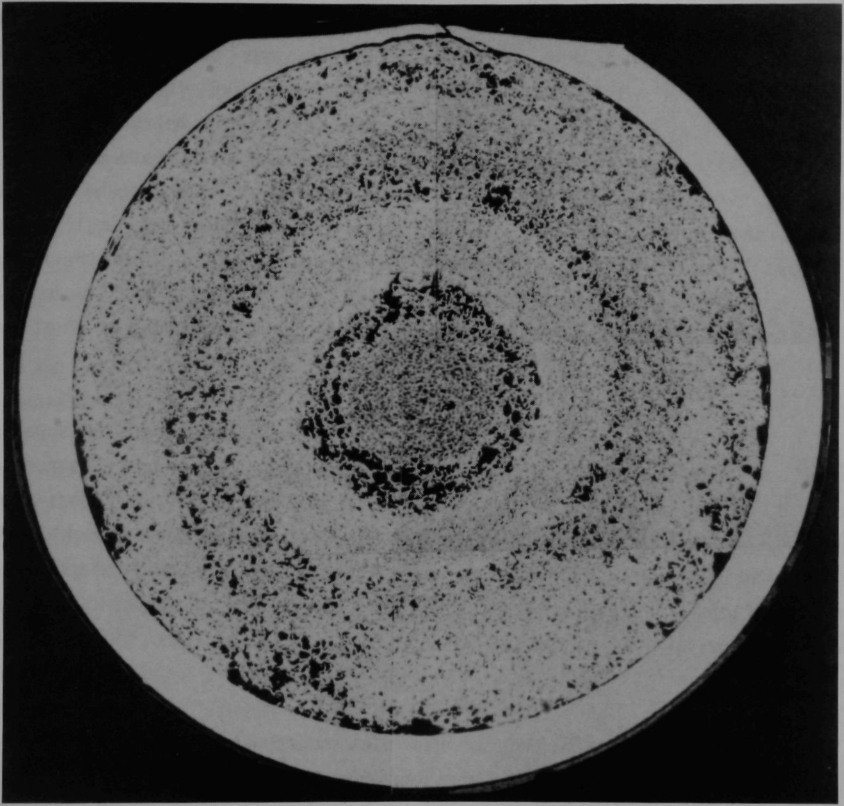

25X

Fig. II.2. Transverse Section of Pre-thinned Region Showing Small Crack after Breach. RBCB test ran for 170 days after breach with no further clad deterioration.

D. Fuel/Cladding Compatibility

The fuel element performance characteristics related to the chemical compatibility of fuel and cladding materials are attributable to two phenomena. These are the solid-state interdiffusion of fuel and cladding materials during steady-state operation, as well as the behavior of these interdiffusion layers when cladding and fuel temperatures increase during off-normal operation (loss-of-flow and over-power events). A long-standing issue has been the question whether interdiffusion compositions could melt during off-normal operation, and, if such an event occurs, how quickly the molten layer is able to penetrate the cladding. The word "eutectic" will be used to refer to these compositions and temperatures where mixtures of fuel and cladding are found to melt.

In the 1960's it was found that U-Pu-Zr alloys demonstrated a superior potential compared to other U-Pu-M (M = Ti, Mo, etc.) alloys for resistance of eutectic formation when fuel was brought into contact with stainless-steel cladding at elevated temperatures (>725°C). The reasons were thought to be related to the formation of Zr-rich layers at the fuel/cladding interface, or the elevation of eutectic temperatures by a Zr solute in Fe-Pu-U mixtures. This was one of the reasons that the U-Pu-Zr system was chosen as the reference for the IFR fuel system.

The current research program has been concerned with three areas of study. The first of these has been concerned with basic phase studies where fuel and cladding compositions are mixed in a differential thermal analysis (DTA) apparatus. Another group of tests used diffusion couples made with unirradiated pieces of fuel and cladding. Lastly, and most prototypic, has been the detailed analysis of segments of irradiated fuel elements. Compositions and thicknesses of fuel/cladding interdiffusion layers are measured. These same samples are also then heated to elevated temperatures to simulate off-normal conditions and to assess when eutectic melting would occur, and how much cladding is penetrated during the testing time. These latter tests are conducted in the Fuel Behavior Testing Apparatus (FBTA).

The examination of as-irradiated segments of fuel and cladding has shown that the solid-state interdiffusion of fuel and cladding is typically characterized chemically by the schematic representation shown below in Fig. II.3. The three layers found are (1) unreacted cladding, (2) a reacted layer in the cladding rich in lanthanide fission products (Ce, Nd, Sm, and La) depleted in cladding components (largely Fe and Ni), and (3) a fuel layer containing small amounts of cladding components (mostly Fe and Ni). Very little, if any fuel components (U, Pu, Zr) are found in the cladding. The reacted cladding layer is very hard and brittle and has been considered as cladding wastage in fuel performance models. The thickness of this layer increases as Pu is added to the fuel, can be as thick as 75 μm after 6-10 at.% burnup of the fuel, and does not seem to grow significantly as higher burnups are achieved.

The use of unirradiated fuel/cladding combinations had been used early in the development efforts, including diffusion couple testing in the 1960's. As further insight is gained concerning the nature of steady-state (solid-state) interactions, it is becoming questionable as to how prototypic these tests are of the off-normal performance of fuel elements. Nevertheless, these studies could provide insight into the basic mechanisms of fuel/cladding interaction if similar characteristics are observed in more prototypic tests using as-irradiated fuel and cladding combinations.

The DTA studies have used mixtures of U-xPu-10Zr (wt %) (x = 0, 8, 19, 26%) and 316, D9, and HT9 cladding materials. Diffusion couple tests have included U-xPu-yZr (x = 0-26% Pu, y = 6.3-14% Zr) with current testing confined to y = 10%, and 304, 316, D9, HT9, 9Cr-1Mo, and other assorted stainless-steel cladding materials. The intent of the tests was to investigate possible effects of the cladding compositions on eutectic formation (no such effect was found in the studies done to date). The initial DTA testing has consisted of heating the fuel/cladding mixtures until molten ($T > 1300°C$) to attain equilibrium and then cooling the mixture. This procedure causes relatively stable Fe-Zr compounds to form on cooling, and Zr therefore does not seem to contribute to increasing the eutectic temperature. Careful studies are now being done to assess whether the results are affected by the testing conditions. The equilibrium condition of the DTA tests may not be reached in an actual fuel element during irradiation. Thus, the stable Fe-Zr compounds may not form during irradiation to the extent found in the DTA tests.

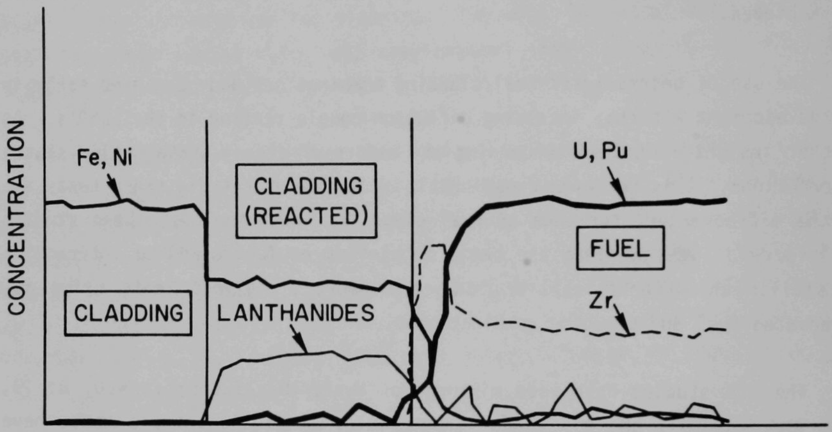

Fig. II.3. Stylized Representation of Solid-State Interaction Characteristics as Fuel and Cladding Interdiffuse

Ignoring the effects of zirconium, Fig. II.4 compares the results of diffusion couples with the DTA tests. Note that the diffusion couple tests generally have shown higher melting temperatures. The scatter in the diffusion couple results further indicates that the role of Zr is important; it can form a Zr-layer diffusion barrier between fuel and cladding, and/or act as a solute to modify the melting temperature of fuel/cladding compounds.

The more prototypic testing (FBTA) results have shown that the data base is not yet extensive enough to allow prediction of the behavior of any fuel/cladding combination, but in general demonstrate higher eutectic temperatures than the unirradiated test samples. Moreover, the limited testing indicates, surprisingly, that the Pu content of the fuel does not seem to lower the eutectic temperature.

Table II.2 shows the FBTA data which has been generated using samples taken from fuel elements with high plutonium contents. Note that the U-26Pu-10Zr/316 samples demonstrated good compatibility. No eutectic melting was observed at temperatures less than 800°C. The reasons for the superior compatibility are currently unknown, but eutectic melting at a very high fuel/cladding temperature was consistently demonstrated by the fuel elements. Identification of the factors producing the effect may be important for producing optimal performance in the fuel elements.

Eutectic melting can consistently be achieved at 800°C, and this temperature has initially been used to study cladding penetration rates. Scatter has been observed in the data for samples that had been irradiated under different conditions or using different fuel/cladding combinations. In general, however, the behavior is characterized by an initial rapid penetration followed by a decrease in the penetration rate.

In general, DTA test results have shown a lower onset of eutectic temperature between fuel and cladding than FBTA tests. As pointed out earlier, at equilibrium virtually all of the zirconium is tied up as stable Fe-Zr compounds. Thus, zirconium was not effective in increasing the eutectic temperature. Whether this condition would ever occur during irradiation of a fuel element is uncertain and will be addressed with long term and high

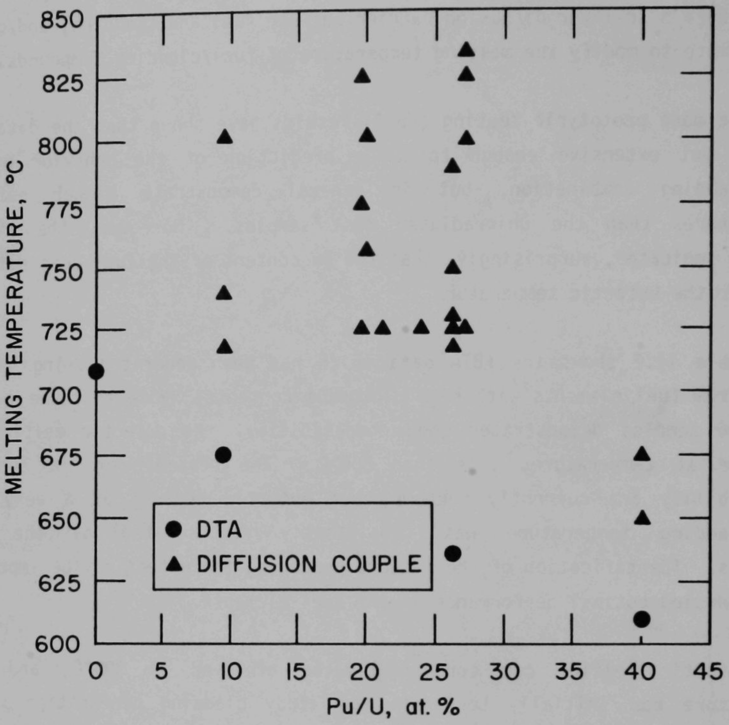

Fig. II.4. Comparison of DTA and Diffusion Couple Results. Note that the diffusion couple results represent Zr concentrations of 6.3 to 14 wt %.

TABLE II.2. Results of Fuel/Cladding Compatibility Tests in FBTA

Peak BU at.%	Test Temp. (°C)	Test Time (hr)	Max. Liq. Penetration (μm)	Penetration Rate (μm/s)
		U-26Pu-10Zr/316		
4.7	700	1.0	0.0	0
4.7	750	1.0	0.0	0
4.7	800	1.0	32.5	9.03×10^{-3}
4.7	850	1.0	75.0	2.08×10^{-2}
4.7	670	7.0	0.0	0
4.7	740	7.0	0.0	0
4.7	710	7.0	0.0	0
4.7	770	7.0	0.0	0
4.7	800	1.0	36.5	1.01×10^{-2}
4.7	800	2.0	56.5	7.85×10^{-3}
4.7	800	4.0	74.0	5.14×10^{-3}
4.7	800	0.4	24.0	1.67×10^{-2}
		U-19Pu-10Zr/HT9		
3.0	700	1.0	0.0	0
3.0	750	1.0	49.4	1.4×10^{-2}
3.0	780	1.0	62.7	1.7×10^{-2}

temperature tests both in-reactor and with ex-reactor furnace tests on whole elements.

FBTA testing will be used to identify the effects on eutectic temperature caused by irradiation condition (temperature, burnup, etc.) and of fuel and cladding composition. This is being done in an effort to understand and document how different fuel element designs may behave during off-normal events, and how the design may be used to prevent fuel/cladding eutectic formation. In addition, a test apparatus has recently been completed where an entire fuel element, previously irradiated in reactor, can be heated to simulate off-normal conditions and observe the time-to-failure characteristics. Also, in-reactor testing at elevated temperatures is planned. These tests (FBTA, whole-pin heating, and in-reactor) will be emphasized to develop performance codes and guidelines for operational limits. The tests using unirradiated fuel and cladding will be used to add fundamental understanding of observed phenomena.

E. Redistribution of Alloying Elements

The irradiation of U-Pu-Zr fuel produces significant radial redistribution of zirconium within the cylindrical fuel slug. The redistribution can result in radial zones of the slug depleted in zirconium content. The possible influences of this effect on the performance of the fuel are (1) a reduction in the melting (solidus) temperature of the fuel in depleted areas and (2) if depletion should occur next to the cladding, then the potential for fuel/cladding interaction could be enhanced.

The characteristics of Zr migration observed thus far have been (1) redistribution occurs significantly only in U-xPu-10Zr alloys where x is at least 15 wt %, (2) the higher the operating temperatures; or the greater the radial thermal gradients, the greater is the redistribution effect; (3) the fuel components (U, Pu, Zr) migrate so as to exchange U and Zr while the Pu content of the alloy remains relatively constant across the radius; and (4) the Zr-depleted regions form at the center of the fuel slug (two-zone segregation) or in the mid-radius area (three-zone segregation). The Zr-depleted area has never been found to form at the area near the fuel/cladding interface. Redistribution of fuel components is also characterized by well-defined porosity, or gas bubble, distributions in the fuel. These distributions form either concurrently with or prior to alloy redistribution. The correlation between fuel swelling and redistribution is also discussed in Section II.G.

Figure II.5 shows typical fuel element cross-sections in U-19 wt % Pu-10 wt % Zr where redistribution has occurred. Chemical analysis has indicated that the lightly-colored regions are generally depleted in zirconium. One of the most segregated samples tested showed a two-zone structure with the central, Zr-depleted areas having less than 2 wt % zirconium (see Fig.

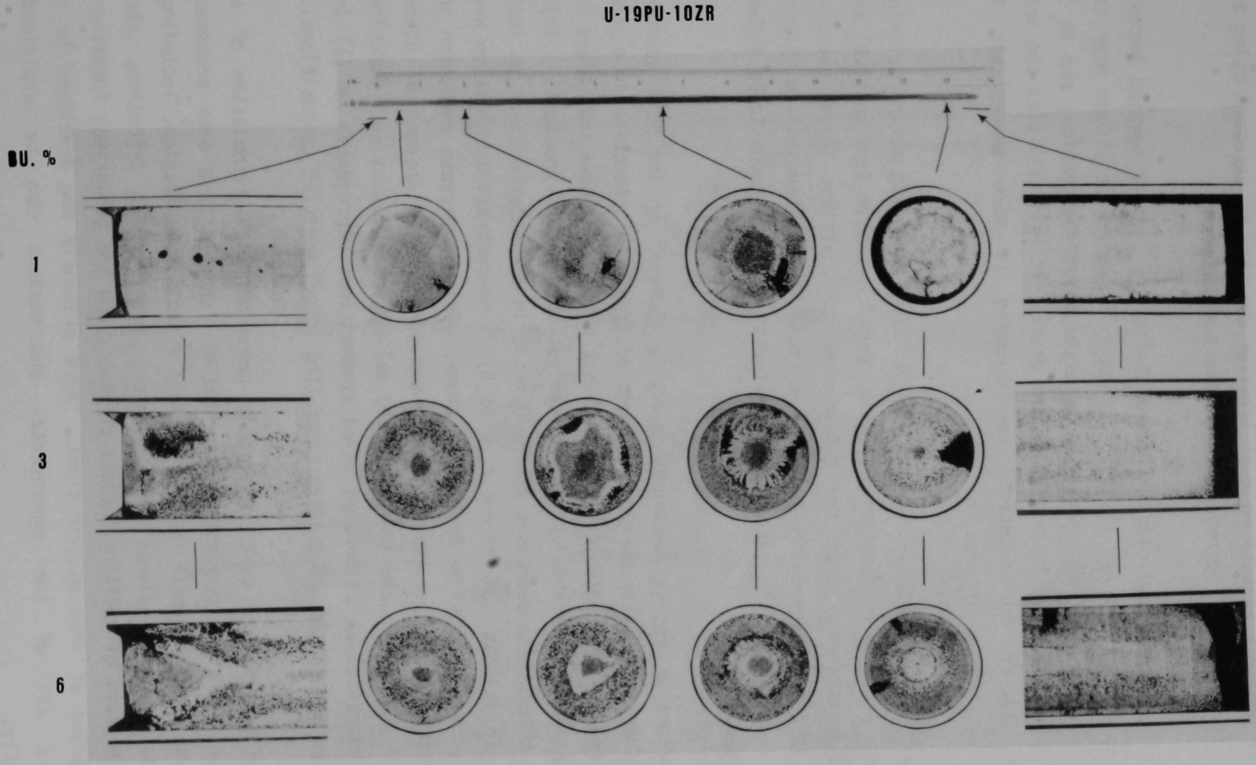

Fig. II.5. Photomicrographs of Irradiated U-19Pu-10Zr Fuel Showing the Characteristics of Alloy Redistribution

II.6). The possible effects on fuel behavior can then be assessed using the assumption that the most segregation possible has occurred.

The effect upon fuel/cladding compatibility is largely negated because Zr-depletion has never been observed to occur in radial positions near the cladding. However, radial cracking often accompanies segregation, and it is the low-Zr fuel which swells to fill in the crack. It is likely that the area where this low-Zr fuel contacts the cladding is more susceptible to fuel/cladding chemical interaction.

Segments of irradiated fuel elements have been subjected to high temperatures (>750°C) to simulate off-normal conditions (see Section II.D) and results have confirmed that the circumferential positions where eutectic formation is first observed are those where radial cracks have filled in with low-Zr fuel. However, the eutectic temperatures have been found to be higher than expected.

The effect of redistribution of alloying elements on the fuel solidus temperature was originally analyzed in terms of Zr-content reduction in a zone while keeping the Pu/U ratio constant. It has since been shown that U and Zr interchange while the absolute Pu concentration remains constant. This phenomenon effectively decreases the Pu/U ratio in Zr-depleted areas so that reductions in solidus temperature created by Zr-concentration reduction are not as great as expected by Zr removal alone. This is because reduction in the Pu/U ratio increases the solidus temperature in the absence of other effects. Figure II.7 shows the calculated solidus temperatures as a function of Zr concentration as calculated using compositions represented by (1) Zr removal alone and (2) Zr and U interchange (the actual measured compositions).

Present and future work is largely concerned with formulation of a physical model for the chemical redistribution. Models have been proposed previously which incorporate thermal gradient effects on diffusion, including chemical potential gradients and thermal flux induced diffusion, the mechanical effects of swelling-induced stresses, and the gas-driven formation and resintering of void distributions. None presently are developed to a stage where all of the experimental observations can be explained satisfactorily.

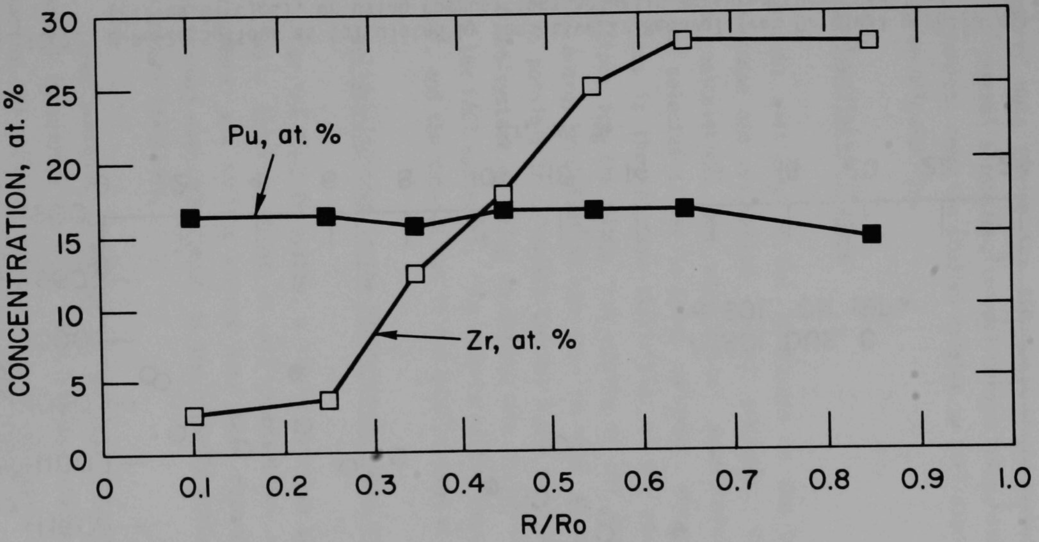

Fig. II.6. Radial Composition of a U-19Pu-10Zr Sample at 5.5% Burnup (Pu and Zr) Showing Zr Segregation with No Pu Segregation. Uranium concentrations show that mass balance is achieved by U and Zr exchange.

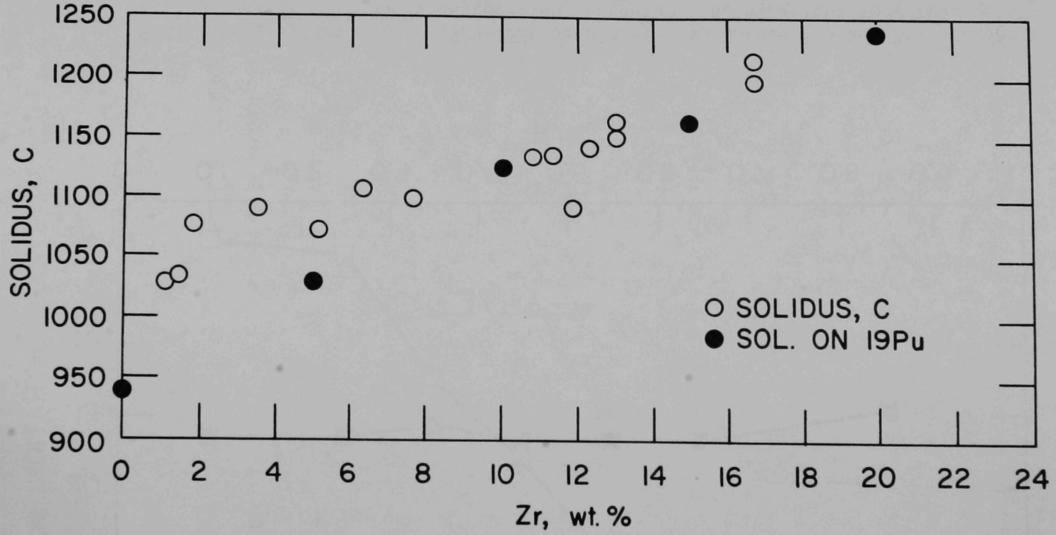

Fig. II.7. U-Pu-Zr Solidus as Calculated by Sensitive Zr Removal from Original U-Pu-Zr Alloy (Filled Circles), or Using Compositions Actually Measured (Open Circles).

F. Thermal and Physical Properties

This phase of the program was designed to provide the thermophysical and chemical property data needed for IFR fuel development. This includes: measurements of thermal expansion, thermal conductivity, and phase transition temperatures, chemical reaction studies related to fuel-cladding interactions, and phase-diagram calculations.

1. Phase Equilibrium Studies

The data available in the literature on the U-Pu-Zr system are inadequate in scope and reliability for our purposes. A dual approach of phase diagram calculations and experimental determination of transition temperatures for selected alloys is being employed. The thermodynamic basis of phase diagrams is the relative stabilities of all possible phases in a system. Equations for the Gibbs free energy of all competing phases are needed. Free energy minimization can then be used to calculate the phase diagram. It is possible to calculate ternary phase diagrams from data on the three binary sub-systems by using an appropriate mixing rule. This work is performed with the FACT system[1,2]. The efforts on the solidus-liquidus in the Pu-U-Zr system[3], and the sub-solidus in the U-Zr[4] system are summarized below.

a. Solidus-Liquidus in the Plutonium-Uranium-Zirconium System

For the Pu-U-Zr system, a liquid solution and a body-centered-cubic (BCC) solid solution exist at all compositions within the ternary system. Liquidus and solidus curves have been reported for all binary systems, but ternary data are scarce, as are reliable activity or calorimetric data on the binary solutions.

Free energies of fusion of the pure components U, Zr, and Pu were of central importance in these calculations. These were obtained from standard sources and could be selected reasonably easily for Zr and Pu. The data for uranium presented a difficulty, however, in that the value recommended by Oetting, et al.[5] gave poor agreement with the measured Pu-U phase diagram. Another published value[6] gave much better agreement with the Pu-U phase diagram. This presented a significant problem. On the one hand, two independent determinations of the Pu-U solidus were available. On the other hand, the recommended enthalpy of fusion seemed to be quite reliable. This dilemma was resolved in favor of the value recommended by Oetting et al., chosen because it gave better agreement with our solidus-liquidus measurements, and it seemed unlikely that the experimental enthalpy measurement would be so much in error.

The available literature on the binary systems was examined in this assessment and reasonable judgements were made of the most reliable information. With the FACT system, Gibbs energy equations were derived and used to calculate the ternary solidus-liquidus. Excess Gibbs energies in the ternary liquid and solid phases were calculated from the values for the three binary systems by means of the Kohler interpolation equation.

Calculated ternary isothermal sections are shown in Fig. II.8. Near the median of the composition triangle, error limits are estimated as ~75°C for the liquidus and ~125°C for the solidus. Comparison of the calculations with the few experimental values available generally gave agreement within the estimated uncertainty.

b. Thermodynamics of the Uranium-Zirconium System

Calculation of the sub-solidus phases in the Pu-U-Zr system requires thermodynamic functions for those phases in the three binary sub-systems. A study of the U-Zr system, the simplest and most important of the three, was begun. Relatively little thermodynamic data exist for the U-Zr system, and the analysis relied to a great extent on a critical assessment of the U-Zr phase diagram performed by Sheldon and Peterson[4].

The solubility of Zr in U(α) or U(β) is very low. Similarly, solubility of U in Zr(α) is very low. These three phases have been treated as Henrian solid solutions. The two BCC phases, U(γ) and, Zr(β), form a solid solution phase in which a miscibility gap exists. An intermediate phase also exists. This phase has been treated with a quasi-chemical model.

Henry's law coefficients were calculated for the U(α), U(β), and Zr(α) phases from the appropriate phase boundaries. For each of these phases,

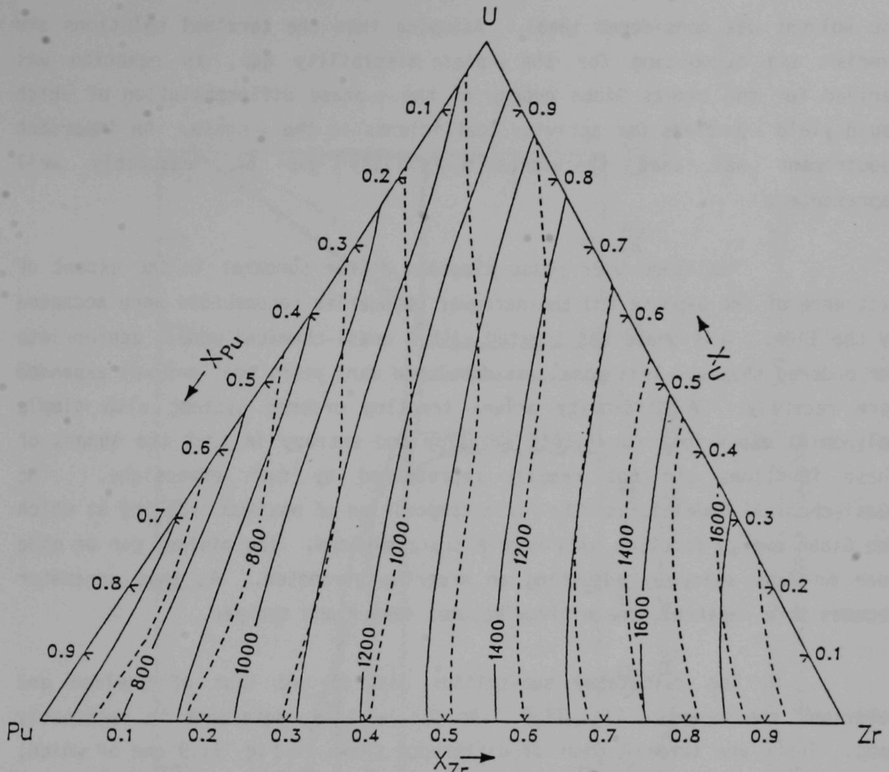

Fig. II.8. Calculated Pu-U-Zr Liquidus (Solid Lines) and Solidus (Broken Lines) in 100°C Intervals the solvent was considered ideal. Assuming that the terminal solutions are Henrian and accounting for the γ-phase miscibility gap, an equation was derived for the excess Gibbs energy of the γ-phase differentiation of which would yield equations for activity coefficients in the γ-phase. An important requirement was that the γ-phase miscibility gap be reasonably well represented.

Published U-Zr phase diagrams differ somewhat in the extent of existence of the ∂-phase and the narrower boundaries recommended were accepted by the IAEA. This phase was treated with a quasi-chemical model, appropriate for ordered phases. This model was developed many years ago[7] and was expanded more recently. A difficulty arises treating ordered systems with simple polynomial expansions for excess enthalpy and entropy in that the shapes of these functions are not readily represented by such expansions. The quasi-chemical model is used to fix a composition of maximum ordering at which the Gibbs energy function will have a sharp minimum. The minimum can be made more or less sharp by adjusting an ordering parameter. As this parameter becomes more negative, the minimum becomes deeper and sharper.

The calculated sub-solidus diagram and that of Sheldon and Peterson[4] are shown in Fig. II.9. As can be seen, agreement is reasonably good. There are several areas of difference shown in Fig. II.9 one of which, the extent of the ∂-phase has already been discussed. Other areas of disagreement have to do with the limiting slopes of the phase boundaries. It is known that for a melting transition, for example, as the composition approaches a pure component, the difference between the slopes of the liquidus and solidus curves is determined by just the enthalpy of fusion and the melting point of that component independent of any model. A similar equation relates the limiting slopes for solid-state phase transformations to the enthalpy and temperature of transformation of the pure component. The calculated diagram shows the correct limiting slopes, whereas the diagram of Sheldon and Peterson differs somewhat from the theoretical values in some cases. Overall, that the calculated diagram is believed to be a good representation of the true phase equilibrium.

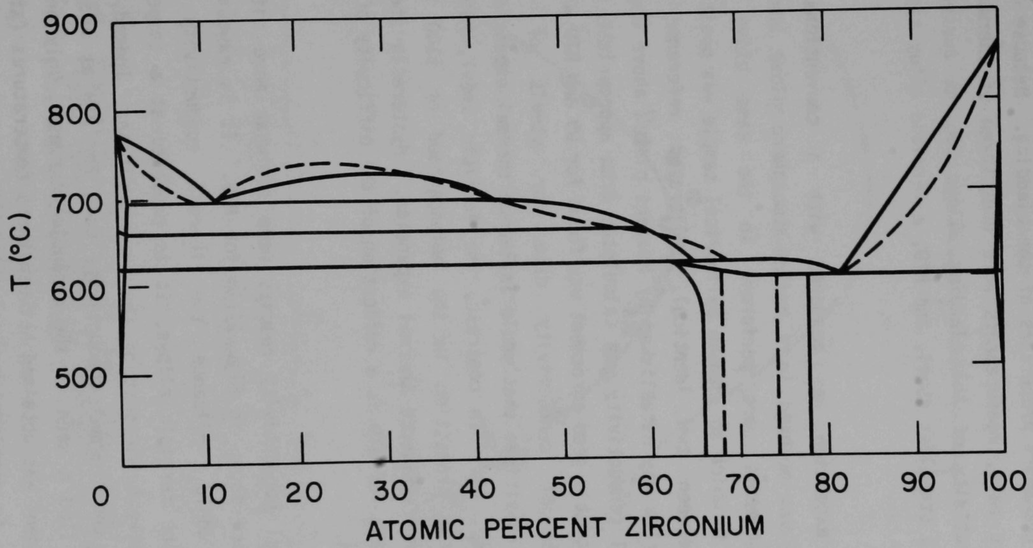

Fig. II.9. Comparison of Calculated (Ref. 3, Solid Lines) and Literature (Ref. 4, Broken Lines) U-Zr Phase Diagrams

2. Thermal Expansion and Thermal Conductivity of D9 and HT9

Modeling of fuel performance depends, in part, on knowledge of the thermodynamic and transport properties of the cladding. Because of a lack of reliable literature data, measurements were undertaken of thermal expansion and thermal conductivity of the cladding alloys D9, an austenitic steel similar to Type-316 stainless steel, and HT9, a ferritic alloy similar to 400 series steels.

Thermal expansion was measured with a conventional push-rod dilatometer, which was mounted in a helium-atmosphere glove box. Thermal conductivity measurements were performed in the same glove box by a comparative method in which an unknown cylindrical sample was positioned under spring tension between two identical, calibrated reference cylinders. Longitudinal heat flow was established by heaters placed above and below the column, and thermal conductivity was calculated from appropriate temperature measurements. Reasonably good agreement was found for D9 and HT9 with thermal expansion and thermal conductivity data for steels of comparable composition[8]. No transitions that would influence thermal expansion occur in the austenitic alloy, D9. In contrast, the ferritic steel, HT9, shows a ferritic-to-austenitic transition in the neighborhood of 1100 K. Curie transitions would not influence thermal expansion. Hysteresis shown by the thermal expansion data for HT9 is a reflection of the difficulty of reversing the phase transition.

The thermal conductivity results were somewhat more difficult to interpret. These are shown in Fig. II.10 for HT9. It is expected that a Curie transition would influence the thermal conductivity at high temperatures. In the ferritic alloys, it is expected at a temperature of about 1040 K, slightly below that of the $\alpha \rightarrow \gamma$ transition. Indeed, a marked break was found in the thermal conductivity data for HT9 at about 1030 K rather than at the 1100 K seen in the expansion curves. Only one thermal conductivity measurement was obtained between these temperatures (at 1071 K), and it is impossible to distinguish between the effects of the (α to γ) and the Curie transitions on thermal conductivity. It is possible that the thermal expansion transition at 1100 K was slightly delayed. Data have been presented[9] for thermal expansion and thermal conductivity of the steel alloys

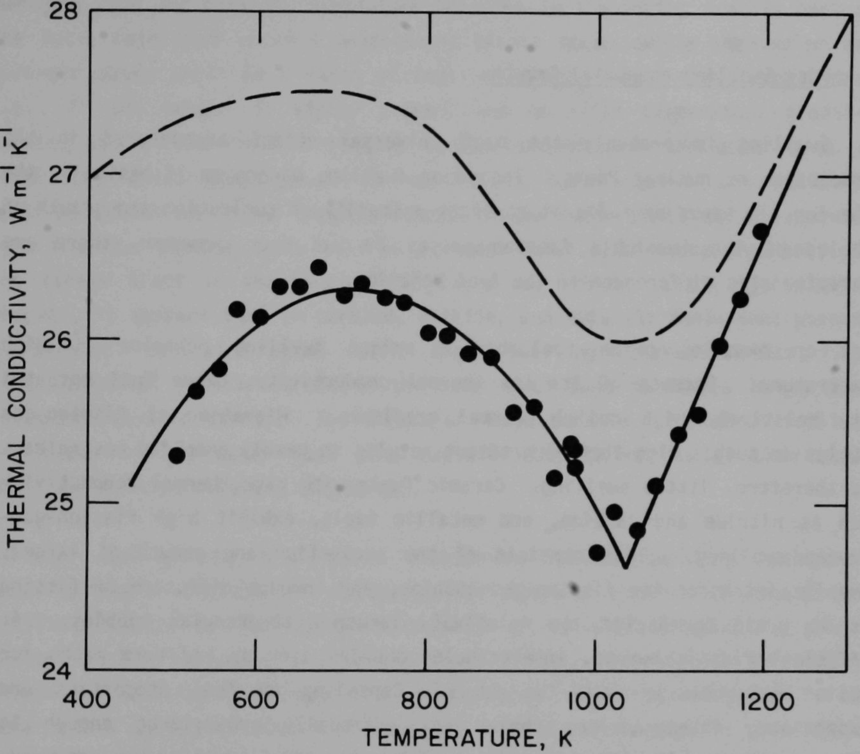

Fig. II.10. Thermal Conductivity of HT9. Experimental points and fit (solid line) from Ref. 9; literature values (broken line) provided by Sandvik Steel Co.

D9 and HT9. The austenitic alloy, D9, shows values for both thermal expansion and thermal conductivity typical of 316 stainless steel. The ferritic alloy, HT9, however, shows a 1030 K phase transition. Assessments of its behavior under severe, unexpected conditions, such as hypothetical beyond design basis accidents, must take this transition into account.

G. Fuel Swelling and Axial Growth

Swelling is probably the most universal effect encountered in the irradiation of nuclear fuels. The major swelling mechanism is basically the same for all types of fuel; it consists primarily of nucleation and growth of bubbles of the insoluble fission gasses Xe and Kr. However, there are characteristic differences in the fuel behavior.

For example, oxide fuel has a unique swelling behavior at high temperature. Because of its low thermal conductivity, oxide fuel operates with relatively high radial thermal gradients. Migration of fission-gas bubbles in such a high thermal gradient results in nearly complete gas release and therefore, little swelling. Ceramic fuels with high thermal conductivity such as nitride and carbide, and metallic fuels, exhibit high fission-gas-induced swelling. This consists of the nucleation and growth of largely immobile intragranular fission-gas bubbles, and through diffusion of fission gas to grain boundaries, in relatively larger intergranular bubbles. At sufficient fissile burnup, intergranular bubbles link up and form paths for fission gas release from the fuel. Depending on fuel properties and temperature, intragranular bubbles may eventually grow large enough to interconnect as well. At this point, a large amount of swelling has occurred, and therefore a major fraction of the fission gas will be released from the fuel. This allows a large amount of fuel swelling and gas release to take place, reduces fuel cladding mechanical interaction (FCMI), and is the key to successful high-burnup operation of these fuels. This is achieved by employing relatively low planar smeared densities, typically around 75%. The large amount of radial swelling allowed by low planar smeared density also results in much larger axial growth of the fuel column. For example, sodium-bonded carbide[10] and sodium-bonded metallic U-Zr, both with a smeared density of ~75%, contact their cladding with 15% diametral swelling and, interestingly, both fuels have at that point grown axially by approximately 10%. The anisotropic swelling behavior of these fuels is caused by a difference in swelling behavior between the inner and outer regions of the fuel. A higher swelling implies higher fission gas diffusivity and higher creep rate in the central region of the fuel. As a result of a higher swelling rate and plastic, fluid-like behavior in the hotter central part of the fuel, this fuel is in a hydrostatic stress state, while the cooler and stronger outer shell in a state of tensile stress. Under ideal conditions, i.e., if the center is highly plastic and no axial temperature gradient exists, the circumferential tensile stress component in the outer zone is twice the axial component. In an actual fuel element the ratio of circumferential and axial tensile stress in the outer shell may be somewhat less than two because there will be a modest axial temperature gradient, and the stress state in the central fuel zone may not be purely hydrostatic. However, it appears that in carbide, nitride, and metallic fuels that possess a plastic central region with high swelling characteristics, the circumferential tensile stress in the outer fuel zone is always larger than the axial tensile stress. The effect of these tensile stresses on swelling and creep in the outer fuel zone explains the larger radial than axial swelling and thus observed anisotropy.

In addition to this basic fission-gas-induced swelling mechanism, metallic fuels may exhibit additional anisotropic irradiation growth and swelling induced by the radiation response of non-cubic crystalline phases present in uranium and plutonium and their alloys. Anisotropic irradiation growth and swelling of orthorhombic alpha uranium was first recognized in the late 1950's by Kittel and Pain[11] and was extensively studied in the 1960's. Shape changes involving (010) elongation and (100) shrinkage are the results of anisotropic condensation of interstitial and vacancy loops in the lattice. The Burgers vectors of different loops align with the prevailing stresses in the vicinity of the fission spike where they are formed. Thermal stresses are highly anisotropic because of the large anisotropy of thermal expansion in orthorhombic α-U[12]. As a result, crystallographically aligned microtears are formed in each grain. In α-U these tears most likely nucleate at twin boundaries formed during the martensitic transformation[13].

In polycrystalline fuel, mismatched growth stresses that develop at grain boundaries cause plastic flow or cavitation, depending on the grain size and temperature. Fission gas diffusion to these grain-boundary cavities and to the intragranular microtears gradually transform these initially empty features to fission gas bubbles. Several factors may result in net anisotropic swelling of an alloy that undergoes tearing. The presence of a preferred grain orientation or texture, induced by stress or temperature gradients when the fuel undergoes transformation to the α phase during manufacture, has a direct effect on isotropy. Indirectly, however, the stress state in the fuel element noted above has a pronounced effect on tearing and cavitation, and thereby, exacerbates the difference between radial and axial swelling of the fuel element when α phase is present.

The irradiation data discussed here were generated in an experimental program designed to develop the IFR fuel. The fuel elements consisted of both binary U-Zr and ternary U-Pu-Zr elements clad in both Type-316 and D9 austenitic stainless steel. Irradiation was carried out in the EBR-II reactor to a heavy metal burnup of 15 at.%. Examinations have been completed at 0.4, 0.9, 2, 3, 6, and 12 at.% burnup.

The fuel elements began irradiation in the as-cast condition. In this condition the zirconium is largely in supersaturated α' phase with the presence of a number of zirconium based precipitates caused by small quantities of carbon and oxygen impurities. The irradiation and thermal environment created by fissioning of the fuel allows the fuel structure to revert to a more equilibrium-like mixture of phases.

The test elements were fabricated in two distinct groups. One consisted of fuel with 0, 3, 8, 19, 22, and 26 wt % Pu - 10 wt % Zr-balance U clad in 7.4 mm (0.29 in.) diameter stainless steel tubes, and the other consisted of 0, 8, and 19 wt % Pu - 10 Zr - balance U clad in 5.8 mm (0.23 in.) diameter tubes. The fuel linear power was similar for the two groups, resulting in a nominally lower temperature gradient and lower fission rate for the 7.4 mm (0.29 in.) diameter element. Because of a higher coolant flow, overall temperature in the 7.4 mm diameter elements was lower as well. In the following, the 7.4 mm and 5.8 mm elements are referred to as A and B elements, respectively, to facilitate comparison. Nominal operating parameters for both groups are shown in Table II.3.

TABLE II.3. Nominal Operating Conditions of U-19Pu-10Zr Elements (at Beginning of Life)

Cladding Diameter, mm	7.4 (A)	5.8 (B)
Linear Power, kW/m	4.1	4.1
Peak Fuel Centerline Temp., °C	610	610
Radial Fuel ΔT,°C	130	130
Radial Fuel Temperature Gradient, °C/cm	455	600
Peak U^{235} Fission Rate, (10^{13}fissions/cm^3-s)	4.5	8.8

The overall swelling of the experimental fuel elements was determined by measuring diameter and length changes from neutron radiographs taken at various intermediate burnup intervals. This technique gave reliable data on free swelling up to the point at which the fuel contacts the cladding. Beyond this point, swelling is mechanically restrained by the cladding, and only axial fuel strain can be measured. The radiography measurements were compared with measurements from metallographic sections taken from selected fuel elements. This was found to be a reliable experimental technique. The fuel microstructure was studied with standard metallographic techniques and scanning electron microscopy (SEM) employing secondary electron and back-scattering detection.

Fuel slug length changes for various fuel compositions as a function of burnup in the A elements are shown in Fig. II.11. Because these length changes were measured at frequent intervals from neutron radiographs taken from the same set of elements, they offer the most detailed picture of overall fuel swelling at low burnup. The swelling of all compositions has an incubation burnup of approximately 0.3 at.% followed by rapid swelling over approximately a 1 at.% burnup interval. All compositions behave in a similar

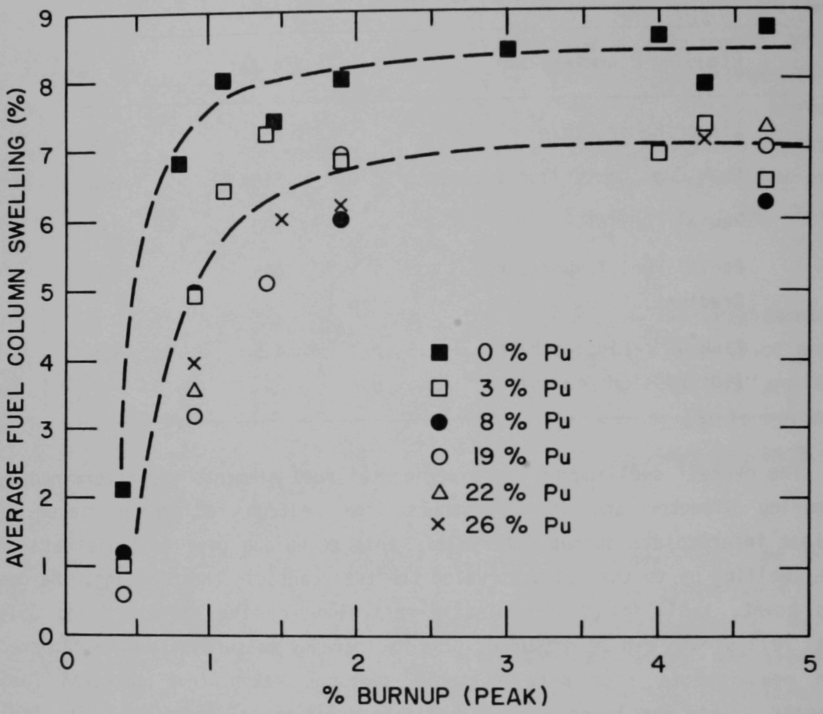

Fig. II.11. Axial Fuel Swelling of 7.4 mm (0.29 in.) Elements manner with the exception of 0% Pu, which swells significantly faster and reaches a somewhat higher level of axial growth.

The leveling off of the swelling vs burnup curve is due to axial shear stresses caused by fuel/cladding contact, however, as noted earlier for isotropic swelling, this level should be reached at ~15% for an as-built planar-smeared density of 75%, not as shown in Fig. II.11 at 6-9%. This anisotropic swelling behavior is shown graphically in Fig. II.12. Shown in the Fig. II.12 are both average axial and diametral swelling measurements taken at two burnup intervals prior to fuel/cladding contact. It appears that the degree of anisotropy varies substantially between the different fuel compositions.

The B elements were first examined at ~1 at.% burnup and at that point had already reached fuel/cladding contact. Therefore, diameter data are not available for this set of elements. However, axial swelling measurements were continued well beyond 1 at.% burnup, after which fuel-cladding contact is made and swelling slows dramatically. These axial swelling data are shown in comparison with the A data in Fig. II.13 for fuel compositions common to the two sets of elements. The behavior of 0% Pu and 8% Pu is virtually identical for the two tests that ran incidentally under different irradiation conditions. However, the axial swelling in 19% Pu B elements is only about 1/3 as much as that in A elements. It would appear that the B elements swelled very anisotropically, for at the point of fuel/cladding contact (~1 at.% burnup) the axial swelling is only ~3%, compared to a projected isotropic value of 15%.

Anisotropy of the swelling i.e., the consistently higher radial than axial swelling component, is essentially due to the effect of differences in swelling mechanisms between the hotter and the cooler part of the fuel. Specifically, the large radial temperature gradient leads to the development of distinct microstructural radial zones that have different swelling properties, and thus, interact mechanically. Addition of Pu increases the differences in swelling properties of the zones and their interaction, leading to a higher degree of anisotropy. However, the absence of the orthorhombic α phase, in the cooler regions of high Pu fuel, in turn reduces anisotropy. This trend appears not to hold for high Pu alloys operating at high

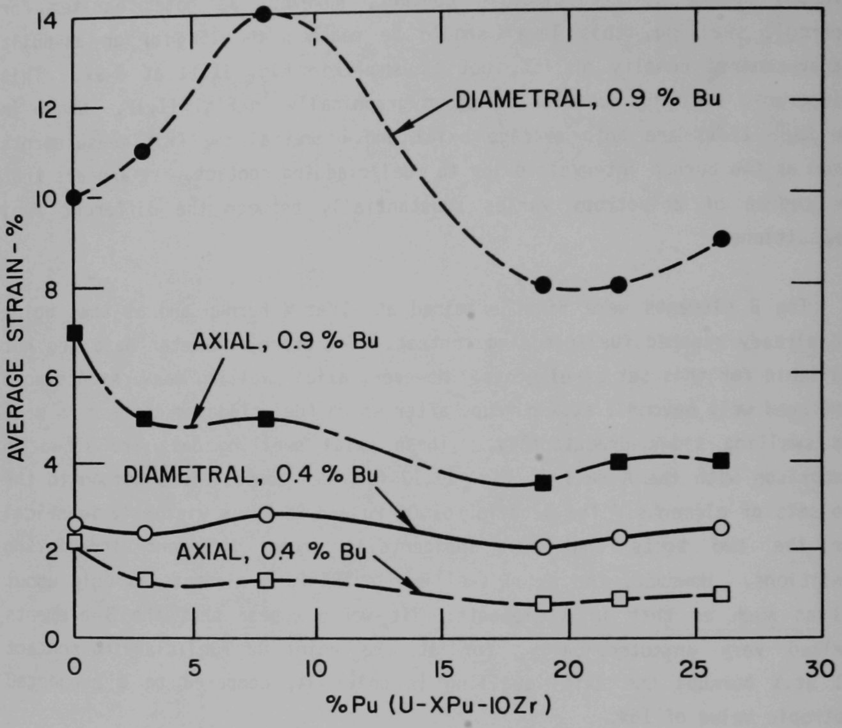

Fig. II.12. Axial and Average Diametral Fuel Swelling of 7.4 mm (0.29 in.) Elements

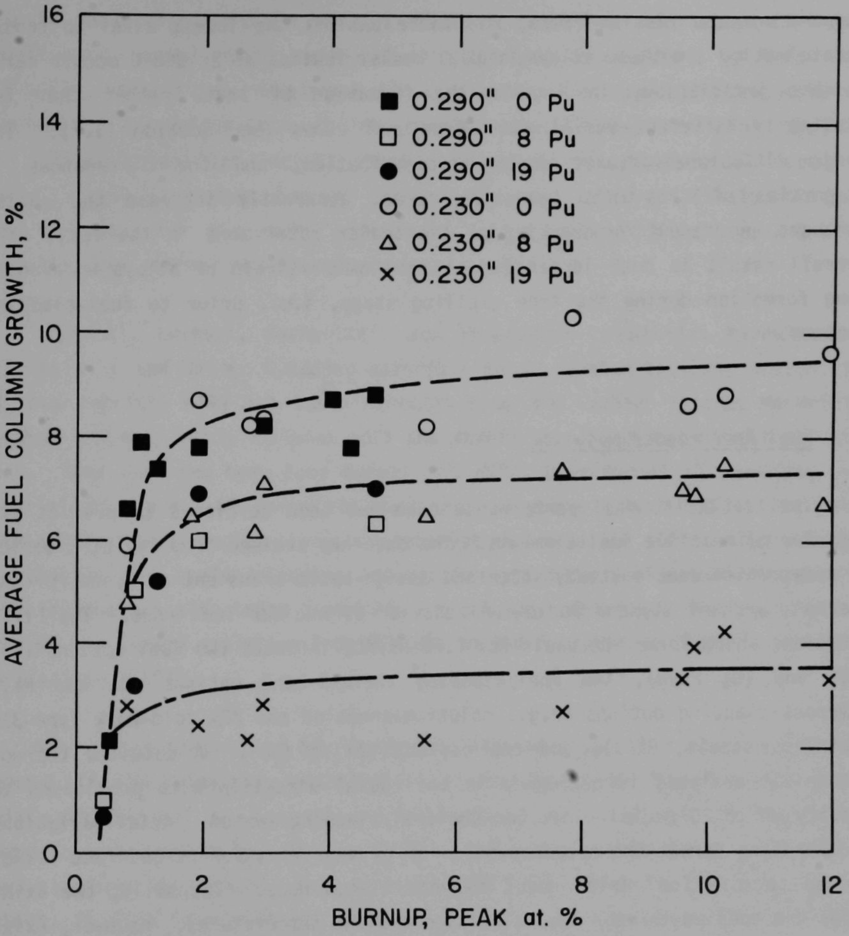

Fig. II.13. Axial Fuel Swelling of 7.4 mm (0.29 in.) and 5.8 mm (0.23 in.) Elements temperature and fission rates, for these exhibit the lowest axial to radial strain ratio. In these alloys, radial redistribution of Zr and U occurs early in the irradiation, leading to the formation of three rather than two distinctly different radial microstructural zones (see Section II.E). The large diffusional fluxes during redistribution, and the differences in properties of the three resulting zones, apparently increase the radial stresses and result in cracking of the cooler outer zone in the fuel. The overall result is much larger radial than axial strain of alloys undergoing zone formation during the free swelling stage, i.e., prior to fuel-cladding contact.

H. Fuel Performance Modeling

The LIFE-METAL fuel performance code has been developed to predict the behavior of metallic fuel elements. The code has evolved from the LIFE series of codes which enable steady-state and design-basis-transient analyses for the thermal, mechanical, and radiation behavior of nuclear fuel rods. The LIFE-4CN code, which forms the basis for LIFE-METAL, includes two fuel options [(U, Pu)C and (U, Pu)N], two fuel/cladding thermal-bond options (He and Na), numerous cladding options (e.g., solution-annealed and 20% cold-work Type-316 stainless steels, etc.), and one coolant option (Na). A detailed thermomechanical analysis is performed in the radial direction with provisions to specify up to 20 radial rings for the fuel/cladding system. Axial variations in operating conditions are accounted for by inputting powers and fast fluxes for up to nine fuel axial nodes and one plenum node. Thermally, the axial nodes are coupled through the calculated coolant temperatures. However, axial heat conduction is ignored (a good approximation), and there are no provisions for mechanical coupling between axial nodes.

A detailed mechanical analysis is performed for both fuel and cladding utilizing the generalized-plane-strain assumption for each axial segment, and incorporating a large strain capability, the solution procedure involves iteration on local total strain within each time step. Approximate analytical solutions are used to accelerate convergence. The solution procedure is explicit in time.

In converting LIFE-4CN to LIFE-METAL, a number of fuel properties and models were changed and/or added. Fuel properties correlations for U-5Fs and U-xPu-yZr were first developed as continuous functions of temperature, porosity, alloy composition, stress, fission rate, burnup, etc. The physical and thermal properties include density, phase-change temperatures, specific heat, thermal expansion, thermal conductivity, and alloy and fission product distributions. The mechanical properties include elastic modeling, fracture strength, and thermal and fission enhanced creep.

Physical, thermal, mechanical, and irradiation properties correlations for the test and design cladding materials (e.g., austenitic 316, austenitic D9, and ferritic HT9) are taken directly from the Nuclear Systems Materials Handbook (NSMH), which includes both the correlations and the properties data base. Some work has been done during LIFE-METAL development in improving the correlations (e.g., D9 creep and swelling) to get a better fit to the data base within the operating range of interest for metallic fuels. The wastage correlation for sodium/cladding interaction and time and strain-temperature correlations are also taken from NSMH. Models were developed for Ni depletion from D9 and carbon depletion from HT9 due to the fuel/sodium/cladding chemical interaction (FCCI).

Fuel model development has focused on isotropic swelling due to solid and gaseous fission products, anisotropic deformation (i.e., larger radial than axial growth) due to texture and anisotropic stress states in the lower temperature α-uranium-type phases, and fission gas retention and swelling. Fuel-cladding mechanical interaction (FCMI) is not modeled explicitly. Rather, it is a result of the detailed fuel and cladding mechanical analyses which have provisions for both open and closed fuel/cladding gaps.

The focus of LIFE-METAL development has been on verifying the algorithms and validating the models for predicting fuel-rod behavior important in design analysis under normal operating conditions. Predictions important to the nuclear design are fuel length changes and changes in fissile content due to burnup and breeding. Thermal predictions of interest are fuel temperature, design margins to fuel melting, and design margins to low-melting-temperature alloy (e.g., U-Fe) formation. Mechanical predictions of interest to designers are cladding damage and design margin to cladding failure due to fission gas pressure loading, FCMI and FCCI, and cladding deformation and design margin to significant coolant flow area reduction.

As part of the verification process, LIFE-METAL has been subjected to extensive steady-state and transient thermal benchmark testing, and thermoelastic-creep benchmarks for pressurized solid and hollow cylinders and solid cylinders with thermal gradients. Improvements in the analytical methods and the numerical algorithms have been made based on these benchmarks.

The validation effort has been quite detailed. Postirradiation data are available from a large number of fuel-element irradiations for "global" integrated parameters such as fission gas release, fuel volumetric change, and fuel length change. Axial profiles are available for fuel radial growth at low burnup (prior to and including initial fuel-cladding contact) and for cladding radial growth for a wide range of burnups and fast fluences. Other data available on a more limited basis are radial and axial variations in U, Pu, Zr, and fission gas porosity, axial variations in fraction of porosity filled (logged) with Na, and depth of C-depleted and Ni-depleted zones in HT9 and D9, respectively. Fairly complete sets of data are currently available for 65 fuel-rod irradiations. Limited data (e.g., fuel length change, cladding diameter change) are available for hundreds of irradiated fuel rods. Table II.4 summarizes the irradiation data base used in LIFE-METAL validation as compared to a sample set of anticipated design conditions. Design ranges not covered under the current LIFE-METAL validation data base are listed in the "data needs" column of Table II.4. It should be highlighted that the irradiation test program reflects serious attention to data needs. Subassemblies are being irradiated currently or are in the process of examination for the full range of design conditions needed to qualify LIFE-METAL as the reference design tool for metallic fuel performance predictions under normal operating conditions.

The approach used in validating LIFE-METAL to date has been to focus on the detailed data from 34 irradiated fuel rods for the purpose of adjusting model parameters. These data are from two fuel compositions (U-10Zr and U-19Pu-10Zr) covering the burnup range of 0.4-11 at.% and the fast fluence range of 0.4-11 x 10^{22} n/cm^2. The remaining 31 validation cases were analyzed with

TABLE II.4. Summary of Irradiation Data Needs Based on the Range of Experimental Materials and Operation Conditions as Compared to Reference Design Conditions

Parameter	Experimental	Design	Data Needs
Fuel Pu Content, wt.%	0-26	26	19-26
Fuel Zr Content, wt.%	6-14	10	-
Smear Density, %	70-85	75	-
Fuel Length, m	0.34	1.27	0.34-1.27
Plenum/Fuel Volume Ratio	1.3-2.1	2.1	-
Cladding	HT9,D9	HT9	-
	316SS		-
Peak Burnup, at.%	0.4-18.0	15.5	-
Peak Power, kW/m	25-50	34	-
Peak Fast Fluence, 10^{23} nvt	0.04-1.8	2.9	1-2.9
Peak Clad, Temperature, °C	500-600	564	550-625

LIFE-METAL without changing any code parameters to test the code's extrapolation in burnup (up to 18 at.%), interpolation in Pu content (0-19 at.%), extrapolation in Pu content (19-16 wt %, extrapolation in Zr content (6-14 wt %), and exterpolation in initial fuel smear density (70-85%). Excellent agreement has been achieved between predictions and measurements for fission gas release, fuel volume change, fuel length change, low-burnup fuel diametral strain profiles, and cladding strain profiles for all fuel elements examined with an initial smear density of ~75%. Prior to this year, problems were encountered in underpredicting fuel and cladding (D9) diametral strains and overpredicting fuel axial strain. The significant progress made over the past year in improving predictions has come from the inclusion of an anisotropic fuel deformation model and an improvement in the D9 irradiation creep correlation. In the case of the 85% smear-density fuel, LIFE-METAL overpredicted HT9 cladding strain (0.72% vs 0.3% measured) for U-19Pu-10Zr fuel at 6 at.% burnup. More work needs to be done in this area to improve fuel restructuring and swelling models and fuel mechanical properties based on the results of this comparison.

In summary, reasonable progress has been made in validating LIFE-METAL predictions for fission-gas release, fuel volumetric strain, fuel length change, fuel diametral strain profiles, and cladding diametral strain profiles for the conditions listed in Table II.3. More work is needed in improving code predictions for initial smear densities >75%. Also, more data and validation are needed for higher Pu fuel (19-26 wt %), HT9 cladding at higher burnups (11-16 at.%), and higher fast fluences (11-29 x 10^{22} n/cm^2), and higher cladding temperatures (>530°C). Finally, validation data are needed in the area of fuel thermal performance. While most of the LIFE-METAL fuel models are temperature-dependent, no direct in-reactor data are currently available for validating the fuel thermal conductivity model which includes a reduction in effective conductivity due to fission-gas porosity development, and an enhancement in conductivity due to a partial ingress of liquid Na into the fuel interconnected porosity.

References for Section II

1. C. W. Bale, A. D. Pelton, and W. T. Thompson, "F*A*C*T Users' Instruction Manual," McGill University/Ecole Polytechnique, Montreal, (1979-84).

2. L. Leibowitz, E. Veleckis, R. A. Blomquist, and A. D. Pelton, "Solidus and Liquidus Temperatures in the Uranium-Plutonium-Zirconium System," J. Nucl. Mater., 154, 145 (1988).

3. L. Leibowitz, R. A. Blomquist, and A. D. Pelton, "Thermodynamics of the Uranium-Zirconium System," J. Nucl. Mater., 167, 76 (1989).

4. R. I. Sheldon and D. E. Peterson, "The U-Zr (Uranium-Zirconium) System," Bull. Alloy Phase Diagrams, 10, 165 (1989).

5. F. L. Oetting, M. H. Rand, and R. J. Ackermann, "The Chemical Thermodynamics of Actinide Elements and Compounds - Part I," Intl. Atomic Energy Agency, Vienna, Austria (1976).

6. H. Savage and R. D. Seibel, "Heat Capacity Studies of Uranium and Uranium-Fissium Alloys," Argonne National Laboratory Report, ANL-6702 (1963).

7. R. Fowler and E. A. Guggenheim, "Statistical Thermodynamics," Cambridge University Press (1939).

8. Y. S. Touloukian, R. W. Powell, C. Y. Ho, and P. G. Klemens, "Thermophysical Properties of Matter," IFI/Plenum, New York (1970).

9. L. Leibowitz and R. A. Blomquist, "Thermoconductivity and Thermal Expansion of Stainless Steels D9 and HT9," Int. J. Thermophys., 9, 873 (1988).

10. M. Colin, et al., "The Sodium-Bonding Pin Concept for Advanced Fuels Part I: Swelling of Carbide Fuel up to 12% Burnup," Nucl. Tech., 63, 442 (1983).

11. J. H. Kittel and S. H. Pain, "Effect of Irradiation on Fuel Materials," Proc. 2nd Intl. Conf. on the Peaceful Uses of Atomic Energy, Geneva, Coomm.P.1890, 5, 500 (1958).

12. S. N. Buckley, "Properties of Reactor Materials and the Effects of Radiation Damage," D. J. Littler, Ed., Butterworth, London (1962).

13. R. D. Leggett, B. Mastel, and T. K. Bierlein, "Behavior of High Purity Uranium," Westinghouse Hanford Laboratory Report HW-79559, UC-25 (1963).

III. PYROMETALLURGICAL PROCESS DEVELOPMENT

A key element of the IFR concept is its unique fuel cycle. The development of a compact process for recovering plutonium and uranium from the metallic core and blanket materials, for removing fission products from them, and for re-enriching the core alloy with plutonium bred in the blanket has been a prime activity. To accomplish this, major development efforts are directed toward flowsheet development and process chemistry, process development studies, engineering-scale demonstration of the electrorefining process, and waste treatment and management.

A. Process Flowsheet and Chemistry

The IFR pyrochemical process for recovery of pure uranium (for blanket element fabrication) and a uranium-plutonium mixture (for core fuel elements) is based on the removal of pure uranium onto a solid cathode, even in the presence of much more $PuCl_3$ than UCl_3 in the electrolyte salt. The basic flowsheet for processing the IFR fuel and blanket material is shown in Fig. III.1. Following disassembly of the reactor fuel subassemblies, the fuel pins are chopped into short lengths, which are packaged to form a batch for dissolution in the electrorefiner. An oxidant, $CdCl_2$, is added to convert sodium from the thermal bond in the fuel and active fission-product metals to their chlorides, which become a part of the molten chloride electrolyte. Uranium is electrorefined by deposition on a solid cathode. Uranium-plutonium is electrorefined by deposition in a liquid cadmium cathode. These cathodes are removed from the electrorefiner cell, the cadmium and occluded salt are removed by retorting, and the uranium or uranium-plutonium product is consolidated by melting. The residual solids in the cadmium pool constitute the noble metal fission-product waste from the process. The salt, which can be made sufficiently free of actinides to be regarded as a nontransuranic (nonTRU) material, is a process waste. The rare earth and noble metal fission products may be consolidated into a metal matrix such as copper to provide a permanent disposable waste form. The chloride salt waste, which contains fission-product cesium, strontium, and iodine-129, may be incorporated into a suitable matrix material to produce a disposable (nonTRU) waste form.

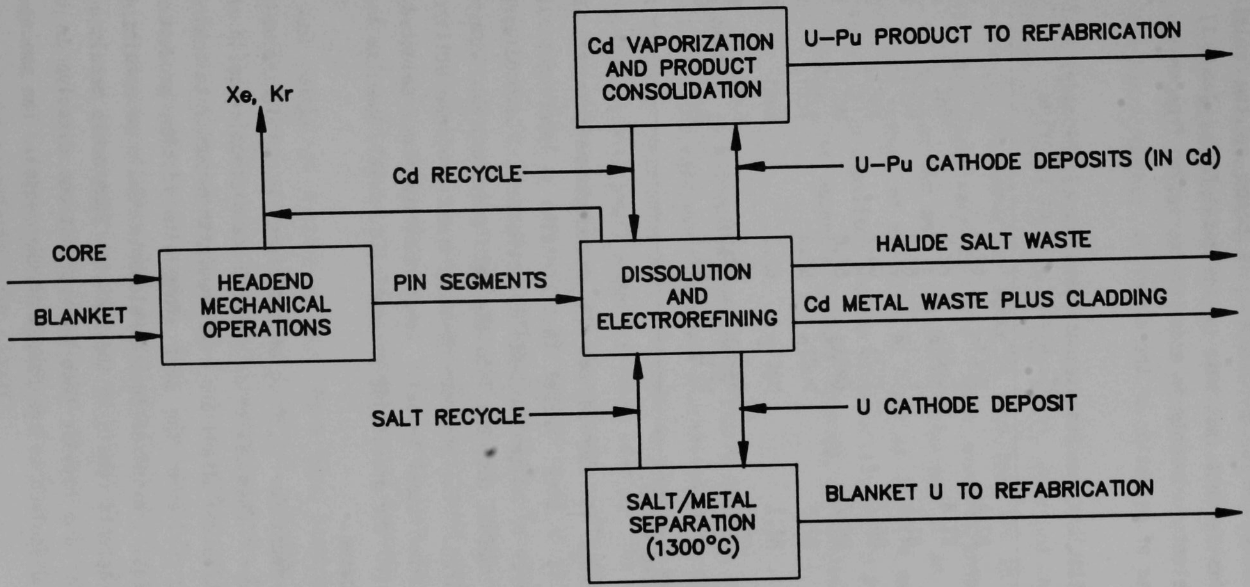

Fig. III.1. Electrorefining Process for IFR Core and Blanket

The chemistry of the pyroprocess is based on the relative ease of oxidation of the elements that make up the metal fuel. Table III.1 lists the chlorides of selected elements in order of increasing free energy of formation (decreasing ease of oxidation of the element).

TABLE III.1. Free Energies of Formation of Chlorides at 500°C
$-\Delta G^\circ_f$, kcal/g atom of chlorine

$BaCl_2$	87.9	$PrCl_3$	69.0	$ZrCl_2$	46.6
CsCl	87.8	$CeCl_3$	68.6	$CdCl_2$	32.3
RbCl	87.0	$NdCl_2$	67.9	$FeCl_2$	29.2
KCl	86.7	YCl_3	65.1	$NbCl_5$	26.7
$SrCl_2$	84.7	$CmCl_3$	64.0	$MoCl_2$	16.8
LiCl	82.5	$PuCl_2$	62.4	$TcCl_3$	11.0
NaCl	81.1	$MgCl_2$	62.1	RhCl	10.0[a]
$CaCl_2$	80.7	$NpCl_3$	58.1	$PdCl_2$	9.0
$LaCl_3$	70.2	UCl_2	55.1	$RuCl_3$	6.9[a]

[a] Estimated value.

Pyroprocessing is carried out in an electrorefiner at 500°C. The electrorefiner is a steel vessel that contains a layer of molten cadmium underlying a layer of molten LiCl-KCl eutectic salt. Cathode assemblies and anode "baskets" can be inserted into the salt and withdrawn from the electrorefiner as desired. The engineering-scale electrorefiner utilizes a 32-in. diameter, low-carbon steel vessel. Low-carbon steel was selected because it is compatible with the processing reagents (Cd, salt), has low cost, and can be easily fabricated.

A batch of spent fuel (~20 kg of actinides) is put in the molten salt of the electrorefiner. Chemical oxidation with cadmium chloride is then used to convert easily oxidized alkali and alkaline earth elements to their chlorides. The chlorides dissolve in the salt along with fission product iodide and bromide. Less easily oxidized (noble) elements remain as metals; in particular, cladding fragments remain in the basket. Some noble metals are released as particles that are heavier than the salt; these dissolve in the cadmium layer or sink undissolved to the bottom of the vessel. The amount of oxidant is adjusted so that the actinides and rare earths are found both as metals and in the salt, although actinides will mostly be found as metal and rare earths will mostly be chlorides. Thus, oxidation effects most of the separation of actinides from fission products.

Separate collection of the uranium product and the mixed actinide product is possible because uranium is slightly less easily oxidized than the other actinides, and because the oxidation state is such that the salt contains a mixture of actinides (and rare earths). When electrotransport is used simultaneously to oxidize the metals to their chlorides at an anode and to reduce an equivalent amount of chloride to metal at a solid metal cathode, uranium is preferentially deposited and the other actinides are preferentially oxidized. The product is essentially pure uranium, contaminated with the salt.

When the cathode is a crucible containing liquid cadmium, plutonium, the minor actinides, and the rare earths are all stabilized as metals by interaction with the cadmium. Uranium is not. The cadmium electrode product is thus a mixture of actinides with small amounts of rare earths. The composition of the mixture is determined partially by the composition of the anode metal, but mostly by the composition of the salt. Our procedure is to control the salt and anode compositions by removal of selected amounts of uranium with solid cathodes so that the cadmium cathode has the desired composition. We have been successful in producing the predicted salt and cathode compositions from uranium-plutonium-rare earth mixtures. Also, the data have shown that americium follows the plutonium in the electrotransport process.

After some number of batches of fuel have been processed (perhaps a dozen, depending on the age of the fuel and its activity), it will be necessary to remove noble metal fission products from the cadmium by mechanical removal of solids or by removal and distillation of the cadmium pool. Removal of the rare earths from the salt by reduction with lithium-potassium-cadmium alloy will purify the salt sufficiently to allow recycle. Cesium and strontium are the only radioactive species remaining in the recycled salt. Both the noble metals and the rare earths will be in a metallic form and can easily be incorporated in a copper matrix, a waste form that is expected to be satisfactory for disposal.

B. Laboratory-Scale Process Development

1. Flowsheet Verification

The compositions of the salt, solid, and liquid metal phases in the electrorefiner have been predicted by an ANL model based on thermodynamic data; our selection of the kind and arrangement of the process steps is based on these predictions. Figures III.2 and III.3 compare data from our experiments to model calculations for electrotransport into a cadmium electrode. In Fig. III.2, measured plutonium concentration is only presented for the last run, since no detectable plutonium could be found in the cathode metal product formed in earlier runs. This agrees with the model prediction. Rare earth analyses (represented in Fig. III.2 by Nd) indicate that, at most, undetectable amounts of rare earths were codeposited with uranium, again as predicted. The anode was saturated with zirconium but, as predicted, the zirconium content of products was less than 0.01%. The agreement between predicted and observed behavior is completely adequate for process design.

To date, we have obtained good agreement between predicted and measured compositions of the salt and cadmium phases, but we have not specifically verified the maximum $PuCl_3/UCl_3$ ratio in a salt from which uranium free of plutonium could still be extracted. Experiments ENG-26 to ENG-30 were conducted to establish this ratio, to compare the experimental value to the predictions of our model, and to investigate the behavior of the solid cathode.

The experimental procedure consisted of collecting the material on an iron mandrel by passing constant current for a selected period of time, removing the cathode assembly from the electrorefiner, allowing the cathode assembly to cool to room temperature, scraping off and weighing the cooled product, and then lowering the cathode assembly back into the electrorefiner for the next test. The laboratory-scale electrorefiner used in these experiments and other process development studies is shown in Fig. III.4. The cell operating temperature during testing was 500°C. During the cool-down period after each test, the product was visually examined and photographed. The deposit from each test was weighed, ground, and split into portions. A representative portion of each deposit was taken for chemical analysis.

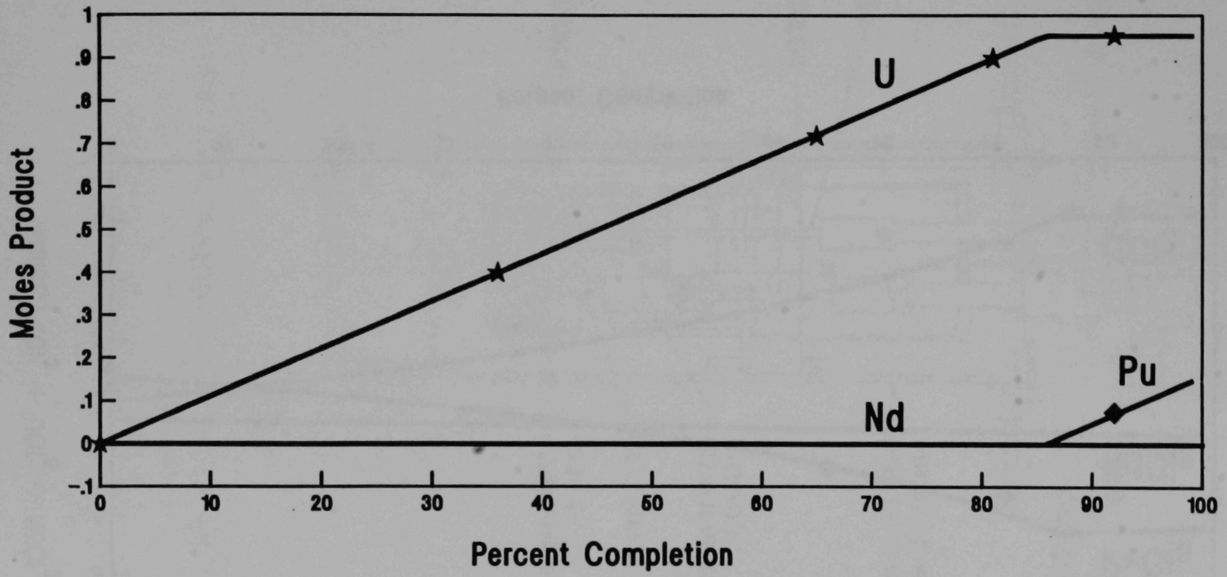

Fig. III.2. Accumulation in Solid Cathode during Electrotransport. Curves are from thermodynamic model calculations; points represent experimental measurements. "Percent Completion" is the percentage of the initial U and Pu in the cadmium pool transferred to the cathode.

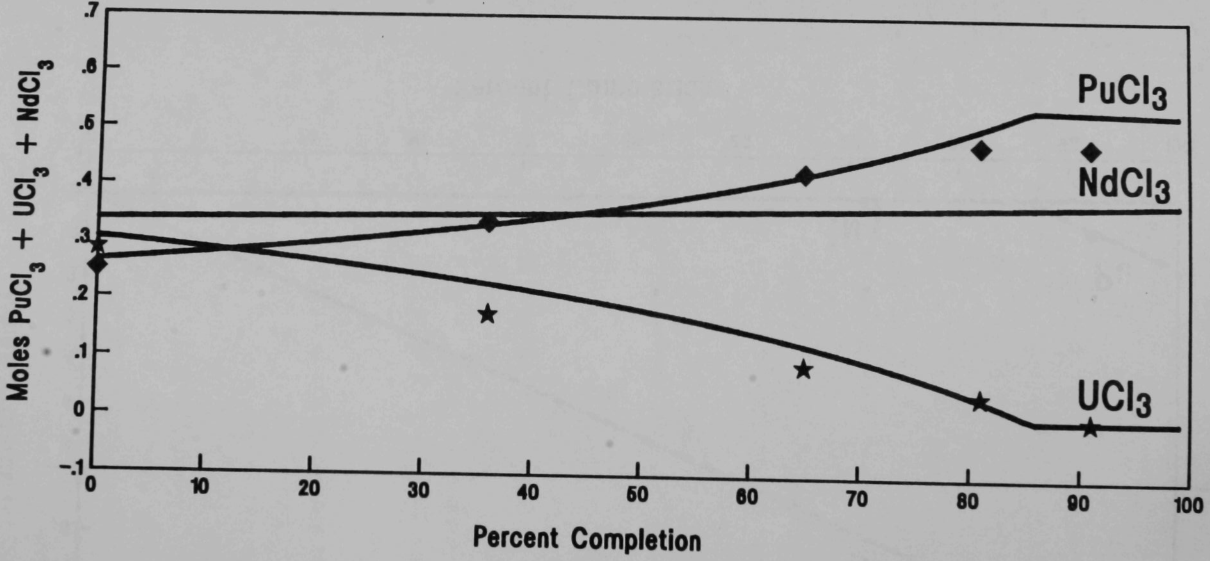

Fig. III.3. Composition of Electrolyte during Electrotransport with Solid Cathode. Curves are from thermodynamic model calculations; points represent experimental measurements. "Percent Completion" is the percentage of the initial U and Pu in the cadmium pool transferred to the cathode.

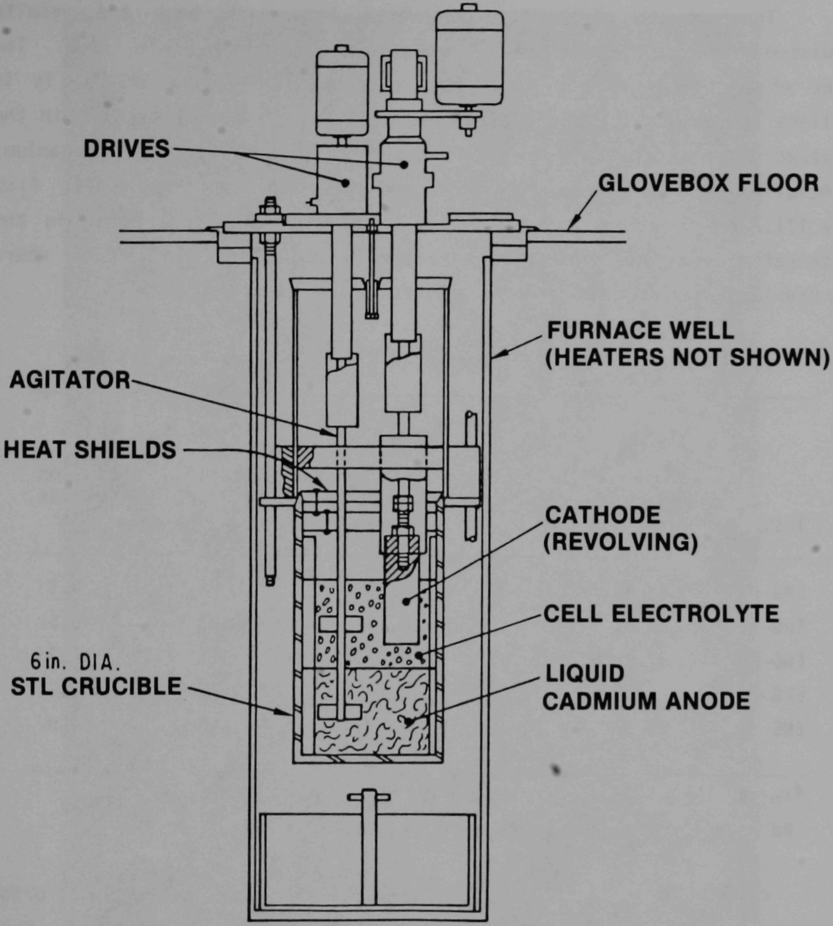

Fig. III.4. Laboratory Electrorefining Apparatus

The amounts of product recovered from each test and results calculated from associated chemical analysis are given in Table III.2. The amount of plutonium in the first four products (ENG-26 to ENG-29) is in excellent agreement with that calculated due to the presence of salt in the recovered material (not due to electrodeposited plutonium). Thus, uranium, essentially free from plutonium, is obtained in the first four products. From Table III.2 we find that 92.5% of the uranium originally present in the electrorefiner was electrodeposited as pure uranium prior to ENG-30, where both uranium and plutonium electrodeposited on the solid cathode.

TABLE III.2. Product Recovered in Five Flowsheet Experiments[a]

Test	Product, g	Amount in Product, g		Calculated Pu Due to Salt Residue, g	Salt on Cathode, g
		U	Pu		
ENG-26	91.43	71.30	0.38	0.40	20.1
ENG-27	113.20	96.59	0.41	0.32	16.6
ENG-28	87.40	76.05	0.329	0.36	11.3
ENG-29	83.08	41.81	1.73	1.57	41.3
ENG-30	85.87	14.72	16.33	1.90	54.8

[a] Initial Condition: (1) 309 g U and 171 g Pu; (2) sum of Nd + Ce + Y, 44 g; and (3) anode saturated with Zr.

Figures III.5 and III.6 are photographs of the cathode products prior to removal from the iron mandrel for runs ENG-26 and -30, respectively. When pure uranium is the product with the salt low in $PuCl_3$ (Fig. III.5), the product is dendritic and very adherent to the cathode mandrel. When mixed U/Pu is the product (Fig. III.6), with the salt high in $PuCl_3$, the product is very fine crystals in a deposit that contains much more electrolyte and is very weakly adherent to the cathode. This U/Pu product will not be collected on the solid cathode but in the liquid cadmium cathode, as discussed later.

A material balance for uranium and plutonium was made for each test using the chemical analytical results obtained from product, salt, and anode

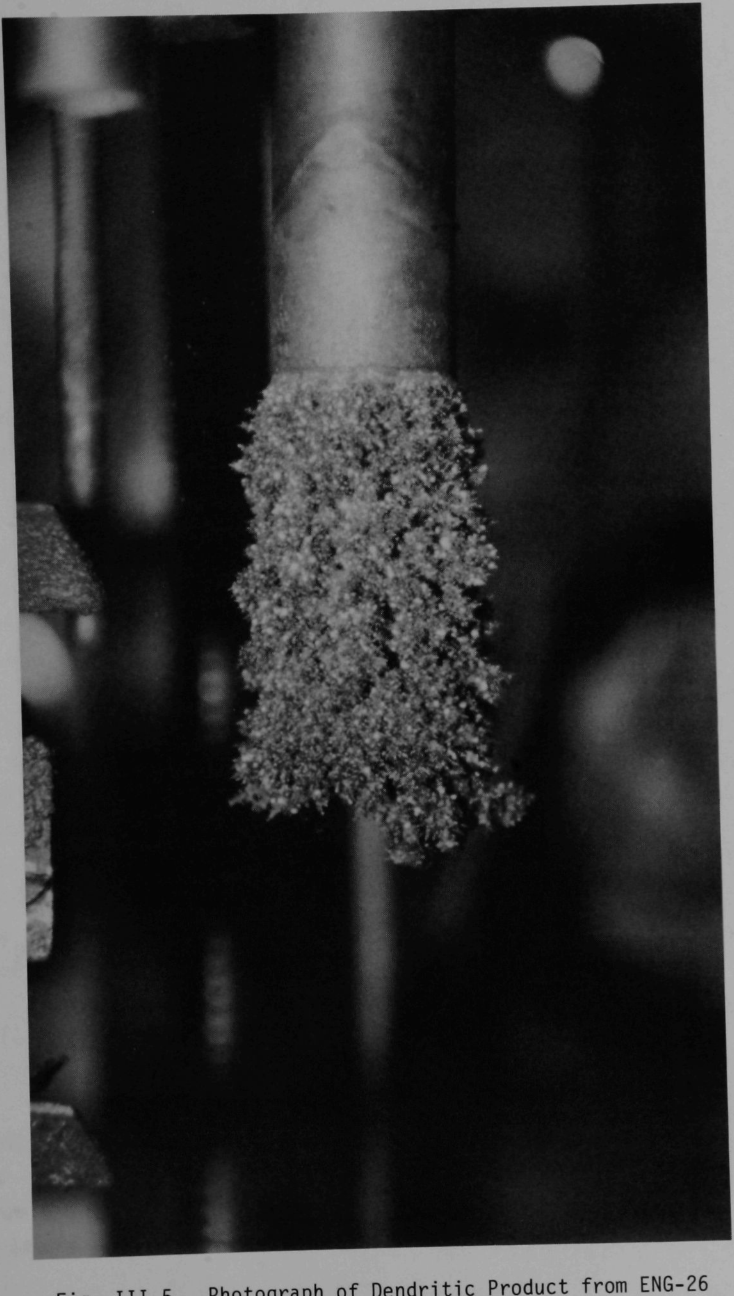

Fig. III.5. Photograph of Dendritic Product from ENG-26
[illegible] 4388 Frame 8)

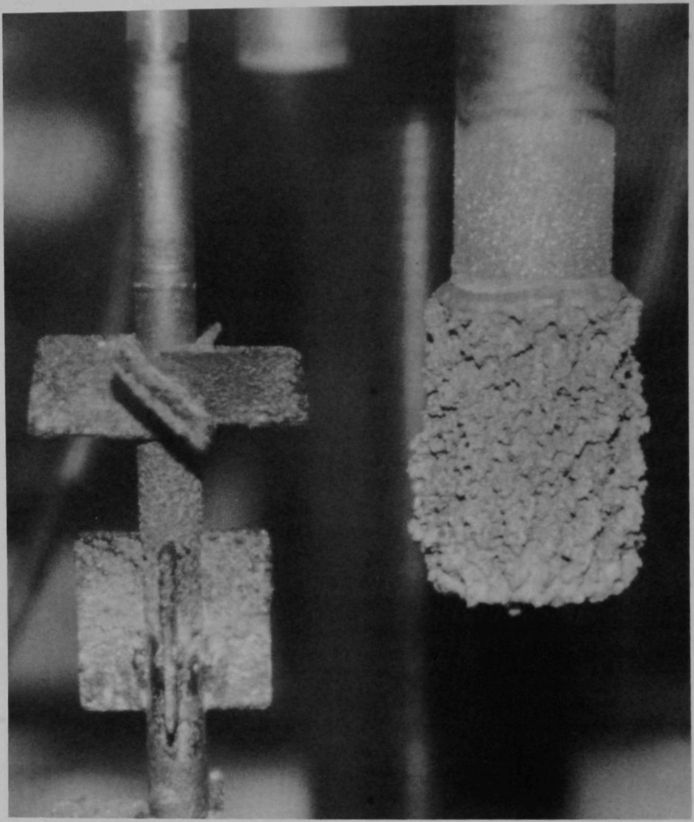

Fig. III.6. Photograph of Weakly Adherent Product from ENG-30
(ANL Neg. No. 4700 Frame 18)

metal. The material balance was excellent, and the results were within the error in sampling and analysis of the liquid cadmium, salt, and the solid product. In these tests, we expected the sum of the concentrations of U, Pu, Ce, Nd, and Y in the electrolyte phase to be a constant, and this was verified by the chemical analysis.

The following two conclusions were reached from these test results. First, when blanket fuel and core fuel are processed sequentially in the electrorefiner, essentially plutonium-free uranium may be obtained from the electrorefiner for blanket fuel refabrication in amounts exceeding the input blanket feed. Second, plutonium-uranium alloy may be obtained from the electrorefiner with a Pu/U ratio greater than that in fast reactor fuel. In addition, this series of tests has verified the thermodynamic model.

Another important issue for both product collection and rare-earth removal is the relative partition of plutonium and the rare earths between cadmium and salt. We have used available data to predict the separation of plutonium and neodymium and assumed that the other rare earths behave like neodymium. Scoping experiments (competitive partition of rare earths) generally agreed with this assumption under electrorefiner operating conditions; partition coefficients for five of the the seven most abundant rare earth elements were identical within experimental error. Under reducing conditions, however, europium and samarium, because of their very stable +2 oxidation state, strongly favored the salt phase relative to the other rare earths. More precise rare-earth characterizations are under way; in the case of europium, they have shown that cadmium chloride was not a sufficiently strong oxidizing agent to produce the +3 oxidation state. Nonetheless, all rare earths can be removed from the salt with alkali-cadmium alloys.

2. Product Purification and Consolidation

As mentioned earlier, two types of cathodes for the collection of product material, uranium or a uranium-plutonium mixture, are under development: (1) a solid metal mandrel and (2) liquid cadmium. Electrotransport of uranium onto a solid steel mandrel is straightforward, but plutonium deposition (along with uranium) onto a solid mandrel is difficult. Deposits have been amorphous, fine grained, and non-adherent. Therefore, the use of a liquid cadmium cathode for deposition of uranium and plutonium has been investigated.

For demonstrating codeposition of uranium and plutonium, conditions in a small-scale electrorefiner (principally, the relative amounts of uranium and plutonium) were arranged to simulate the plutonium transport portion of the theoretical transport curves. The revolving solid cathode was replaced with a small stationary ceramic (BeO) crucible containing a cadmium liquid pool equipped with a small stirrer, which also acted as the current lead.

Deposition of uranium into a cadmium cathode after the saturation concentration has been reached is accompanied by a pronounced tendency of deposited uranium to form dendrites, which grow out of the surface of the cadmium. Formation of uranium dendrites must be avoided because they will eventually short circuit the electrorefining cell. Their buildup can be reduced by using a stirrer or cutter blade that sweeps the cadmium cathode surface. Uranium, which has a density of 19 g/cm^3, tends to sink to the bottom of the cadmium. (The density of cadmium is 7.8 g/cm^3.)

In contrast, $PuCd_6$ crystals, which have a density of about 9.3 g/cm^3, tend to remain suspended in the liquid cadmium. As the cadmium surface is "swept," the $PuCd_6$ crystals tend to pile up in front of the blade and be "plowed out" of the cathode crucible. The beryllia stirrer blades were withdrawn from the crucible before the cathode assembly was removed from the electrolyte. The composition of the various cathode phases is given in Table III.3 for experiment ENG-21. The total uranium and plutonium content is in agreement with the inventory differences in cell anode and electrolyte before and after electrolysis. The material balance for the experiment is given in Table III.4. This experiment proved that plutonium will codeposit with uranium into a liquid cadmium cathode. Similar results were obtained in the previous experiment (ENG-20).

Figure III.7 shows a half section of the U-Pu-Cd ingot removed from the crucible (in ENG-21). In this experiment, the plutonium content of the cadmium product phase was 14.5%. Analyses indicated the solid content of the

TABLE III.3. Weights of Constituents in Cathode Components (Experiment ENG-21)

		Metal Phases, g		
	Salt,g	Cd	U	Pu
Cathode Ingot Average[a]	37.0	243	31.2	41.1
"Overflow" on Cathode Supports	2.5	20	1.3	2.1
Loose Dendrites	10.1	5.8	15.6	1.2
Plated on Stirrer	3.9	21.2	2.6	4.3
TOTAL			50.7	48.7

[a] Estimated from four different samples for the heterogeneous ingot removed from the crucible.

product ingot to be about 45 vol %. The large solids content probably results in a slurry too thick to be stirred without overflow. Further work is needed to determine the capacity limit of the electrode and the best means of providing agitation. The goal is to obtain a cadmium ingot with a clean interface between the top surface of the metal ingot and the electrolyte.

In the IFR process, decontamination of the plutonium product will be controlled by rare earth elements. That is, the only fission product elements expected to accompany plutonium to any extent through the process are the rare earths. The rare earths with high fission yields are cerium and neodymium. Information on the behavior of cerium and neodymium was obtained in the two plutonium-transport experiments (ENG-20 and -21). Decontamination factors were calculated from Nd/Pu and Ce/Pu ratios in the cathode product divided by the same ratios in the IFR discharge fuel composition (see Table III.5). The decontamination factors for neodymium were 5.8 and 3.1 for ENG-20 and -21, respectively. The cerium decontamination factor was 5.3 for ENG-21.

In the two plutonium-transport experiments, the americium-to-plutonium ratio in the cathode product was essentially the same as in the anode prior to electrorefining. This indicates that americium transported with the plutonium. Curium and neptunium are expected to behave similarly, but additional experiments to confirm this and to verify the observed behavior

TABLE III.4. Material Balance for Uranium and Plutonium in Experiment ENG-21

	Amount, g (wt %)	
	Plutonium	Uranium
Cell Inventory prior to Electrorefining		
Electrolyte	99.9 (2.3)	63.4 (1.4)
Cadmium Anode	83.4 (0.52)	66.1 (0.42)
Total	183.3	129.5
Cell Inventory after Electrorefining		
Electrolyte	105.2	55.0
Cadmium Anode	28.5 (0.18)	18.8 (0.12)
Total	133.7	73.8
Inventory Difference	49.6	55.7
Cathode Products Content[a] (Metal Phase)	48.7	50.7
Consumption in Analytical Samples of Cathode Products	2.3	1.4
Cell Inventory after Cathode Products Dissolved in Cell Fluids		
Electrolyte	101.2	63.4
Cadmium Anode	79.4	61.6
Total	180.6	125.0

[a] Estimated from samples of the heterogeneous cathodic materials removed from the crucible.

Fig. III.7. Photograph of U-Pu-Cd Metal Ingot (Half-Section)
(ANL Neg. No. 1708 Frame 3)

TABLE III.5. Decontamination of Plutonium from Neodymium and Cerium in Experiments ENG-20 and -21

Experiment	Ratio	IFR Discharge Fuel	Cathode Product Ingot	Decontamination Factor
ENG-20	Nd/Pu	0.069	0.012	5.8
ENG-21	Nd/Pu	0.069	0.022	3.1
ENG-20	Ce/Pu	0.045	Not obtained	-
ENG-21	Ce/Pu	0.045	0.0085	5.3

of americium are required. If, as expected, americium, curium, and neptunium accompany plutonium through the process, they will be recycled to the reactor in the core fuel, where they will be consumed by fission. Burning most of the actinide elements in the reactor, rather than dealing with them in various waste streams, would be advantageous.

In the current flowsheet under development for processing IFR fuel, plutonium-uranium products are accumulated in liquid cadmium cathodes in the electrorefining cell. These products have to be processed in order to remove salt and cadmium and recover uranium and plutonium for further recycle. Previous tests have shown that high-purity uranium (<80 ppm Cd) can be obtained by retorting a uranium product deposited on a solid cathode that contained ~12 wt % salt and 2 wt % cadmium. Because a similar high-purity product is necessary from treatment of uranium-plutonium products obtained by using liquid cadmium cathodes, we conducted a series of experiments to demonstrate the purification and consolidation of U-Pu-Cd products. The major question to be answered was whether or not the $PuCd_6$ intermetallic compound could be decomposed by retorting.

The starting compositions for these experiments were selected to simulate the expected product in the recovery of uranium and plutonium in a liquid cadmium cathode. The starting material was slowly heated under a partial vacuum (5-10 mm Hg) to about 700°C. The material was cooled and sampled to obtain an intermediate composition, which is shown in Table III.6 along with the starting composition. X-ray diffraction analysis identified alpha-uranium and $PuCd_6$ as the intermediate phases. The distillation and consolidation were completed by heating the intermediate material to about 1300°C (above the melting point of uranium). A consolidation ingot typical of those produced in these experiments is shown in Fig. III.8. The composition is shown in Table III.6. In the first experiment, the product contained less than 150 ppm of cadmium and beryllium. The product from the second experiment contained 54 ppm of cadmium and 287 ppm beryllium (from the BeO crucible). These experiments have demonstrated that a purified and consolidated U-Pu product can be obtained from the electrorefiner product (U-Pu-Cd-salt), and that essentially no uranium or plutonium is lost in the process.

TABLE III.6. Starting, Intermediate, and Final Compositions for Product Purification and Consolidation

	Starting Composition, g (wt %)	Intermediate[a,b] Composition, g (wt %)	Final Composition, g
Run #1	100.42 U-Zr (21.75)	100.42 U-Zr (52.60)	129.33
	28.92 Pu (6.26)	28.92 Pu (15.15)	U-Pu-Zr[c]
	332.40 Cd (71.99)	61.56 Cd (32.25)	
Run #2	128.21 U (26.08)	128.21 U (75.28)	156.28
	28.07 Pu (5.71)	28.07 Pu (16.48)	U-Pu[d]
	335.19 Cd (68.21)	14.03 Cd (8.24)	

[a] X-ray diffraction analysis identified intermediate phases to be alpha-U and $PuCd_6$.

[b] Maximum heating temperature was 668°C for Run #1 and 702°C for Run #2.

[c] Product contained <150 ppm Cd and Be.

[d] Product contained 54 ppm Cd and 287 ppm Be.

Fig. III.8. Photograph of U-Pu-Cd Metal Ingot Obtained by Purification and Consolidation (ANL Neg. No. 5508 Frame 13)

C. Engineering-Scale Process Development

1. Dissolution of Spent Fuel

Small-scale laboratory tests with individual clad fuel segments showed that anodic dissolution of clad metal fuel is a viable method for dissolution. In these tests, single 1/4-in.-long uranium-zirconium pins inside of 1/4-in. O.D. SS cladding segments were anodically dissolved in an electrorefining cell in 2.5 hours when a current lead was attached to the cladding. The voltage used was sufficient to oxidize the heavy metal pin but leave the cladding shell intact. Based on the laboratory tests, anodic dissolution was chosen for scale-up to plant scale (10 kg batch size).

In the fuel dissolution step, uranium and plutonium metals are oxidized at the anode (fuel segments in the anode baskets), and uranium/plutonium chlorides are simultaneously reduced at the cathode (either a metal mandrel or a container vessel with its layer of cadmium). (The Cl^- balance is maintained.) Table III.7 shows the oxidation-reduction reactions for uranium, the bulk of the fuel. For the anode processes, reaction (1) is the normal oxidation of the fuel. The second reaction is a parasitic reaction which oxides U^{3+} to U^{4+}. This reaction occurs at the metal basket surfaces and on the metal surface of the cladding hulls. (A corresponding reaction U^{4+} to U^{3+}, reaction (4), occurs at the cathode.) This reaction results in no fuel

TABLE III.7. Anodic Dissolution Reactions

Anode		
(1)	$U^{\circ} - 3e \longrightarrow U^{3+}$	(USEFUL)
(2)	$U^{3+} - e \longrightarrow U^{4+}$	(PARASITIC)
(3)	$3U^{4+} + U^{\circ} \longrightarrow 4U^{3+}$	(USEFUL)
Cathode		
(4)	$U^{3+} + 3e \longrightarrow U^{0}$	(USEFUL)
(5)	$U^{4+} + e \longrightarrow U^{3+}$	(PARASITIC)

dissolution unless the U^{4+} ion is brought into contact with the fuel matrix in the anode. If the U^{4+} ion comes in contact with fuel metal in the anode, then anode reaction (3) occurs with resultant fuel dissolution. This was an important consideration in designing the anode baskets. Cylindrical baskets gave very low current efficiency since the U^{4+} ions formed on the outside shell of the basket could not be brought into contact with fuel and were reduced parasitically, reaction (5), at the cathode. With four prismatic baskets arranged on an anode shaft in the shape of a plus (+), each basket is following in the wake of another basket when the anode shaft is rotated, and the U^{4+} rich salt is continuously contacted with fuel as the salt flows through the openings in the basket shell. With this arrangement, current efficiencies of greater than 50% are achieved for the fuel dissolution process.

A schematic of the engineering-scale electrorefiner (32-in. diameter crucible), which is in operation, is shown in Fig. III.9. (In this figure, means of applying heat to maintain the operating temperature (500°C) in the cadmium and electrolyte is omitted.)

During the anodic fuel dissolution step, it was found that the overall electrorefining cell resistance was sensitive to the number of parallel conductors in the anode. This is shown in Fig. III.10 where the overall cell resistance is related to the number of conductors in the anode. Low cell resistance is important. The anode voltage is limited to -1.3 volt (to prevent corrosion of the cladding and basket materials), and the lower cell resistance allows the dissolution current to be increased. Results of tests are given in Table III.8. In these tests, the cathode was the cadmium pool in the bottom of the electrorefiner vessel (see Fig. III.9), and four baskets mounted on the anode shaft gave parallel circuits in the electrolyte.

Another important feature of anode design is the capability for removal of residual electrolyte (after dissolution) from the empty cladding hulls in the anode baskets. In the electrorefining cell, the vertical dimension between the top of the cell electrolyte and the bottom of the cell heat shield assembly is greater than the overall length of the anode basket. After dissolution is complete, the anode shaft is raised to lift the baskets

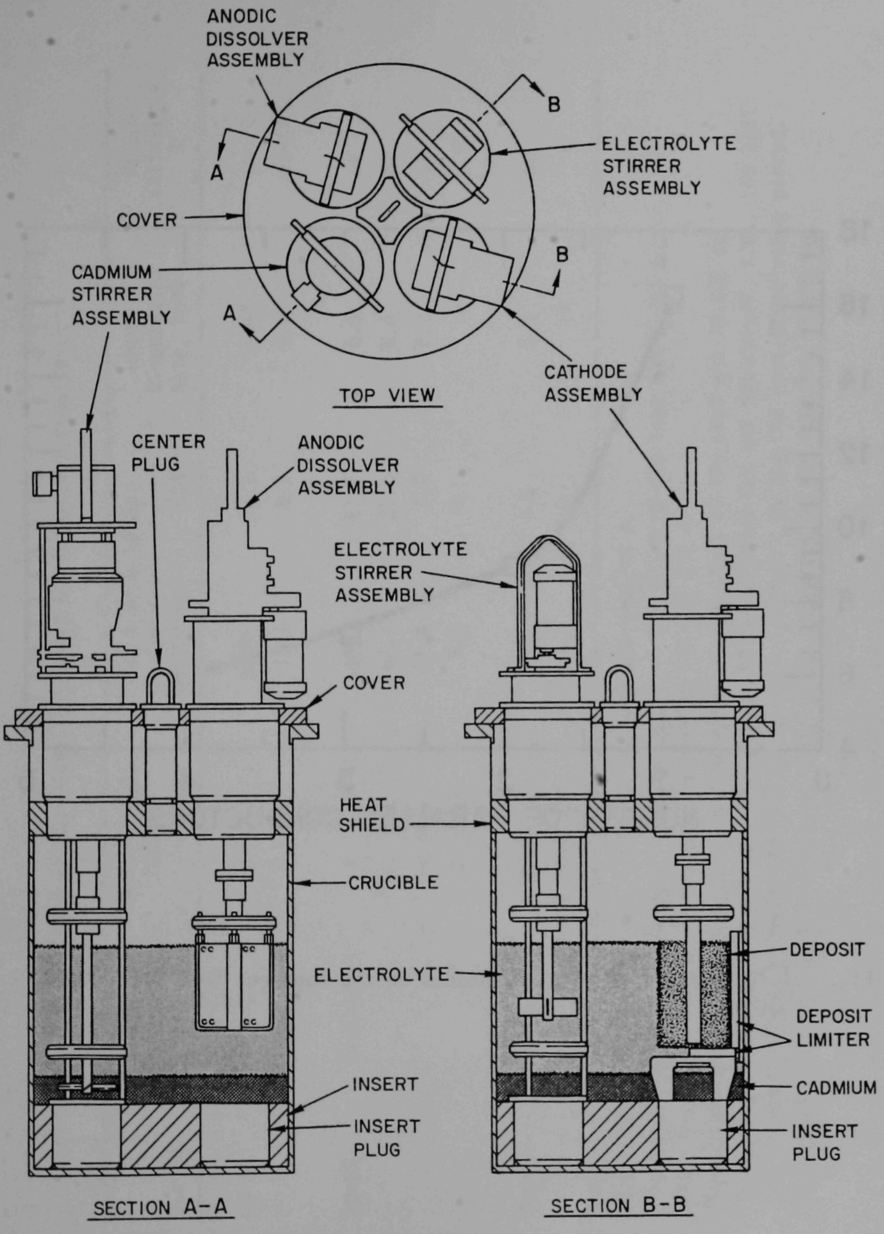

Fig. III.9. Electrorefining Cell

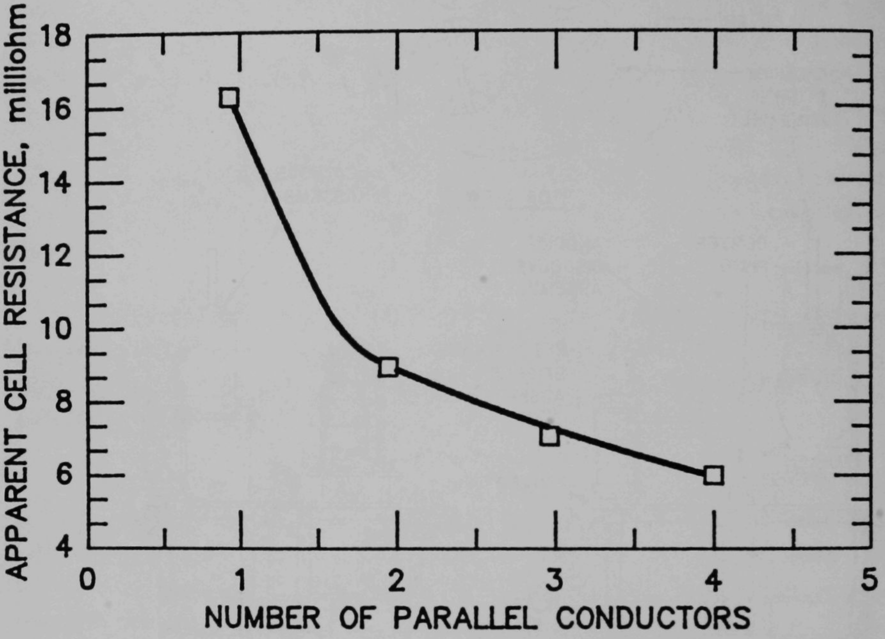

Fig. III.10. Effect of Parallel Anodes on the Apparent Cell Resistance

TABLE III.8. Parallel-Basket Anodic Dissolution Tests

Run No.	Chopped Pin Bed Depth, cm	Dissolution Period, h	Wt % of U-10 Zr		Uranium Dissolution Rate, kg/h	Anodic Efficiency, %
			Beginning	End		
AD-7[a]	8.9-9.5	8	100[b]	31.1	0.45	68-70
		4.3	31.1	8.1	0.3	55-57
AD-8[c]	17.8-19.7	6	100[d]	67.7	0.5	69
		11	67.7	21.6	0.4	51
		7	21.6	7.5	0.2	55
		7	7.5	0	e	e
AD-9[c]	22.2	26.75	100[f]	3.6	0.4	52
		2.2	3.6	0	e	e

[a] The dissolution current was typically between 150 and 200 A.

[b] The weight of uranium-10 wt % zirconium alloy at the start of the test was 5.215 kg.

[c] The dissolution current was typically between 200 and 250 A.

[d] The weight of uranium-10 wt % zirconium alloy at the start of the test was 10.202 kg.

[e] The exact time needed to electrotransport all of the uranium was not determined, i.e., the last bit of material was transferred at some undetermined point during the last dissolution period.

[f] The weight of uranium-10 wt % zirconium alloy at the start of the test was 11.108 kg.

out of the electrolyte, and then the basket assembly is rotated at about 250 rpm in this hot gas space inside the electrorefiner. The centrifugal force produced in the assembly strips residual liquid electrolyte from the baskets. This liquid electrolyte collects on the vessel walls and returns to the electrolyte pool. In a stripping experiment, one of the four baskets and its contained cladding hulls were water washed to remove residual salt after the spinning operation. About 15 g of salt was found, along with 0.02 g of fines. The heavy metal content of the salt electrolyte is 3.2 wt %, which means that the heavy metal content of residue in the four baskets is about 2 g. This is only a 0.02% process loss (anode baskets charged to dissolution contained 10 kg of uranium) in this cladding hulls waste. Since the cladding hulls are essentially salt free after the spinning operation, they are easily removed from the anode baskets, which are then recycled for reuse.

2. Dissolution of Irradiated Fuel

As discussed above, the anodic dissolution of unirradiated U-10 wt % Zr in stainless steel cladding has been successfully demonstrated in the engineering-scale electrorefiner at the 10-kg batch level. However, it was not certain whether these results are applicable to the dissolution behavior of irradiated fuels. For this reason, experiments with irradiated fuel (both anodic dissolution and electrotransport to solid cathodes) have been conducted using an electrochemical cell in the Hot Fuel Examination Facility/North (HFEF/N). One objective of irradiated fuel dissolution experiments is characterization of cladding hull waste resulting from the anodic dissolution. Of particular importance is the determination of the quantities of uranium, plutonium, and fission products remaining with the cladding hulls at the completion of the anodic dissolution operation. A preliminary measurement of these materials was obtained by the examination of 10 cladding hulls resulting from 10 anodic dissolution tests of single segments (1/4-in. long) of irradiated fuel from EBR-II. For these examinations, salt-coated anodes containing the fuel remnants (cladding and any remaining fuel) were sent to analytical laboratory hot cells for chemical analysis. Deionized water was used to dissolve away the salt coating the anode, allowing removal of the fuel remnant. Then, a series of washes with deionized water and dilute nitric acid combined with ultrasonic action was used to remove or dissolve material from the cladding. The "clean" hulls were then dissolved in strong acid. Solutions resulting from this procedure were analyzed for uranium and plutonium by mass spectroscopy. Radioactive fission products were measured by gamma-ray spectroscopy. Complete characterization of cladding hull waste will require analysis with a hot cell Inductively Coupled Plasma Atomic Emission Spectrometer (ICP) and an atomic adsorption instrument (AA).

The operating conditions for these experiments with single segments of irradiated fuel are summarized in Table III.9. Binary fuel, U-10 wt % Zr, was used in the first six tests. The last four tests were conducted using ternary fuel, U-19 wt % Pu-10 wt % Zr. Anodic dissolution of the fuel segment was complete, with only a small amount of fuel material remaining in the clad hull. The results of the analyses for any uranium, plutonium, and fission products remaining with the clad hulls are shown in Fig. III.11, where the percentage of the initial material remaining in the clad hull is plotted. The data show that essentially all of the plutonium and cesium and greater than 99.9% of the uranium and zirconium were removed in the anodic dissolution. The removal of the other fission products was slightly less complete.

The electrotransport of uranium to a solid cathode proceeded as expected. This result combined with the anodic dissolution behavior indicates that the electrorefining of irradiated fuel behaves very similar to the electrorefining of simulated fuels. Tests with irradiated fuels are continuing.

3. Electrotransport to Solid Cathode

A number of modes of operation are available for heavy metal product collection at a cathode. Solid cathodes are used to collect uranium, and liquid-cadmium cathodes are used to collect plutonium or plutonium/uranium. (The solid cathode excludes plutonium metal from the product.) Collection on the cathode has been done while the pool of cadmium in the vessel bottom (and hence the vessel wall since it contacts the cadmium) serves as an anode. This requires a previous step in which the pool of cadmium serves as a cathode during the anodic dissolution step. Collection on the cathode has also been done concurrently with anodic dissolution. This later mode of operation cuts

TABLE III.9. Test Conditions for Anodic Dissolution of Single Irradiated Fuel Segments

Test #	Fuel Type	Dissolution Time (h)	Initial Cell Voltage (V)	Initial Current (A)	Total Current (A-h)	Anodic Eff. (%)
AD-2	U-10 Zr	1.0	0.620	0.640	0.480	72.50
AD-2R	U-10 Zr	1.1	0.608	0.600	0.504	73.24
AD-3	U-10 Zr	1.3	0.510	0.400	0.650	77.99
AD-3R	U-10 Zr	1.2	0.510	0.400	0.453	77.12
AD-4	U-10 Zr	0.7	0.895	0.920	0.461	83.33
AD-4R	U-10 Zr	0.7	0.893	1.000	0.489	73.89
AD-5	U-19 Pu-10 Zr	0.7	0.893	1.100	0.510	73.45
AD-5R	U-19 Pu-10 Zr	0.7	0.898	1.250	0.524	72.74
AD-6	U-19 Pu-10 Zr	1.3	0.550	0.400	0.481	71.13
AD-6R	U-19 Pu-10 Zr	1.2	0.525	0.420	0.513	68.01

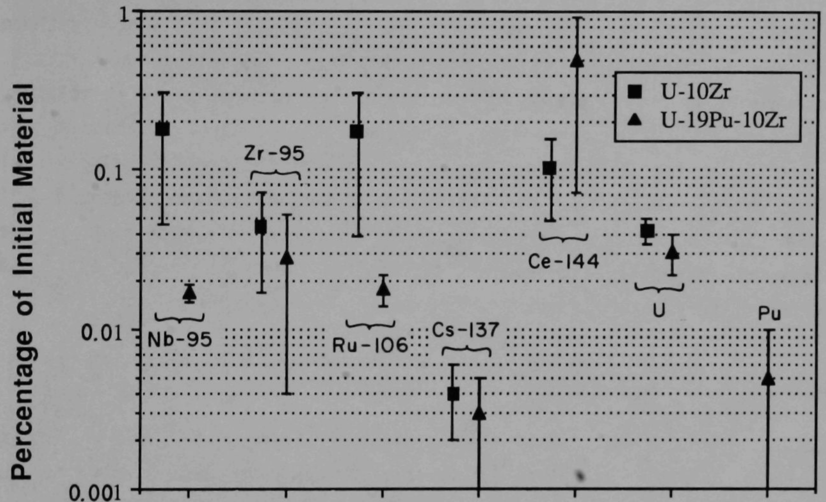

Fig. III.11. Fuel Material and Fission Products Remaining with Clad Hulls after Anodic Dissolution overall processing time since the dissolution and collection processes are occurring at the same time.

A single cylindrical iron mandrel (1-3/4 in. diameter x 12 in. long) has been used as a cathode. Multiple rods of uranium (each rod about 0.2 in. diameter) have been used as a multipin cathode. In the former, the dendritic deposit of heavy metal must be physically removed from the iron base mandrel in a product recovery step. In the latter, the uranium rods may be melt consolidated along with the dendrite deposit, and physical removal from the base cathode material is not required. Uranium deposits on a single cathode mandrel and on a multipin cathode are shown in Figs. III.12 and III.13, respectively. During formation of a cathode, the cathode shaft is rotated, and scrapers (BeO plates permanently located in the electrolyte phase) limit the overall diameter (8 in.) and length (13 in.) of the deposit. Individual dendrites which grow beyond these limits are broken off by the scrapers, fall into the cadmium pool, and are recycled. This continuous shaping of the cathode tends to densify it; however, current efficiency is lowered since the same material recycles from anode to cathode.

a. Single Mandrel Cathode

Table III.10 shows the results of three deposition runs using single solid cathodes. Run AD8/14 was carried out with anodic dissolution, from the anode basket, and cathode deposition occurring concurrently. In the

TABLE III.10. Results of Solid Cathode Tests

	Run Number		
	10	C-2	AD8/14
Weight of Uranium Deposited on Cathode, kg (kg/h)	6.9 (0.25)	6.0 (0.25)	5.7 (0.48)
Composition of Cathode Deposit, wt %			
Uranium	84.3	85.3	78.1
Salt	15.0	13.9	20.2
Cadmium	0.7	0.14	0.41

Fig. III.12. Photograph of 7-kg Deposit for Run AD-8 Direct Transport from Anodic Dissolution Baskets. (ANL Neg. No. 6279)

Fig. III.13. Photograph of Deposition on Multipin Cathode (ANL Neg. No. 6046) other two runs, deposition was carried out with the large cadmium pool (and crucible) as the anode, into which uranium was previously dissolved. In run AD8/14, for the cathodic circuit, part of the current passed through the solid mandrel, and part was split off and passed through the crucible wall/cadmium pool. This essentially gave two cathodes, parallel connected. This arrangement allowed the cell to be run at the highest current and resulted in the highest rate of deposition on the solid cathode, 0.48 kg HM/h.

b. Multiple Pin Cathode

Table III.11 gives the results for six deposition runs with multipin cathodes. In the tests both steel and U-10 Zr rods were used. Rod arrangement patterns in the cathode were either circular or cruciform. The number of rods was varied from 5 to 13. Runs were made under various stirring conditions in the anode pool and the electrolyte, including the condition of no stirring at all (other than that due to cathode rotation). Half the runs were made at one uranium concentration in the electrolyte; in the other half, the uranium concentration was doubled. Collection efficiency (rate of collection) was not greatly affected by any of the variables except the stirring rate, with the highest rates being obtained when the salt mixer and anode cadmium mixer were at 0 rpm. Stirring causes dendrite loss (with subsequent recycle) from the cathode deposit.

4. Electrotransport to Liquid Cadmium Cathode

Plutonium or plutonium/uranium is collected in a cadmium pool contained in a ceramic crucible suspended in the electrolyte phase. To keep reasonable size, it is necessary to collect an amount of plutonium in the cadmium pool in excess of the solubility of plutonium in cadmium (3.62 wt % at 500°C). When plutonium exceeds its solubility in liquid cadmium or liquid cadmium-uranium, it precipitates as $PuCd_6$, an intermetallic compound. In small-scale laboratory work (0.2 kg plutonium scale), cadmium cathodes have been produced which contain about 15 vol % plutonium solid. For a plant-scale electrorefiner, the 10 kg HM fuel batch will contain about 2.0-2.5 kg plutonium. A cathode pool containing about 30 kg of cadmium is required for this plutonium collection (a 5 L ceramic crucible is required).

TABLE III.11. Results of Multipin Cathode Tests

	Run Number					
	15	C-1	19	24	27	30
Total Deposit Weight, kg	4.8	7.0	10.2	9.2	11.0	8.4
Weight of Uranium, kg	3.6	5.6	8.4	7.4	9.7	a
Collection Rate, kg/h	0.18	0.23	0.24	0.22	0.20	a
Composition of Cathode Deposit, wt %						
Uranium	76.3	79.8	81.8	79.9	88.6	a
Salt	23.3	19.1	17.8	13.9	9.9	
Zirconium	0.21	0.9	0.4	5.2	1.3	
Cadmium	0.18	0.12	<0.01	0.4	0.2	

[a] Has not been determined; samples of this deposit were submitted for chemical analysis.

Table III.12 shows the results of runs in which uranium was deposited into cadmium in a 3 L crucible. Figure III.14 shows a cross section of one of the cadmium-uranium ingots. For this work, uranium is used as a stand in for plutonium, since the glovebox in which this engineering development work was carried out is not a plutonium facility. Since uranium does not form an intermetallic compound with cadmium when the uranium solubility is exceeded at operating temperature (500°C), a higher (U/Cd) ratio is required to form the same volume percentage solids in the cadmium as for the case of (Pu/Cd). For the three runs, the amount of uranium solids in the cadmium ingot was 10-14 vol %. In these particular runs, the cadmium phase in the cathode crucible was not stirred; the electrolyte phase was stirred with a ceramic agitator. When the product ingots were removed from the crucible, the cadmium ingots were coated with electrolyte, which did not separate easily from the cadmium. The amount of electrolyte varied from 1.5 to 5 wt % of the product ingot.

The highest deposition rate attained in the cadmium cathode deposition runs was 0.054 kg/h (run LCC-1). For the case of plutonium this needs to be improved to about 0.08 kg/h to complete the fuel batch in 24 hours. Improvement in the rate is expected when the deposition is done into a slightly larger cadmium pool (increased cadmium-electrolyte interfacial area) and when the deposition is done concurrent with dissolution, as found for the solid cathode.

5. Direct Chemical Reduction

Plutonium/uranium may also be deposited into the cadmium pool by chemical means. Lithium reductant introduced into the cadmium crucible pool reduces $PuCl_3$ and UCl_3 out of the electrolyte and deposits the metal in the cadmium pool. Development work on this alternative has started and is in a preliminary stage. The reaction for the reduction is extremely fast, but reduction can take place in the electrolyte phase (lithium metal is slightly soluble in the electrolyte) away from the cadmium-electrolyte interface. Cathode designs and operating procedures are being developed to confine the reaction space and to cause the reduced heavy metal to consolidate into the cadmium pool.

TABLE III.12. Electrorefiner Electrodeposition of Uranium into Liquid Cadmium Cathode, 500°C

	LCC-1	LCC-2	LCC-3
Electrodeposition Current, A	25	26	25-30
Cutoff Voltage, V	-1.0	-1.0	-1.0
Electrodeposition Time, h	56	68	130
Cathodic Efficiency, %	73	54	46
Dendrite Braker Speed, rpm	±270	±(20-270)	±(20-200)
Cadmium Cathode Load, kg	8.7	12.5	12.2

Composition of Cathode Product

	LCC-1[a]			LCC-2[a]			LCC-3		
	kg[a]	L	vol %	kg[a]	L	vol %	kg	L	vol %
Cadmium	7.1	0.91	86	9.1	1.16	90	12.8	1.64	88
Uranium	3.0	0.15	14	2.8	0.13	10	4.4	0.22	12
Electrolyte	0.3	0.16		0.2	0.12		0.9	0.51	

[a] Composition of the product after free cadmium and salt had drained from the cathode crucible.

Fig. III.14. Photograph of LLC-3 Sectioned Product
(ANL Neg. No. 5384 Frame 12)

Results for the preliminary work on chemical reduction are given in Table III.13. In two of the runs (CRU-1 and -2) agitation was provided at the salt-metal interface within the reaction crucible. In two of the runs (CRU-3 and -4) agitation was not used. Best results were obtained in the run without agitation (CRU-3). For this run, all of the uranium equivalent to the amount of reductant used was found in the metallic phase of the product, which was contained within the alumina crucible (see Fig. III.15). In the run with agitation, much of the uranium was found in material which overflowed the crucible or which was bonded to the impeller.

D. Waste Treatment Processes

1. Waste Flowsheet

Methods for recovering transuranic elements from the pyroprocessing wastes and packaging the treated wastes for disposal are being developed. The principal high-level radioactive wastes are (a) gaseous fission products, (b) cladding hulls, (c) salt from the electrorefiner, and (d) cadmium from the electrorefiner. The salt and cadmium discharged from the electrorefiner contain nearly all of the nongaseous fission products, with the alkali metals, alkaline earths, rare earths, and halides in the salt and the noble metals in the metal wastes. This salt also contains 0.5 and 1% of the actinides fed to the electrorefiner. The actinide contents of the waste metal and the cladding hulls are expected to be very low.

The gaseous fission products (tritium, krypton and xenon) are released into the argon atmosphere of the processing cell and recovered by commercially available techniques. The solid wastes are treated by the process scheme shown in Fig. III.16. In this process, the salt from the electrorefiner is first contacted with a Cd-U alloy to extract nearly all of the transuranic elements from the salt while leaving most of the rare earths in the salt. The resulting metal solution is retorted to remove cadmium, and the TRU-rich residue is returned to the electrorefiner. The salt, which now contains only trace amounts of TRU elements, is contacted with a Cd-Li alloy

TABLE III.13. Results of Direct Chemical Reduction Tests

					Product					
	Starting Material, kg						Composition, wt %			
Run No.	Li-Cd[a]	(U_{eq})	Cd	LiCl-KCl	Location	Description	Uranium	Cd	Salt	Uranium Wt., kg
CRU-1[b]	1.221	4.0	8.012	0	Impeller[c]	Brittle	32.2	51.9	15.9	2.187
					Cd Pool	-	-	-	-	1.25
					BeO Crucible	Metallic	11.4	88.2	0.4	0.159
										3.6 TOTAL
CRU-2[d]	1.227	4.0	12.0	0	BeO Crucible	UCd_{11}[e]	23.4	71.6	5.0	2.768
					Supp. Hdw.	-	15.5	81.5	3.0	0.515
					Impeller	-	23.4	71.6	5.0	0.181
					Cd Pool	-	-	-	-	0.225
										3.7 TOTAL
CRU-3[f]	0.518	1.7	5.053	1.708	Alumina Cruc.	Metallic	21.3	67.9	10.8	1.7
CRU-4[f]	1.133	3.7	4.672	1.274	Alumina Cruc.	Metallic	12.8	-	-	1.0
					Supp. Hdw.		13.1	-	-	0.1
					Cd Pool		-	-	-	2.6[g]

[a] 28.6 wt % lithium-cadmium alloy.

[b] Double-bladed metal impeller provided mixing in Cd and salt in ceramic crucible.

[c] Product was attached to impeller and withdrawn from crucible when impeller was removed.

[d] Alumina impeller provided mixing at salt/Cd interface.

[e] Appearance was identical to products found in LCC tests and identified as UCd_{11}.

[f] No mixing in crucible.

[g] This uranium was deposited in the cadmium pool and on the walls of the electrorefiner.

Fig. III.15. Photograph of CRU-3 Product from Alumina Crucible (ANL Neg. No. 6659)

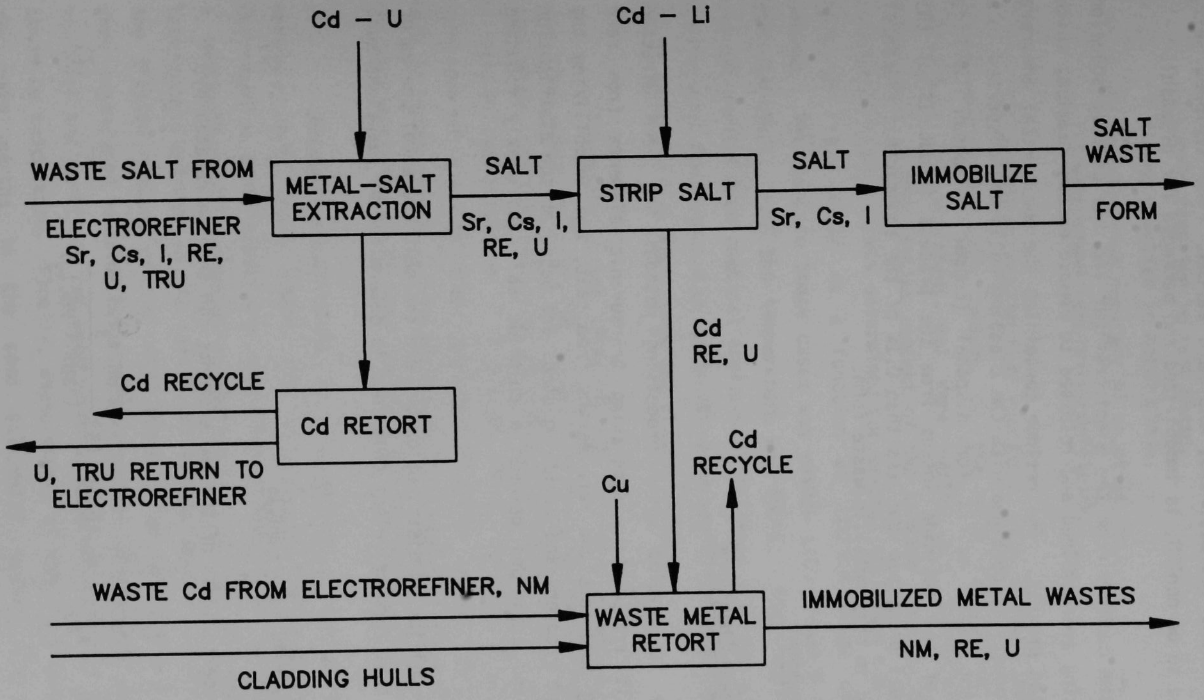

Fig. III.16. Reference IFR Waste Treatment

RE = rare earth fission products
NM = noble metal fission products
TRU = transuranic elements

to strip away uranium, residual TRU, and rare earths. The stripped salt, which is expected to be nonTRU, is immobilized and packaged for disposal.

The waste cadmium from the electrorefiner and the cadmium solution from salt stripping are combined and retorted to remove excess cadmium, which is returned to the process. The residue containing the noble metal and rare earth fission products is combined with the cladding hulls and dispersed in a corrosion-resistant metal matrix for disposal (copper is shown in Fig. III.16). Most of the actinide losses from the process (about 1% of the uranium in the fuel processed and less than 0.1% of the transuranic elements) will be contained in this metallic waste form.

2. Salt Treatment

a. Process Chemistry

Work to develop waste processing methods has been directed primarily to salt treatment: separating transuranic elements from rare earths, stripping actinides and rare earths from salt, and immobilizing the treated salt. The recovery and stripping steps are based on the distribution of rare earths and actinides between a chloride salt and weakly reducing cadmium alloys.

The equilibrium distribution between the salt and metal phases of any two elements that form trivalent chlorides is determined by reactions such as:

$$PuCl_3 + Nd = Pu + NdCl_3 \qquad (1)$$

The distribution coefficients of the two elements can then be related by:

$$D_{Pu} = \frac{y_{PuCl_3}}{x_{Pu}} = (D_{Nd}) \; (K) \; \frac{(\gamma_{NdCl_3}) \; (\gamma_{Pu})}{(\gamma_{Nd}) \; (\gamma_{PuCl_3})} \qquad (2)$$

where: D = distribution coefficient,
y = mole fraction in salt phase,
x = atom fraction in metal phase,
K = equilibrium constant of reaction, and
γ = thermodynamic activity coefficient.

If analogous equilibrium reactions with lithium are considered in systems where the LiCl content of the salt is constant, distribution coefficients of actinides and rare earths are approximately inversely proportional to the lithium content of the cadmium phase to the third power. Distribution coefficients determined for several actinides and rare earths are shown in Fig. III.17 as a function of lithium metal concentration in cadmium. The salt in these cases was either LiCl-42 mol % KCl or LiCl-29% $CaCl_2$-18% $BaCl_2$, and the temperature was 500°C. Distribution coefficients were determined from chemical analyses of filtered salt and metal samples for coefficients from about 0.01 up to 50 where analytical results were reliable; values shown outside that range are extrapolations.

The slope of the lines in Fig. III.17 is slightly greater than the -3.0 that would be predicted because the activity coefficient of lithium in cadmium was found to depend on lithium concentration, varying from 1.6×10^{-3} at a lithium concentration of 0.013 at. % to 3.7×10^{-3} at 6.1 at. %. The curvature of the americium line was attributed to the formation of $AmCl_2$ in more reducing systems. Neptunium distribution coefficients were not measured but were estimated to be less than the uranium coefficients.

Because measurements of lithium concentrations in cadmium were accurate only above about 0.04 at. %, the relationships between the distribution coefficients and lower lithium concentrations were established by a combination of extrapolation techniques. First, the emf of an Ag||AgCl reference electrode in the salt-metal system was determined as a function of the lithium content of the metal phase. The rare earth distributions were then correlated with lithium concentrations determined partly by chemical analyses and partly by emf measurements, from which the lithium concentration could be calculated. Finally, measurements of the distributions of actinides and rare earths in the same salt-metal system allowed the actinide coefficients to be related to the lithium content.

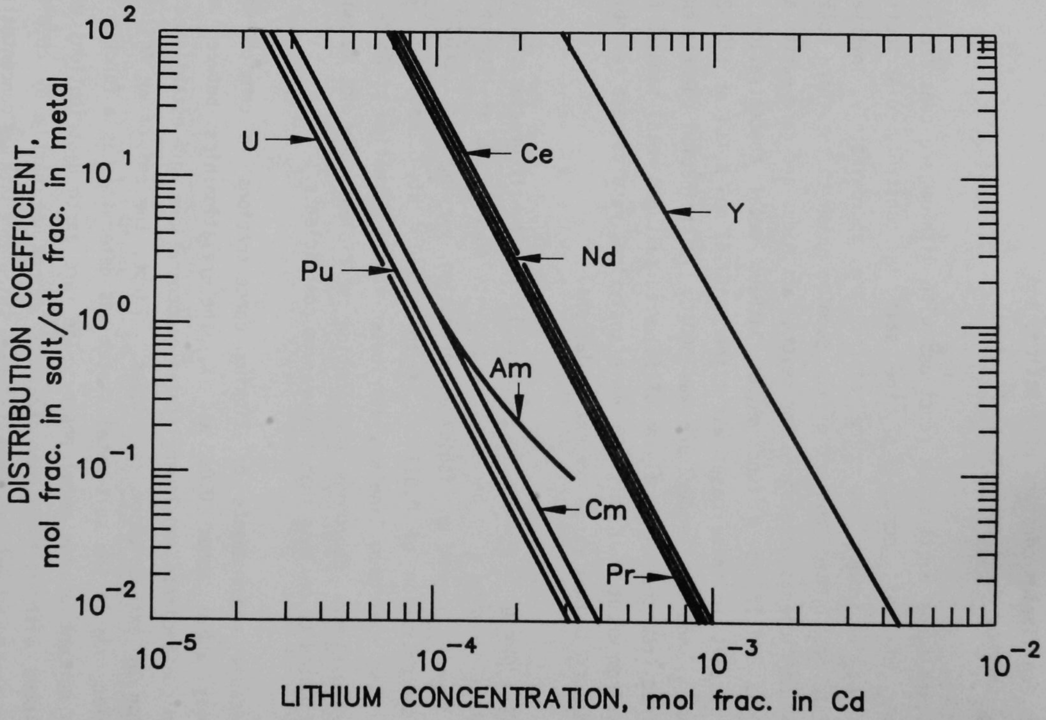

Fig. III.17. Distribution Coefficients of Actinides and Rare Earths between Chloride Salts and Cadmium-Lithium Alloys at 500°C

b. Salt Stripping

The data in Fig. III.17 show that the actinide and rare earth content of the chloride salt can be made extremely low by contacting the salt with a cadmium alloy containing only about 1.5 at. % lithium (0.1 wt %). This has been demonstrated in laboratory experiments in which the actinide and rare earth contents of a salt were reduced from the 0.1 to 1.0 wt % range to the ppm range in a single contact with a Cd-0.1 wt % Li alloy. The residual actinide content (U ~ 10 ppm, Pu ~ 1 ppm) was attributed to small particles of insoluble oxides. The removal of a large fraction of such insoluble compounds by passing the salt through stainless steel filters was also demonstrated on a laboratory scale.

c. TRU Recovery

Because of the large differences between the distribution coefficients of actinides and rare earths, as shown by the data in Fig. III.17, actinides can be separated from rare earths by extraction processes in this salt-metal system. Such processes are best carried out where the actinide distribution coefficients are about 1.0, and consequently, a practical extraction process cannot depend on controlling the lithium content of the metal phase because it would have to be so low. However, transuranic elements can be separated from rare earths by an extraction process that employs Cd-U alloys as the extractant. When a salt containing uranium, transuranics, and rare earths is contacted with a Cd-U metal solution, uranium in the metal phase will exchange with the transuranics and rare earths in the salt to establish metal phase concentrations as required by the relationships among the distribution coefficients. The fractions of transuranic elements extracted from the salt will be greater than the fraction of rare earths extracted. Calculations have shown that more than 99.9% of the americium and less than 20% of the neodymium would be extracted from a waste electrorefiner salt in 5 to 6 equilibrium stages of countercurrent contact with a metal/salt weight ratio of 3 to 5.

3. Salt Immobilization

The stripped waste salt will contain less than 1 ppm of total actinides (<100 nCi/g of alpha activity) and very low levels of radioactivity from rare earth fission products, but it will contain nearly all of the fission product cesium, strontium, and iodine. Consequently, the salt must be suitably immobilized and encapsulated to meet the Federal regulations for disposal of high-level radioactive wastes[1]. The salt waste form must be encapsulated in metal containers that are sufficiently resistant to internal and external corrosion that they will not be penetrated by repository groundwater for several hundred years. The salt, being easily dissolved in water, must be immobilized to retard dispersion during shipping and handling and leaching of radioisotopes from the repository into groundwater. Even though Sr-90 and Cs-137 will have decayed to low levels when the containers are finally penetrated by repository groundwater, the salt dissolution process must be gradual[2]. In addition, the waste form must make a significant contribution to the leach resistance of the engineered barriers so that the leach rate[3] of the remaining radioisotopes from the overall system of engineered barriers will be less than 0.001%/y.

Attempts were made to convert chloride salts to glassy materials similar to one of the reference waste forms for high-level wastes. The salt was reacted at high temperatures with steam and oxygen to remove the chlorine as HCl and to convert the solids to oxides. Another reactant, such as SiO_2 or B_2O_3, was necessary to make this reaction approach completion. At temperatures above 700°C, essentially all of the chlorine could be removed in 4 h from a mixture of LiCl-42 mol % KCl salt, SiO_2, and H_3BO_3. The product was a glassy material that was insoluble in water. However, the gaseous reaction products were extremely corrosive; quartz tubes with platinum liners were destroyed within a few hours.

Because of the severe materials problem with this approach, other means of immobilizing the waste salt are being sought. Dispersal of the salt in a portland cement-base mortar has been investigated. A mortar made from 25% Type I portland cement, 25% Class F fly ash, and 50% blast furnace slag with a water/solids ratio of about 0.4 was found to be strong and to have a high resistance to leaching when containing up to 10 wt % LiCl-KCl. Grouts containing up to 15 wt % salt were sufficiently fluid that they could be mixed and pumped into waste canisters, and set times were longer than 8 h, which would allow ample time for mixing and casting into canisters. Held at room temperature, the mortar strength reached 20 MPa in 7 d and exceeded 40 MPa after 56 d. Waste forms that cured at temperatures up to 125°C due to fission product heating would have higher early strengths, but their long-term strengths would be lower by 10 to 20%. These strengths would be adequate for waste forms cast into steel canisters. Mortars without blast furnace slag achieved similar strengths at room temperature, but at higher temperatures their long term strengths were considerably less.

Leach rates from these mortar formulations were measured by the ANS 16.1 procedure[4], in which a cylindrical specimen (2 cm dia by 4 cm long) was suspended in 200 mℓ of distilled water. Periodically, the specimen was removed and placed in a fresh volume of water, and the leachate was analyzed for chloride ion. From these data, an effective diffusivity of chloride ions from the specimen was calculated, and this parameter was used to predict the leach rate from a large waste form. From the measurements, it was estimated that only 20 to 25% of the chloride salt would be leached from a salt-mortar waste form the size of a 55-gal drum if it were immersed in flowing water for 100 y. The fractions of the cesium and strontium leached would be lower because these ions leach more slowly from mortars than lithium and potassium. Without blast furnace slag in the mortar, the leach rates would be two to three times higher.

The strength and leach resistance of salt-mortar waste forms appeared to be adequate for a high-level waste form, but the water in the mortar can be decomposed by beta-gamma radiation from fission products. A mortar containing 7 wt % of waste salt would receive an initial dose rate of about 0.05 Mrad/h from Sr-90 and Cs-137, and a total dose of about 5×10^4 Mrad. Studies were conducted with a Co-60 source to determine the effects of radiation on the mortar formulations being considered for immobilizing IFR waste salt. In these experiments, the radiolytic pressurization was monitored during the irradiation, and the gas phase was analyzed at the conclusion of the test.

Irradiation of mortars consisting of cement, fly ash, chloride salts and water produced no significant amounts of HCl or chlorine but did produce high pressures of hydrogen and oxygen. When blast furnace slag was included in the mix, only hydrogen was produced. The rate of hydrogen production was constant and steady state pressures were not attained up to a total dose of 500 Mrad. Hydrogen yields depended on salt content; at 25°C, the $G(H_2)$ was 0.14 molecules/100 eV for a mortar containing 3 wt % salt and 0.22 for a mortar with 10 wt % salt. Hydrogen yields decreased with increasing temperatures; for a mortar containing 10 wt % salt, hydrogen yields were 40% lower at 75°C than at 25°C, and 90% lower at 120°C.

The studies indicated that hydrogen yields from slag-containing mortars were high because back reactions and recombination reactions between the precursors of molecular hydrogen (the hydrated electron and hydrogen radicals) and hydroxyl radicals were not competitive with hydroxyl radical scavenging reactions with species in the mortar. Some scavengers were believed to be reduced sulfur species, chloride ions, and neutral or singly charged chlorine molecules. Since the leach resistance and compressive strength of this mortar were promising, additional experiments were conducted to determine if hydrogen yields could be lowered. The approach was to add small amounts of oxygen-rich electron scavengers, such as NO_3^- and IO_4^-, which should cause a decrease in hydrogen yields because they should react with the hydroxl scavengers. As illustrated in Fig. III.18, the addition of 1 wt % $NaNO_3$ to a salt-mortar specimen decreased the radiolytic pressurization rate and reduced the amount of hydrogen produced. The radiolysis products were changed from only hydrogen to hydrogen, nitrogen, and N_2O. The addition of 1 wt % $NaIO_4$ decreased the pressurization rate but did not change the radiolysis products. Further studies are underway to identify other electron scavengers that will lower hydrogen yields but will not decompose to other gaseous products.

Although it may be possible to solve this radiolysis problem, for example, by adding electron scavengers or venting waste containers, other salt waste forms are being investigated, especially those that contain no water. The simplest approach is encapsulation of the salt in highly corrosion-resistant, thick-walled metal containers or porous metal matrices. Studies

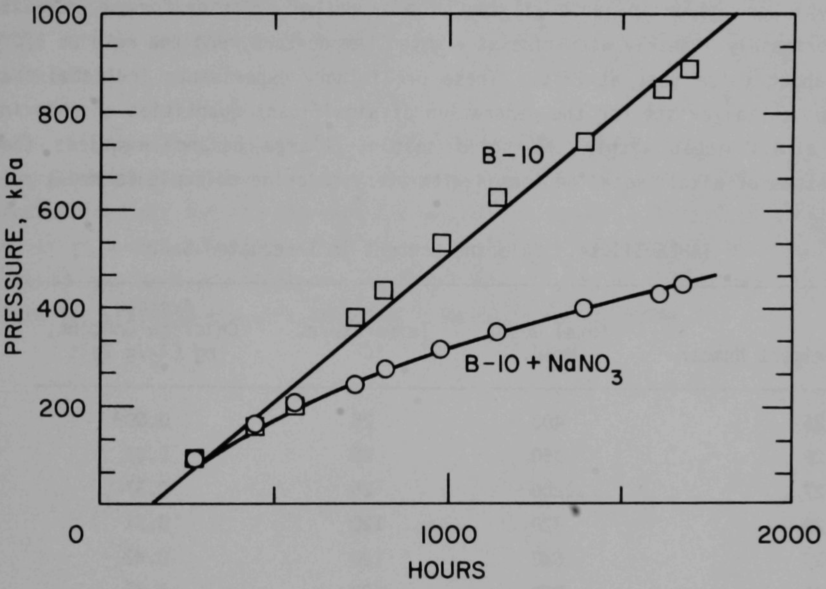

Fig. III.18. Decrease in Radiolytic Pressurization by the Addition of $NaNO_3$ to Salt-Mortar Specimens

B-10: Mortar with slag and 10 wt % salt

B-10+$NaNO_3$: Mortar with slag, 10 wt % salt and 1% $NaNO_3$

are being conducted to determine the effects of ionizing radiation on solid IFR waste salt during interim storage and long-term disposal. Solid salt consisting of 95.7 wt % of LiCl-42 mol % KCl, 1.1 wt % $BaCl_2$, 1.4 wt % $CaCl_2$, and 1.2 wt % NaCl was irradiated for periods ranging from 1 to 3 months at dose rates between 0.4 and 0.6 Mrad/h and at 25 and 120°C. After irradiation the salt had changed color from white to deep purple or black. The irradiated salt was analyzed iodometrically for chlorine content. The results of these analysis are given in Table III.14. The amount of chlorine formed increased approximately linearly with time at a given temperature, and the rate at 120°C was about twice that at 25°C. These preliminary experiments indicated that the potential exists for the generation of significant quantities of chlorine and alkali metal within the solid salt. (Charge balance requires that two atoms of alkali metal be formed with every chlorine molecule formed.)

TABLE III.14. Chlorine Content in Irradiated Salt

Experiment Number	Total Dose, Mrad	Temperature, °C	Average Chlorine Content, mg Cl_2/g Salt
25	400	25	0.093
26	960	25	0.23
27	1200	25	0.37
29	320	120	0.21
30	640	120	0.42
31	960	120	0.66

4. Planned Waste Studies

In the near term, development of waste processes will continue to emphasize methods for treating and immobilizing salt wastes. The work on salt-mortar waste forms will be completed with the measurement of cesium and strontium leach rates and determination of additives that reduce the production of radiolytic hydrogen. Future experiments related to the storage and disposal of solid salt will be conducted to identify and evaluate container materials which are radiation and corrosion resistant with respect to chlorine, alkali metals, and chloride ion. Long-term experiments are also being planned to determine if chlorine generation reaches a steady state.

Immobilization of salt in water-free ceramic matrices will also be explored. In this approach, the salt would be absorbed into a porous ceramic, sealed in a metal container, and then hot-isostatically pressed to at least partially seal the ceramic pores. The possibility of incorporating a zeolite in the ceramic to preferentially adsorb cesium and/or strontium ions will also be explored.

Equipment to carry out salt-metal extractions and salt stripping is being designed. A salt stripper would be a stirred vessel with means of transferring salt and cadmium into and out of the vessel. The extractor would consist of a bank of several centrifugal contactors with counter current flow of metal and salt and means of feeding these fluids at controlled rates. Initially, a single-stage contactor will be built and operated.

References for Section III

1. U. S. Code of Federal Regulations, Title 10, Part 60, "Disposal of High-level Radioactive Wastes in Geologic Repositories; Licensing Procedures" (September 30, 1989).

2. Ibid, Paragraph 60.113 (a)(1)(i).

3. Ibid, Paragraph 60.113 (a)(1)(ii).

4. "Measurements of the Leachability of Solidified Low-Level Radioactive Wastes - Draft," American Nuclear Society Standards Committee, Working Group ANS 16.1, Washington, D.C. (February 6, 1986).

IV. SAFETY EXPERIMENTS AND ANALYSES

A. IFR Safety Features

Performance of IFR metallic fuel in normal and accident situations is a direct result of its favorable thermal, mechanical, and neutronic properties. These properties assure optimal safety response in design basis transients, anticipated transients without scram, and severe accidents, as well as in normal operation where local faults contribute to cladding failures.

1. Thermal and Mechanical Performance

Many of the superior safety performance characteristics of the IFR ternary alloy fuel design can be traced to its thermal and mechanical properties, with the most important of these being its high thermal conductivity. At operating temperatures, typical fresh IFR fuel has a thermal conductivity of around 20 W/m-°C. This yields a very low radial temperature rise across the fuel at operating conditions (less than 200°C), and a comparatively low stored heat.

The low radial temperature gradient across the fuel gives a correspondingly small zero-power to full-power Doppler reactivity swing, resulting in reduced control reactivity requirements and less excess reactivity available for accidental insertion. The low operating temperature also yields a smaller positive Doppler reactivity input in transients where power is reduced. For unprotected transients such as loss-of-heat-sink (LOHS) and loss-of-flow (LOF), this permits other naturally occurring negative reactivity feedbacks, such as axial and radial core thermal expansion, to overcome the positive Doppler component, resulting in self-adjustment of the reactor core power to equal available decay heat removal capacity.

The peak operating temperature for metallic fuel is about 725°C. This results in low stored heat, leading to reduced system heating in multiple-fault accidents and allowing increased time for operator action to correct flow or cooling deficiencies. Although the melting temperature for IFR fuel is relatively low (around 1125°C), the homologous temperature at operating conditions is nearly the same as for oxide fuels. Phenomena depending on diffusional rate processes, such as creep and fission gas release, are similar for the two fuel types.

Under accident conditions, transient heating of metallic fuel produces cladding loading dominated by the plenum pressure. The similarity of the fuel and the cladding thermal expansion and the compliance of the porous fuel lead to negligible fuel-cladding mechanical interaction (FCMI) cladding damage. Although the FCMI stresses in the cladding may be significant early in the transient, little plastic strain accumulates before fuel creep relaxes the cladding loading to a hydrostatic state that follows the transient increase in plenum pressure. (See Section IV.D for additional discussion.)

Should the accident sequence proceed to fuel melting, the high fuel porosity, low gas retention, and small fuel density decrease on melting lead to little pressurization of the pin before melting at the top of the fuel column allows molten fuel to expand into the plenum region. Besides delaying fuel failure (to about four times nominal power in an 8-sec-period overpower transient), this molten fuel extrusion can provide a significant source of negative reactivity feedback. (See Section IV.E for additional discussion.)

Metallic fuels interact metallurgically with iron-based cladding materials to form relatively low-melting point compositions. During normal operation, the rate of solid-state interdiffusion in metallic fuel is no greater than the wastage in ceramic pins due to fission product attack of the inner cladding wall. During transient heating, cladding penetration by low-melting liquid fuel-cladding compositions can contribute to cladding failure. However, the effect appears to weaken the cladding only by thinning the wall. The smaller transient cladding loading in metallic fuels reduces the impact of this decrease in strength.

2. Neutronic Performance

The metallic fuel core offers favorable neutronics properties. Specifically, the absence of low mass moderating atoms in the fuel leads to a harder neutron energy spectrum, increasing the neutron production per neutron absorbed in the pin. This occurs both because of the higher average number of neutrons emitted per neutron absorbed, η, for Pu^{239} with the harder neutron spectrum and because of the enhanced fast fission in U^{238}. The combined effect increases the number of neutrons available for breeding. Moreover, the effective heavy metal density is increased by use of the metallic fuel relative to the traditional oxide fuel form. Both of these characteristics can be used to increase core internal conversion ratio--to a point where zero burnup reactivity swing is achievable.

The harder neutron spectrum with the metallic fuel form has two important effects on reactivity feedback coefficients. The negative Doppler reactivity coefficient, $T \frac{dk}{dT}$, is reduced by about a third relative to oxide systems. The positive sodium density coefficient becomes more positive by about 30%. The net effect of the lower temperature rise across the pin radius and the shifts in reactivity coefficients is to make the component of the power coefficient which is vested in the coolant temperature rise larger than that which is vested in the fuel temperature rise. This partitioning of the power coefficient components (which is opposite to that of oxide fuel) is the key to the favorable passive reactivity shutdown response attainable in the IFR.

3. Design Basis Transients

The design basis accidents, including anticipated, unlikely, and some extremely unlikely transients, have been evaluated for the IFR concept. Those events lead to consequences well within conservatively interpreted acceptance guidelines when "traditional" values for the plant protection system (PPS) setpoints are used. The improved passive safety capability of the pool configuration and the improved reactivity feedback response of the metal fuel lead to the availability of large design margins. In pool systems, the large primary system heat capacity buffers the primary system so that no reactor scram is required for any combination of balance-of-plant BOP faults. In metal-fueled reactors, the reactivity decrement associated with changing power level is small compared to oxide-fueled reactors. These basic characteristics and the availability of large margins can be used to develop simplifications in the plant protection system (PPS) and plant control system

(PCS) configurations and a new optimum control strategy that could lead to reductions in event frequencies and scram demands.

4. Anticipated Transients Without Scram

In the full spectrum of unprotected accidents, three specific initiators have emerged to serve as quantifiers of safety margins. They are: (1) the loss-of-flow (LOF) accident, in which power to the coolant pumps is lost, (2) the transient overpower (TOP) accident, in which one or more inserted control rods are withdrawn, and (3) the loss-of-heat-sink (LOHS) accident, in which feedwater supply to the steam generators is lost. For all three initiators, it is also assumed that the plant protection system fails to insert the shutdown control rods. These events are generally classed as anticipated transients without scram (ATWS). The key to successful prevention of core disruption under these conditions is the provision in the design for reactor performance characteristics that (1) limit mechanisms leading to reactor damage, and (2) promote mechanisms responding to the upset condition and acting to restore the reactor power production/cooling balance. An example of the first is the minimization of the control rod worth, to limit the inserted reactivity in the transient overpower TOP accident. This is achieved by maximizing the breeding potential and conversion of fertile uranium into fissile plutonium. This reduces the total burnup reactivity swing, the control reactivity requirement, and thus the available insertion reactivity.

In all three of the ATWS accidents, the key to avoidance of short-term core disruption is to maintain the coolant outlet temperature below its boiling point. At normal operating conditions, the core inlet temperature is around 350°C, and the average coolant temperature rise through the core is around 150°C. To avoid coolant boiling, the transient, normalized power-to-flow ratio must be kept below about 4 in order to keep the core-average coolant outlet temperature below the boiling point of sodium at around 925°C.

In the long term, the overall negative reactivity feedback will tend to bring the reactor power into equilibrium with the available heat rejection rate, and the system will approach an asymptotic temperature distribution. To avoid core disruption in the long term, it is necessary that the peak asymptotic temperatures in strategic components (reactor vessel, core support structure, fuel cladding) be maintained below levels at which creep could cause failures.

Avoidance of both short- and long-term core disruption in ATWS events depends on (1) providing sufficient negative reactivity feedback to overcome the power-to-cooling mismatch and return the system to equilibrium at slightly elevated system temperatures, or alternately (2) reducing the positive reactivity feedback components acting to resist the transition to system equilibrium. In this second respect, metallic fuel provides superior safety performance in ATWS events, due to the small stored Doppler reactivity associated with the low fuel temperature.

The detailed IFR responses to the anticipated transient without scram events are given in Section IV.C. Full scale unprotected loss-of-flow and loss-of-heat-sink transients without scram have been carried out in EBR-II. These tests have confirmed the capability of the metal-fueled-IFR concept to respond to unscrammed accidents without core upset (coolant boiling or fuel failures) or system damage (see Section IV.B).

5. Local Faults

Loss of cladding integrity of a single fuel element during normal steady-state full power operation should not occur during the design lifetime of the fuel because of the margins included in the design of the fuel and cladding. However, stochastic fuel element failure must be anticipated, due to a random cladding defect which goes undetected during manufacture and inspection or due to random localized thermal, hydraulic or mechanical conditions within the fuel assembly.

Metallic fuel elements have a range of features that enhance their tolerance to local fuel failure events. These features include:

(1) Fuel alloy compatibility with sodium. No chemical reaction is produced between Na and metal fuel.

(2) High thermal conductivity of metal fuel. Low fuel centerline temperature, reduced hot-spot temperatures.

(3) Low fuel clad mechanical interactions. Minimal clad loading for transient events.

(4) Ease of fabrication allows attainment of high quality reprocessed fuel.

The superior performance potential of metallic fuel under run beyond cladding breach (RBCB) operating conditions was discussed in Section II.C.

6. Core Melt Accident and Mitigation Accidents

The probability of core meltdown is exceedingly remote; however, despite all possible design measures taken, a theoretical possibility of core meltdown (e.g., from complete and sudden loss of flow without scram or from complete, long-term loss of all decay heat removal systems) remains. Work to date has revealed three characteristics of particular importance to reduction of risk for these extreme scenarios: (1) the adiabatic Doppler feedback rate for metal fuel is equal or greater (more negative) than for oxide fuel, (2) in-pin metallic fuel axial extrusion upon melting gives rise to a significant reactivity reduction mechanism, as demonstrated in transient fuel tests in TREAT, (3) following overpower-induced fuel element failure, rapid metallic fuel dispersal has been demonstrated in TREAT tests (see Section IV.F for additional details), and (4) resolidified molten metal fuel debris beds have been shown to be highly porous and coolable (see Section IV.F for additional details).

B. IFR Inherent Safety Demonstration Tests in EBR-II

Twelve years of thermal-hydraulics testing at EBR-II culminated in April 1986, with the completion of the Inherent Safety Demonstration Test series.[1]

The results of this test series provided a prototypic demonstration of the inherent safety features of the IFR concept that result from the use of metallic fuel, liquid metal coolant, and a pool-type primary system. These features include: (1) passive removal of decay heat by natural circulation, (2) passive reactor shutdown in an unprotected (i.e. without scram) loss-of-flow accident, and (3) passive reactor shutdown in an unprotected loss-of-heat-sink accident.[2] Analyses have shown that these inherent safety performance characteristics can be achieved in commercial-sized IFRs.

1. Description of EBR-II Plant

The EBR-II plant consists of a primary system and a secondary system both using molten sodium as the coolant and a rather conventional steam system, as shown in Fig. IV.1. The primary system is located in a large double-walled tank. The tank contains about 340 m^3 of sodium at 370°C under normal operating conditions. The two primary pumps take their suction directly from the tank and deliver a combined flow to the reactor of 485 kg/s at a power of 62.5 MWt. The corresponding mixed-mean temperature of the sodium coolant leaving the reactor is 475°C.

There are 12 control rod positions, although only eight contain control rods (fuel-bearing) at present. The remaining four control rod positions are available for special in-core instrumented subassemblies. The fuel used during the IFR Inherent Safety Demonstration was uranium-5% fissium alloy, enriched to 66% in ^{235}U. Sodium is used as a thermal bond between the pin and its cladding. There are 91 wire-wrapped fuel elements in a regular fuel subassembly and 61 in a control or safety subassembly. The primary flow to the reactor splits into two streams, one entering the high-pressure plenum that feeds the first seven rows and the other entering the low-pressure plenum that feeds the remaining rows. About 84% of the flow goes into the high pressure plenum and the remaining 16% goes into the low pressure plenum.

The high and low pressure sodium streams mix in the reactor outlet plenum, go through the outlet pipe to the primary auxiliary pump (a DC electromagnetic device), and then to the intermediate heat exchanger (IHX) in which it transfers its heat to the secondary sodium. The primary sodium

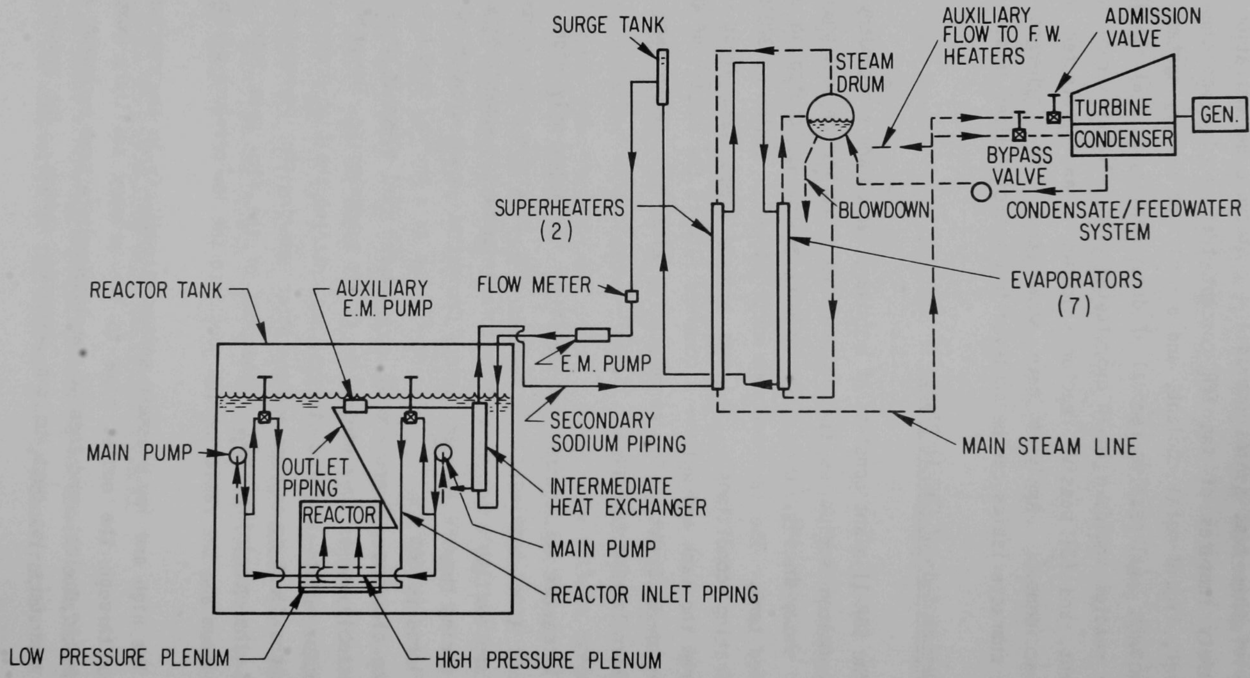

Fig. IV.1. Schematic of EBR-II Plant

leaving the IHX dumps directly back into the primary tank. Power to the auxiliary pump is provided by a rectifier backed up by a battery floating on the line. In case of a power failure, an emergency 480 volt diesel generator provides power to the rectifier. If the emergency power system fails, the battery takes over the load.

The secondary system sodium is driven by a single electromagnetic pump at a flowrate of 315 kg/s. The heat in the secondary system is transferred to the steam system in seven evaporators and two superheaters, all of the Argonne double-wall heat exchanger tube design. The steam is used in a conventional turbine-generator to produce electricity.

2. Results of Testing

The purpose of the EBR-II natural circulation tests was to demonstrate and provide measured data for the transition from forced to natural convection heat removal in a loss-of-flow transient with scram. Eighteen individual tests were run from varying initial power levels. All tests were initiated with loss of all pumping power with a normal reactor scram. Results from the most severe test, a loss-of-flow without scram from 100% power, show that:

(1) Peak coolant and fuel temperatures in the transition are low and do not challenge safety limits, and

(2) Test temperatures are reproducible and predictable, with good agreement between pretest predictions and test results.

The analysis of the tests and the test data indicate that there are a few critical features which govern the transition to natural convection and must therefore be carefully considered in design and in the modeling for analysis. These are: (1) heat generation (decay power), (2) flow coastdown rate (must accommodate short-term heat generation), (3) heat transfer and flow redistribution within the reactor, and (4) component elevation and pressure drops which fix the steady-state flow and steady state temperature field of the system.

In the EBR-II loss-of-flow without scram tests, the normal low-flow scram function was bypassed and the main coolant pumps were tripped to yield a full-scale simulation of an unprotected loss-of-flow accident. The plant was protected during testing by adding a fast acting, in-core temperature scram function designed to prevent fuel failure as a result of operator mistakes or equipment failure during testing. The fast acting in-core temperature scram function limit was not exceeded during the testing. In the loss-of-flow-without-scram accident, as the flow decays the core coolant outlet temperature rises, resulting in negative reactivity feedbacks that reduce the reactor power. In EBR-II, the strongest negative feedback component is supplied by the coolant density reactivity feedback in this scenario. Nineteen loss-of-flow-without-scram tests were run from varying initial power levels and coolant flows, with pump run-downs of varying speeds. All of the tests demonstrated passive reactor power reduction in response to the loss-of-coolant flow. The most severe test was from 100% power and flow, with pump stoppage just 95 sec from initiation of the coastdown. The key observations from these tests are as follows:

(1) Peak temperatures are within anticipated transient safety limits, with no reduction in fuel lifetime;

(2) Good agreement is obtained between measured and predicted results, indicating that the physical mechanisms responsible for the passive power reduction and natural circulation decay heat removal are identified, understood, and adequately modeled;

(3) The long-term core exit coolant temperature falls to near normal operating conditions following a short-term transient rise as reactor feedbacks act to match the power level to the natural circulation flow and the decay heat removal rate; and

(4) The transient peak coolant temperatures are determined by the relative size of the neutronic and thermal-hydraulic time constants that link the temperature changes to power reduction. The flow coastdown time constant is governed by the

pump and flow circuit design. Thus, peak temperatures can be limited by appropriate pump and/or power supply design.

The EBR-II loss-of-flow without scram tests demonstrate that the loss-of-flow class of accidents can be dealt with passively with proper utilization of the IFR design concepts.

In the EBR-II loss-of-heat-sink-without-scram tests, secondary circuit sodium flow was stopped, eliminating the normal heat rejection path from the primary system. The tests were thus a simulation of loss of feedwater accidents, failures in the steam system, or loss of secondary sodium flow coolant. As hot primary sodium returns to the core from the intermediate heat exchanger, negative reactivity feedback mechanisms act to reduce the reactor power, in an attempt to match the power level to the reduced heat rejection.

Stopping heat transfer to the balance of plant causes an increase of the primary system temperature. The rate of increase of temperature was gradual, even though the full reactor power was initially retained in the primary system. The rate of temperature rise was mitigated by the heat capacity of the large sodium pool and structural heat capacity in the cold pool. The increasing cold pool temperature caused thermal expansion of the tank and core support structure resulting in net negative reactivity and a reduction in the reactor power. The power reduction was sufficient to reduce reactor outlet temperature and prevent significant temperature overshoot. An increase of inlet temperature of 40°C was sufficient to compensate for the EBR-II power reactivity decrement and shutdown the reactor. These shutdown mechanisms have been found to be typical of larger IFR designs indicating passive safety margins for loss-of-heat-sink accidents.

C. Safety Analysis

In order to further demonstrate the safety performance potential of the IFR concept, reactor designs of various sizes have been analyzed. The designs considered were 470 MWt, 900 MWt, and 3500 MWt reactors in pool-type primary systems, cooled with sodium and fueled with U-Pu-Zr ternary fuel. The results for only the 900 MWt design are presented here, followed by discussions on the size dependence.

In these analyses, three anticipated transients without scram (ATWS), were analyzed with the SASSYS computer code. The three ATWS events analyzed were (1) unprotected loss-of-flow (LOF), (2) unprotected loss-of-heat-sink (LOHS), and (3) unprotected transient overpower (TOP).

For the unprotected loss-of-flow event, the assumed initiator is loss of power to the primary and intermediate coolant pumps without scram. As the flow decreases, the core outlet temperature rises. The heating and expansion of the core radially and axially cause negative reactivity feedbacks that reduce the reactor power. As the power falls, the coolant outlet temperature peaks and then also begins to decrease. Analysis shows that coolant boiling is avoided with substantial margin in the short-term transient. In the long term, system temperatures remain below levels at which load-stress-induced creep could result in structural failures.

For the loss-of-heat-sink event, it is assumed that feedwater supply to the steam generators is lost, yielding a gradual heating of the intermediate and primary coolant systems and an increase in the core inlet temperature. Heating of the core support grid spreads the core radially, introducing negative reactivity which reduces the reactor power. In the long term, the reactor power equilibrates to any available heat sink with the inlet temperature elevated above the initial state. Analyses show that the negative reactivity feedbacks reduce the reactor power as the core inlet temperature rises, with peak temperatures only slightly elevated above nominal conditions.

For the transient overpower event, the assumed initiator is a runout of a single, maximum-worth control rod. In the IFR metallic-fueled cores with low cycle burnup reactivity swing, this amounts to an insertion of about 10¢ of reactivity. In the resulting transient, the reactor power rises above nominal, followed by a very slight heating of the coolant which introduces sufficient negative reactivity to return the reactor power gradually to equilibrium with the assumed nominal heat rejection at the steam generators. Analyses show that the low excess reactivity made possible by the high breeding gain in the metallic core results in only slight over-temperature conditions.

Results of detailed analyses of LOF, LOHS, and TOP events are presented in the following sections, preceded by a brief summary of SASSYS computer code capabilities and validation results.

1. The SASSYS Computer Code

The SASSYS computer code provides the capabilities to perform a coupled thermal, hydraulic, and neutronic analysis of LMR designs, including the reactor core, the primary and intermediate coolant circuits, the reactor control system, and the balance-of-plant. All heat removal systems, including emergency decay heat removal devices, are modeled with mechanistic heat transfer and fluid flow models.

For the reactor core, SASSYS employs a multiple channel modeling in which a single average fuel element and its associated coolant are taken to be representative of a number of pins in a fuel assembly or a group of fuel assemblies. The single-element-per-channel modeling is also used to represent blanket and control assemblies, so that all the assemblies in the core are modeled. Any number of channels may be specified to represent the core, but usually from 3 to 30 such channels are sufficient.

For the primary and intermediate coolant circuits, SASSYS employs detailed models to represent plena, pumps, pipes, valves, heat exchangers, and other components. One-dimensional heat transfer and fluid flow models are coupled from component to component to provide a fully detailed description of any geometry specified.

SASSYS also contains a general and flexible digital simulation of plant control and protection systems. The plant control system simulation can be used in analyses to explore reactor and plant response to both transient design basis and accident initiators.

The SASSYS balance-of-plant (BOP) capability provides detailed mechanistic models of the steam generators, turbines, pumps, heaters, pipes, and valves in water/steam circuits. These models can be used to analyze transients in the BOP and their impact on the sodium circuits and the reactor core.

Validation of the models in SASSYS has been obtained through detailed analyses of both protected and unprotected tests performed in EBR-II and FFTF.[3,4] Coupled thermal, hydraulic, and neutronic analyses of these tests have produced excellent agreement with measured test data, and validation of the models in SASSYS.

2. Unprotected Loss-of-Flow Analysis for the 900 MWt Reactor

The initiator for the LOF event is loss of power to all pumps, including the steam generator feedwater pumps, the intermediate loop sodium pumps, and the primary coolant pumps. The coolant flow in the primary circuit is assumed to decay with a 6 sec flow halving time, until natural circulation conditions are achieved. It is also assumed that the plant safety system fails to operate, and thus the reactor initially remains at nominal power due to failure of the scram system.

Results from the analysis of this accident are presented in Fig. IV.2. Figure IV.2a shows the time history of reactor flow and power following accident initiation. As the flow decays, the reactor outlet temperature rises, introducing negative reactivity feedbacks that lower the reactor power as shown in Fig. IV.2a. The time dependence of these reactivity feedbacks is shown in Fig. IV.2b. The most significant feedback in this accident comes from radial expansion of the core as the core structure heats and expands due to the coolant temperature rise. Counter to this negative feedback is the positive feedback coming from the decrease in the coolant density as the sodium temperature rises. Other reactivity feedbacks are fuel Doppler reactivity due to the chilling of the fuel with the power decrease, fuel axial expansion as the weak fuel is pulled along with the heating and expanding cladding, and expansion of the control rods drivelines as heated core outlet

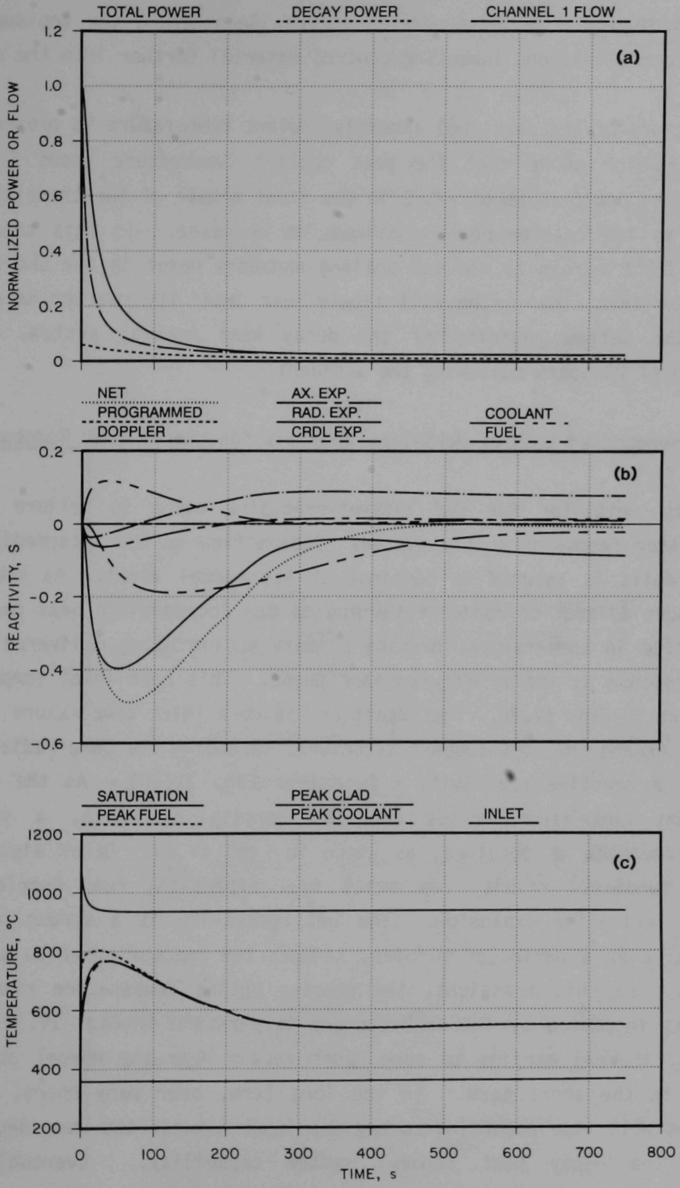

Fig. IV.2. Unprotected Loss-of-Flow: (a) Power and FLow, (b) Reactivity, and (c) Temperature History sodium rises through the above-core structure, lengthening the top-supported control rod drivelines and inserting control material farther into the core.

The history of the peak fuel assembly coolant temperature is presented in Fig. IV.2c, which shows that the peak coolant temperature rises from its normal value of 540°C to about 770°C in the first minute of the transient, and then falls as the reactor power continues to decrease. In this transient, there is a 160°C margin to coolant boiling and core upset in the short term. In the longer term, the system will slowly heat until the reactor decay heat falls to the design capacity of the decay heat removal system, in the neighborhood of 24 hours following the accident.

3. Unprotected Loss-of-Heat-Sink Analysis for the 900 MWt Reactor

The initiator for the loss-of-heat-sink event is failure of the steam generator feedwater supply system. Sodium flow in the intermediate and primary circuits is assumed to continue at its normal level. As the steam generator goes adiabatic, sodium returning to the intermediate heat exchanger begins to rise in temperature, heating primary sodium being delivered to the core inlet plenum by the primary coolant pumps. This core inlet temperature rise is shown in Fig. IV.3c. The impact of the core inlet temperature rise is to heat and expand the core support structure, spreading the core radially and introducing a negative reactivity effect (see Fig. IV.3b). As the overall core coolant temperature rises and its density decreases, a positive reactivity feedback is obtained, as shown in Fig. IV.3b. Other significant reactivity feedbacks result from axial fuel expansion, fuel Doppler, and control rod driveline expansion. The net reactivity is a strong negative effect that, over a period of minutes, reduces the reactor power as shown in Fig. IV.3a. In this transient, the reactor outlet temperature rises only slightly, as indicated by the peak coolant temperature in Fig. IV.3c. As a consequence, thermal margins to core upset remain near the normal operating conditions in the short term. In the long term, over many hours, systems temperatures will rise according to any imbalance between the core decay heat level and the decay heat removal system capability. Eventually, an equilibrium will be achieved between heat generation and rejection.

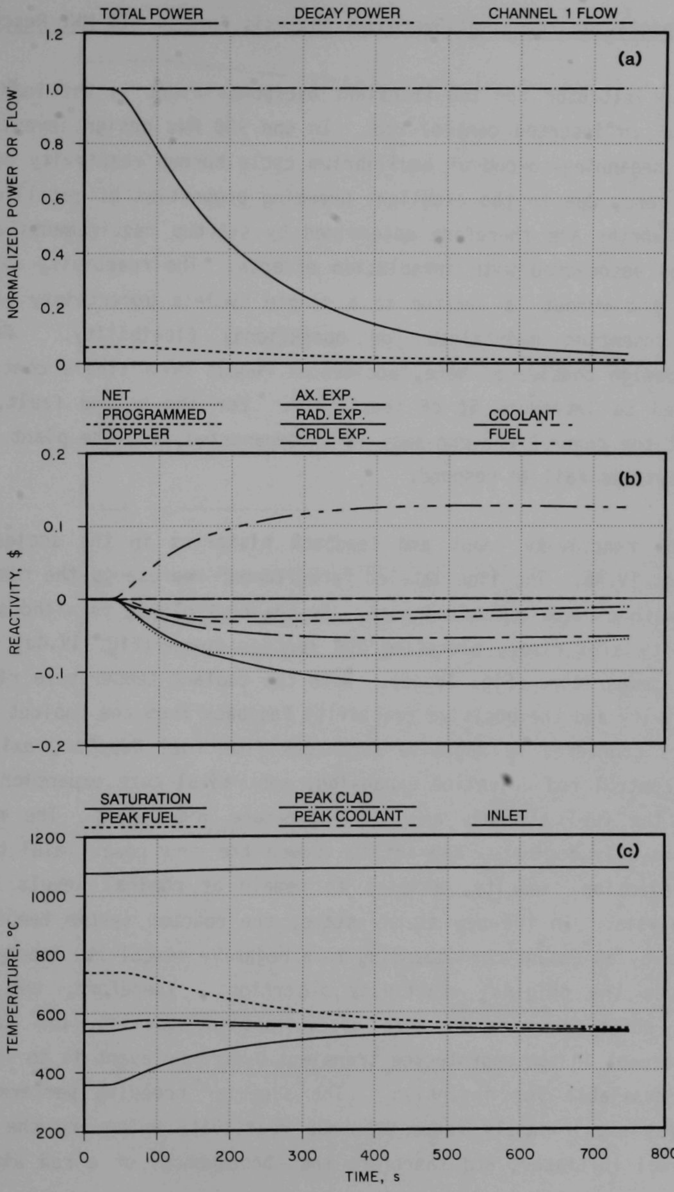

Fig. IV.3. Unprotected Loss-of-Heat-Sink: (a) Power and Flow, (b) Reactivity, and (c) Temperature History

4. Unprotected Transient Overpower Analysis for the 900 MWt Reactor

The initiator for the transient overpower event is the inadvertent withdrawal of an inserted control rod. In the 900 MWt design investigated, the nominal beginning-to-end of equilibrium cycle burnup reactivity swing is essentially zero, due to the excellent breeding properties of metallic fuel. Control rod worths are therefore determined by startup requirements and any uncertainties associated with irradiation effects. The reactivity available for control rod runout is limited to a single cycle's uncertainty plus any additional insertion maintained for operational flexibility. For the conceptual design considered here, accidental runout of a single control rod is calculated to introduce 6¢ of reactivity. For the second fault, it is assumed that the control rod run-away is uncompensated, and the plant control and safety systems fail to respond.

The reactivity input and feedback histories in the accident are shown in Fig. IV.4b. The line labeled "programmed" represents the reactivity associated with control rod withdrawal. As the control rod is withdrawn, the net reactivity also rises, elevating the reactor power (Fig. IV.4a) and the core outlet temperature (Fig. IV.4c). With the coolant temperature rise, the input reactivity and the positive reactivity feedback from the coolant density decrease are countered by negative feedbacks from fuel Doppler, axial fuel expansion, control rod driveline expansion, and radial core expansion due to heating of the fuel assembly and the above-core load pads. The negative effects eventually dominate, and act to reduce the core power level to match the heat rejection capacity, assumed to remain at nominal levels in this example analysis. In the new steady state, the reactor system temperatures are elevated by an amount corresponding to a negative reactivity feedback that just balances the original reactivity insertion. Therefore, the key to maintaining safety margins to core upset (coolant boiling, pin failures, structural creep) in the unprotected transient overpower event is to limit the reactivity available for insertion. The superior breeding performance of metallic fuel significantly reduces burnup reactivity swing and the control rod withdrawal initiator, and therefore the consequences of a rod withdrawal accident.

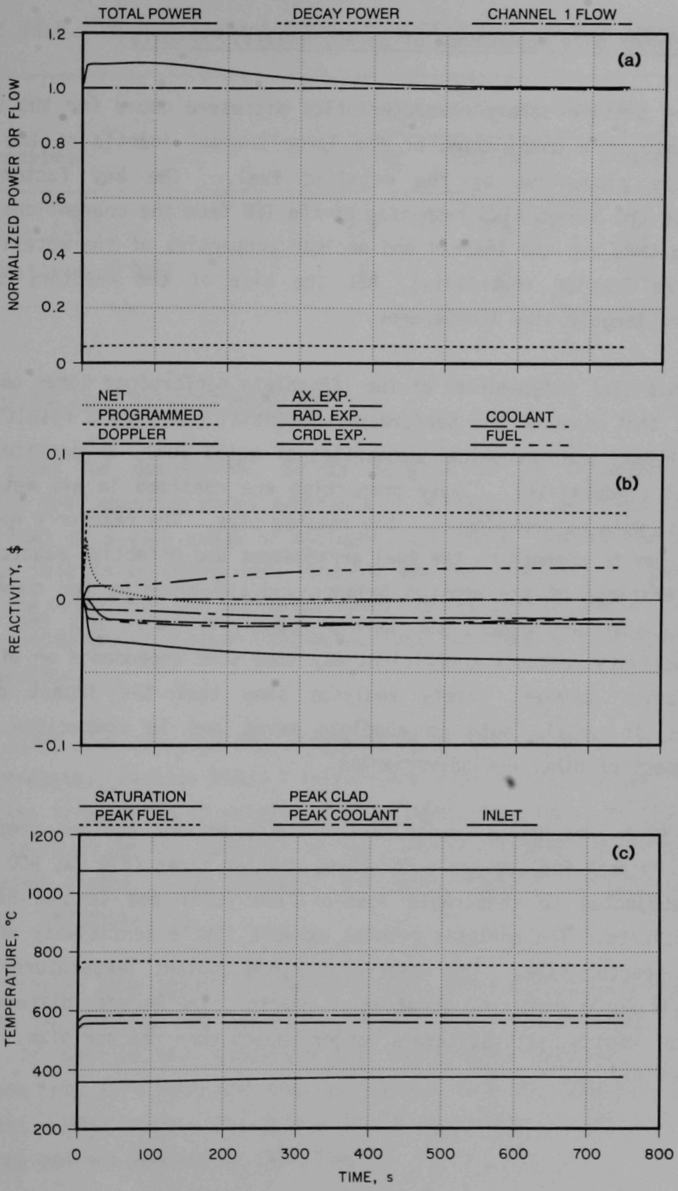

Fig. IV.4. Unprotected Transient Overpower: (a) Power and Flow, (b) Reactivity, and (c) Temperature History

5. Reactor Size Dependence of Safety Analysis Results

The passive safety characteristics discussed above for the 900 MWt design are due to a combination of the large thermal inertia of the sodium pool and the properties of the metallic fuel. The key factors that differentiate the benign ATWS responses of the IFR from the conventional mixed oxide fueled LMRs are the thermal and nuclear properties of the metallic fuel (small stored Doppler reactivity), not the size of the reactor, and the responses are largely size independent.

This size independence of the IFR safety performance comes about due to the fact that much of the performance potential comes as a result of the favorable thermal and mechanical properties of metal fuel, in particular the high thermal conductivity. These properties are realized in all metal fuel applications, with no dependence on the reactor size. The reactor's neutronic performance may be changed by the fuel arrangement and effective reactor size, through alterations of the neutron balance and the breeding (or conversion) performance. In particular, the burnup reactivity swing and the coolant density reactivity feedback coefficient may show some dependence on effective reactor size. However, safety analyses show that the impact of such dependencies is small, both in absolute terms and in comparison to the relative impact of other design variables.

Table IV.1 presents a comparison of the transient coolant temperature rise in the hottest fuel assembly for three reactor sizes (470 MW, 900 MW, and 3500 MW) subjected to comparable loss-of-flow (LOF) and loss-of-heat-sink (LOHS) transients. The analysis results exhibit little sensitivity of safety margins to reactor size. The observed maximum coolant temperature rise in Table IV.1 is not a monotonic function of reactor size because differences in other reactor design features have a larger impact than reactor size.

TABLE IV.1. Maximum Coolant Temperature Rise (°C) in ATWS Transients

Transient	Reactor Thermal Rating		
	470 MWt	900 MWt	3500 MWt
Loss-of-Flow (LOF)	234	229	253
Loss-of-Heat-Sink (LOHS)	69	19	21

D. Transient Fuel Behavior Modeling

In order to demonstrate safety margins it is necessary to have mechanistic fuel modeling codes available to analyze the detailed response of metallic fuel to a wide range of accident initiators. Two of the codes that play a key role in assessing this response are the STARS fission gas behavior code and the FPIN2 fuel pin mechanics code. The current status of these codes and their relationship to the LIFE-METAL fuel performance code are described in this section.

The STARS code analyzes the accumulation of fission products (especially gaseous products), fission product release and fission product swelling during steady-state irradiation of metallic fuel alloys. Physically realistic models are used to describe the behavior of the fission products in various trapped and released stages. The analysis has been recently extended to include multi-axial segments.

The initial development of the STARS code concentrated on the intragranular model for fission gas behavior. Models were also included to evaluate the role of gas in grain-boundary and grain-edge porosity. One of the conclusions from this work was that the bulk of the gas retained in the fuel was present either within the grains or in large pores. The role of these large pores was not modeled at that time.

The next stage of development was to extend the analysis to model the interaction between fission gas and the fuel over the entire fuel pin, rather than for a local element of the fuel. This extension necessitated modeling of the large pores, non-gaseous fission products, and the dimensions of the fuel pin. The analysis employed an average set of conditions--such as power and temperature--for the whole pin. Such a calculation was satisfactory for analysis of gas retention in the short fuel pin segments used in out-of-pile tests. Relatively good agreement was also obtained in some comparisons even for intact pins; for example, calculated plenum pressures agreed well with results from U-Fs fuel pins.[5] The results of this effort enabled the code to predict, with respectable accuracy, the dependence of gap closure and plenum pressure on burnup, temperature, power, and fuel composition.

Fission-gas behavior is strongly dependent on the temperature and power. Since both of these parameters vary strongly with axial location, it became clear that a more accurate analysis was needed. The STARS code was modified accordingly to treat an arbitrary number of equal axial segments. The axial temperature and power profiles are characterized by input values for each axial segment.

Simple models were also developed to account for sodium retained in large pores, and liquid fission products dissolved in the sodium. The result of these modifications is the current version of the STARS code. Results of code validation calculations with this version have been compared to measured results for U-Pu-Zr metallic fuels.[6] The comparisons include gas retained in the fuel, in the porosity, and released to the plenum; and axial elongation of the fuel and the effect of the variation in gap closure with axial location. The agreement between measured and calculated results is generally very good.

The FPIN2 computer code has been developed to analyze the complex thermal-mechanical phenomena which govern fuel and cladding behavior during fast-reactor accident transients. The analysis provides the fuel and cladding temperatures, stresses, and displacements during overpower and undercooling events. The basic program includes a group of subroutines to calculate the temperature of the fuel, cladding, coolant, and outer wall, and a separate group of subroutines to calculate the mechanical behavior of the fuel and cladding. Relevant pretransient fuel characterization parameters are input into FPIN2 based on sibling pin information or STARS and/or LIFE-METAL code calculations. The heat transfer section in FPIN2 uses an implicit finite difference algorithm, and the mechanical analysis makes use of a nonlinear finite-element procedure. A major reason for choosing the finite-element method is that it allows convenient modular coding of the fuel pin mechanics such that different models for material behavior and improvements in specific algorithms can easily be implemented into the code.

A comprehensive description of the FPIN2 code and the models used in the code to analyze the behavior of metallic fuel pins has been given previously.[7] There have been several modifications to the code since the time that paper was issued. These changes reflect new information on material properties and a better understanding of the phenomenology that govern the transient response of metal-fueled pins. The following paragraph describes several aspects of the most recent metal-fuel version of FPIN2.

Post-irradiation destructive examinations of ternary U-Pu-Zr fuel pins irradiated in EBR-II have revealed significant migration of zirconium. All previous versions of FPIN2 have assumed uniform fuel composition; changes have now been made to allow for fuel composition variations. The most significant changes were brought about by the realization that, because of alloy redistribution, the initial melting of ternary fuel may not occur at the fuel centerline and, for full length pins, the molten fuel zone may not have direct access to the plenum when melting begins.

Specific models added to FPIN2 include a provision for the user to supply radial and axial variations in plutonium and zirconium weight fractions (with the remainder assumed to be uranium). These distributions are used in the fuel material properties routines to determine the variations with alloy content in properties such as the fuel solidus and liquidus temperatures. Other modifications to the code include (1) a more detailed transient fuel swelling model that accounts for intragranular gas, grain boundary gas and pore gas, (2) changes in the cladding finite element analysis that allow elements to relax to a hydrostatic state of stress when eutectic melting occurs and (3) models for sodium bond dynamics.

The new version of FPIN2 has been used to analyze TREAT overpower tests M5, M6, and M7.[6] Results of code calculations were compared with experimental data on fission gas retention, plenum pressure, flowtube temperatures, melt fractions, cladding failure time and location, cladding plastic strain, eutectic penetration, fuel axial expansion and liquid fuel extrusion. Agreement between the calculations and measurements, within the experimental uncertainties, is excellent. The calculations show that failure of U-Pu-Zr fuel pins, at about four times nominal power, is dominated by plenum pressure loading with little FCMI. The high burnup pins failed from the fission gas pressure alone and eutectic wall thinning contributed significantly to the failure of low burnup pins in the TREAT tests analyzed.

The LIFE-METAL code is also being developed as part of the overall IFR Program. The LIFE-METAL code is used for the analysis of metallic fuel pins under normal and off-normal operating conditions, while FPIN2 is used to analyze accident conditions. There is some overlap in capabilities for handling off-normal conditions. However, in the development and validation of the codes the emphasis is very different: LIFE-METAL has focused on steady-state fuel behavior, while for FPIN2 the focus has been on transient fuel behavior. The codes use different numerical analysis methods, but the two codes use a common set of material properties. LIFE-METAL incorporates detailed models for predicting steady-state fuel behavior, but does not include detailed high-temperature fuel behavior models for transient behavior (e.g., fuel melting, fuel-cladding eutectic reactions, etc.). FPIN2 incorporates these models plus many more related to accident analysis and asks the user to provide input data describing the pretransient/steady-state conditions. This input can be obtained from LIFE-METAL calculations or data (e.g., fuel geometry, fuel microstructure, fission gas remaining in the fuel) from sibling pins. For design calculations, LIFE-METAL output is the preferred method of determining FPIN2 initial conditions, as LIFE-METAL has been validated to groups of fuel pins, each group having a common fuel composition and operating history. For detailed single-pin analysis of transient tests (e.g., TREAT), the preferred option is to use data from sibling pin(s) to provide the initial conditions.

E. Transient Fuel Testing

Laboratory experiments and in-pile tests provide the phenomenological basis for gaining an understanding of the metallic fuel safety performance. The knowledge obtained from such experiments and tests forms the basis for theoretical models used in analyses. The data generated in the experiments and tests provides direct validation of the theoretical models. Laboratory experiments and in-pile tests therefore play a central role in the IFR safety assessment.

Four facilities are available at ANL to provide the capability to span the range of testing needs necessary for: (1) anticipated and unlikely scrammed transients, (2) inherent response transients, (3) elevated temperature, long term, decay heating transients, and (4) severe fuel damage transients.

The four facilities are:

1. the Experimental Breeder Reactor II,
2. the Fuel Behavior Test Apparatus (see Section II.D),
3. the Whole Pin Furnace Test Apparatus, and
4. the Transient Reactor Test Facility, TREAT.

The relative capabilities of these facilities are shown in Table IV.2. The following sections describe the transient fuel testing results from testing in TREAT and the Whole Pin Furnace Test Apparatus.

1. Transient Fuel Testing in TREAT--the M-Series Tests

A principal activity in transient fuel testing has been a series of experiments performed at the Transient Reactor Test Facility (TREAT). The aim of these experiments, designated tests M2-M7, was the study of cladding failure threshold and other safety-related fuel behavior during simulated transient overpower (TOP) accidents.

TABLE IV.2. Fuel Test Facility Comparison

	In-Pile		In-Cell	
Facilities	TREAT	EBR-II	WPF[a]	FBTA[b]
Test Articles				
Cladding Types	X	X	X	X
Irradiated Fuel	X	X	X	X
Whole Pins	X	X	X	
Multiple Pins	X	X		
Complex Assemblies	X	X		
Sodium Cooling	X	X		
Full-Length Pins	X			
Issues				
Onset of Melting		X	X	X
Low Temp. Damage		X	X	X
High Temp. Damage	X			
Damage Additivity	X	X	X	X
Faulted Assembly	X	X		
Fission Product Source Term	X	X		
Fuel Dispersal	X			

[a] Whole Pin Furnace Test Apparatus.
[b] Fuel Behavior Test Apparatus.

Specifically, the data needs addressed by the TREAT tests were:

(1) Determination of margin to failure and identification of underlying mechanisms,

(2) Assessment of pre-failure axial expansion as a potentially significant pre-failure reactivity removal mechanism, and

(3) Preliminary assessment of post-failure events: behavior of disrupted fuel and coolant.

Overpower testing in the TREAT reactor draws upon more than 20 years of experience of transient safety testing in flowing sodium loops and allows for controlled transient overheating of whole fuel pins by fission in a near prototypic thermal and hydraulic environment. A two dimensional history of test fuel motion is made possible using the fast neutron hodoscope.[8] The TREAT hodoscope, located at the end of a radial slot in the TREAT core, is a diagnostic system that collimates and detects fast neutrons produced by fissions in the test fuel. In support, the Hot Fuel Examination Facility at ANL-West provides in-cell facilities to assemble and disassemble experiments on irradiated fuel. Non-destructive radiography and profilometry of test fuel is also performed both pre- and post-test at Hot Fuel Examination Facility. Post-test destructive examination of M-series TREAT tests, including both failed and unfailed pins, is undertaken at the Alpha Gamma Hot Cell Facility at ANL-East.

2. M-Series Test Hardware

The sodium loop used in TREAT for Argonne's LMR safety experiments in recent years has been the Mark-III loop.[9] Figure IV.5 shows the Mark-III loop as configured for M-series tests. In essence it is a highly instrumented elongated loop of thick-walled stainless steel pipe through which liquid sodium is circulated by means of an electromagnetic pump. Two parallel legs of the loop are 3.5 m long with center-to-center separation of about 0.1 m. The entire system is housed in a long rectangular container of cross section dimensions 10 cm by 20 cm, and is designed to occupy the center of the reactor with the test fuel directly in line with the hodoscope slot. The Mark-III loop is useful for testing a wide variety of test fuel pin types and pin bundles. A removable instrumented "test train" in one leg of the loop contains the test fuel in a configuration pertinent to addressing specific requirements of the test program.

In the M-series test train, each pin is located in a separate stainless-steel flowtube. The division of total loop sodium flow among the flowtubes in each test is chosen to achieve the particular objectives for each pin. The flow division is effected by properly sized orifices installed near the entrance to each flowtube. Lateral separation of test pins is as large as

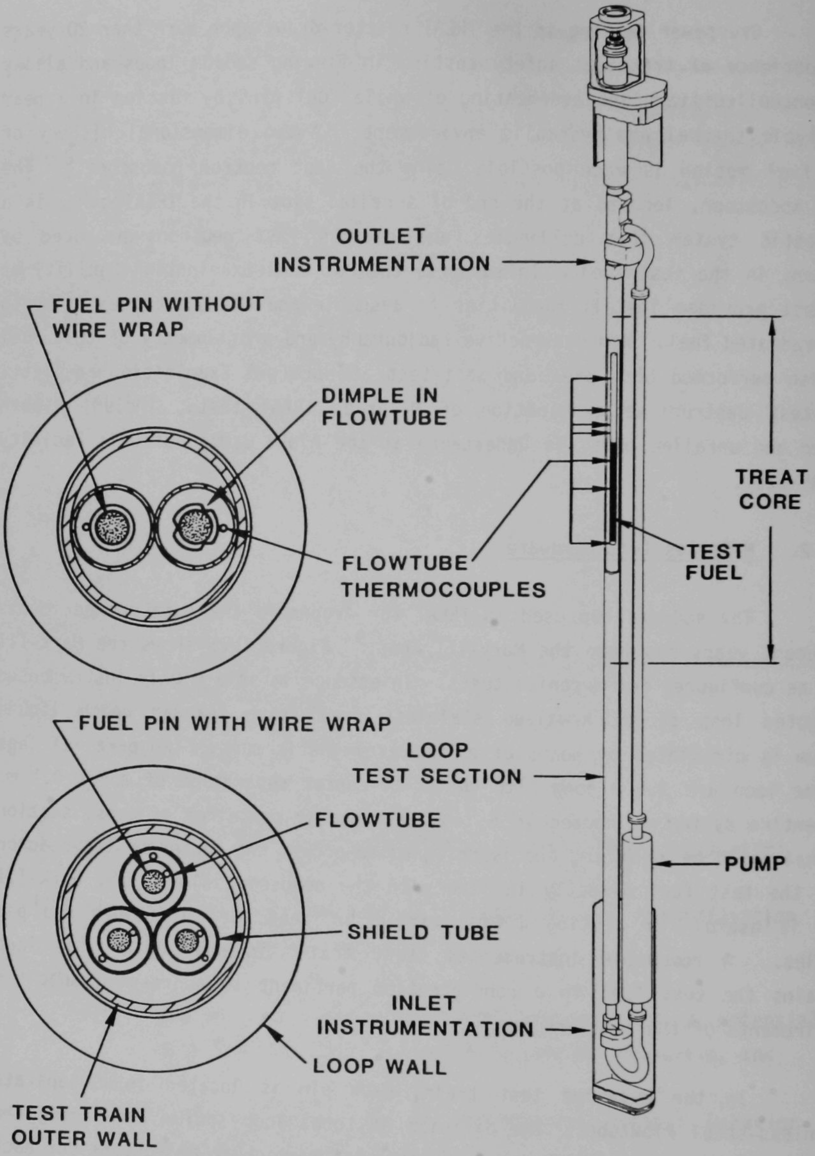

Fig. IV.5. Mark-III TREAT Loop Showing Test Hardware and Fuel Pin Test Configuration possible to minimize the neutron shielding of one pin by another and to enhance the ability of the hodoscope to resolve test pins as individual entities. The number of pins per test is determined principally by the bore diameter of the loop and the diameter of the test pin, as illustrated in Fig. IV.5.

3. M-Series Test Design

The designs of all M-series TREAT tests have a number of general features in common. Low power, non-destructive operation verifies equipment performance as well as the neutronic coupling of the test fuel to the TREAT reactor. The subsequent overpower transient is designed to generate thermal conditions in test fuel that mimic fuel overheated under fast reactor accident conditions. Finally, the overpower transient is terminated quickly enough to preserve conditions which existed at the peak of the overpower.

Heat balance transients, run at constant power and flowrate, are performed before each overpower transient to provide an integrated check of the thermal-hydraulic operation of the entire experiment system including the reactor, test fuel and sodium loop. A key measurement made during the heat balance is the coolant temperature rise from inlet to outlet under true steady-state conditions. This temperature rise provides a direct, in situ measurement of the coupling of each test pin's power to measured reactor power and measured coolant flow rate.

In performing the final overpower transients, all M-series test fuel is subjected to similar overpower conditions: full coolant flow rate and an exponential power rise on an 8-sec period. The 8-sec period was chosen as the slowest transient possible that would commence from near-nominal power and carry through to cladding failure within the energy deposition limitations of the TREAT reactor. (The TREAT reactor core heats up nearly adiabatically, and its energy deposition in the test fuel is limited to the equivalent of several tens of seconds of nominal power.) A "high" system pressure, $\gtrsim 4$ atm, prevents coolant boiling prior to cladding failure. Baseline thermal conditions in the test fuel are referenced to conditions assumed nominal in a fast reactor. These include a peak linear power rating of 40 kW/m, an inlet temperature of

360°C and a 150°C coolant temperature rise. The power transient is rapidly terminated upon detection of cladding breach (through sudden measurable changes in coolant flow) or, by using previously measured failure thresholds, just prior to failure.

Thermal hydraulic analyses referred to here used the COBRA-PI code.[10] Historically, COBRA-PI has been used extensively in analysis of TREAT in-pile experiments because of its ability to explicitly model pin bundle geometry in small-scale experiments. In this context its use has been limited, however, to intact (fixed) geometry and single-phase coolant flow. For M-series tests, the analysis incorporates a detailed description of the fuel pin, the flowing coolant and flowtube.

Reported fuel performance calculations of pre-failure axial expansion and cladding failure are performed by a specially written routine, the EXP ("Extrusion and Penetration") model that is auxiliary to the COBRA-PI code. Development and application of the EXP routine were based on modeling concepts to be described below. Logical flow of the analysis is such that transient temperatures calculated by COBRA-PI provide driving input for EXP, but EXP calculations do not influence COBRA-PI. The combined program for metal fuel performance analysis is termed "COBRA/EXP".

4. Test Fuel

The M-series tests extended existing fuel performance studies into unprotected transient overpower TOP conditions. It is important to test as many fuel and cladding combinations relevant to the IFR concept, with as wide a range of fuel burnups as possible, in order to distinguish features of safety-related fuel performance which are fuel-specific from those which are common to all modern metal-fuel types. Initial tests (M2-M4) in the series used EBR-II Mark-II driver fuel made of a binary alloy of uranium and "fissium" (U-Fs) because irradiated fuel of that type was available early and because it had been well-characterized. Later tests (M5-M7) used IFR-type fuel which had been irradiated in EBR-II, as appropriate test pins became available. Table IV.3 summarizes M-series tests of metal fuel pins to date.

TABLE IV.3. Overpower Testing of Metal Fuel in TREAT M-Series

Test	Fuel (comp. wt.%)	Cladding	Burnup (at.%)	Test Date
M2	U-5Fs	316 SS	0.3	3/85
	U-5Fs	316 SS	4.4	
	U-5Fs	316 SS	7.9	
M3	U-5Fs	316 SS	0.3	4/85
	U-5Fs	316 SS	4.4	
	U-5Fs	316 SS	7.9	
M4	U-5Fs	316 SS	0.0	1/86
	U-5Fs	316 SS	2.4	
	U-5Fs	316 SS	7.9	
M5	U-19Pu-10Zr	D9	0.8	8/86
	U-19Pu-10Zr	D9	1.9	
M6	U-19Pu-10Zr	D9	1.9	2/87
	U-19Pu-10Zr	D9	5.3	
M7	U-19Pu-10Zr	D9	9.8	10/87
	U-10Zr	HT9	2.9	

5. Overpower Test Performance

"Transient hodographs," an example of which is shown in Fig. IV.6 for the M7 test, describe the fuel motion as measured by the fast neutron hodoscope. Measured fuel density, averaged over the indicated time intervals, is displayed on the two-dimensional grid. (The scale is greatly expanded horizontally.) Note that the resolution is sufficient to easily distinguish the fuel columns of both M7 test pins. In Fig. IV.6, prefailure axial expansion is seen in both test pins as an increase of fuel density near the top and above the fuel column in hodographs a-d. The eventual failure of the ternary pin is seen dramatically in hodographs d-g by sudden fuel gains extending to great distances above the original fuel column (with corresponding losses from the remainder of the pin). Timing of this event is in good agreement with other test instrumentation.

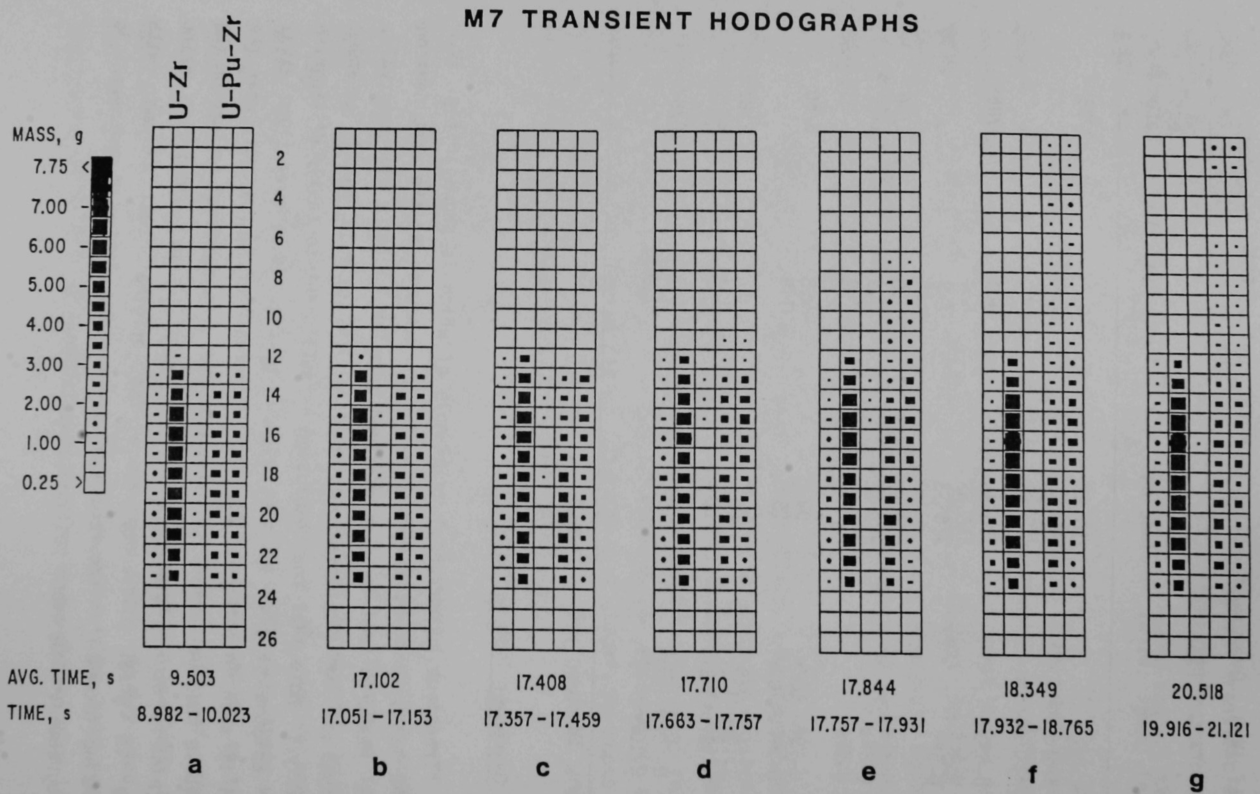

Fig. IV.6. Describing Fuel Motion in Test M7 as Measured by the Fast Neutron Hodoscope

All M-series overpower transients caused extensive melting in the test fuel, amounting to about one-half the fuel inventory at peak power. The same thermal analyses that computed flowtube and coolant temperatures also computed fuel melting and temperature fields deep within the fuel pin. These internal temperatures were not accessible to direct measurement. However, experimental estimates of the maximum extent of melting were made during post-test micro-examination of cross sections from test pins that did not fail. Agreement between these measurements and the calculations was generally good.

A comprehensive summary of key overpower test results is given in Table IV.4. Reported overpower levels signify peak thermal conditions (temperatures, amount of melting, pressure, etc.) appropriate to a fast reactor and carry an uncertainty of 3-5%. Table IV.4 also includes measured peak values of pre-failure fuel expansion and a comparison of cladding failure results with pre-test predictions. Calculated values of peak pin pressure are also indicated.

6. Pre-Failure Fuel Expansion

In every case some axial expansion of the test fuel was observed before fuel cladding failure with peak values shown in Table IV.4. Maximum pre-failure expansion of the U-Fs test fuel shows large expansions (16-18%) at low burnup which decrease rapidly with increasing burnup. By contrast, pre-failure axial expansion of IFR-type fuel tested showed much weaker burnup dependence with large values at low burnup conspicuously absent.

In irradiated fuel, the mechanism underlying measured axial expansion is believed to be fission gas that is initially confined within solid fuel but freed to expand when fuel melts. Post-test examination of test pins which remained intact all show large bubbles which are not typical of normal as-irradiated fuel but are indicative of extensive fuel melting, bubble coalescence and expansion at much higher temperatures. Postulating expanding fission gas as the driving mechanism, elements needed to quantify the particular amount of axial expansion are: (1) the amount of molten fuel, (2) the concentration of gas made available to expand when fuel melts, (3) initial

TABLE IV.4. Peak Overpower Conditions and Fuel Performance Summary

Fuel/ Cladding	Axial Peak Burnup (at. %)	Peak Overpower (normalized)[c]	Calc. Failure Threshold	Peak Pressure (MPa)	Max. Axial Expansion (%)
U-19Pu-10Zr/ D9 Steel	0.8[b]	(3.4) 4.3	(4.6) 5.1	(1) 1	(1) 1
	1.9[b]	(3.4) 4.3	(4.6) 5.1	(3) 3	(0.5) 2
	1.9	4.4	4.6	3	2-3
	5.3	4.4[a]	4.5	10	3
	9.8	4.0[a]	4.4	19	3
U-10Zr/ HT9 Steel	2.9	4.8	4.4	6	2-4
U-5Fs/ 316 SS	fresh	3.8	4.3	0.6	4[d]
	0.3	4.1	4.7	0.6-0.8	16
	0.3	4.1	4.8	0.6-0.8	18
	2.4	4.1[a]	4.4	2-6	7
	4.4	4.2[a]	4.5	7-9	(e)
	4.4	4.0	4.4	7-9	4
	4.4	3.8	4.3	7-9	4
	7.9	4.1[a]	3.6-4.0	17-20	3
	7.9	3.4	3.6-4.0	17-23	4

[a] Indicates cladding failure occurred.

[b] Indicates M5 test pins; values in parentheses "( )" are from the first overpower transient.

[c] Relative to nominal conditions in a fast reactor: peak linear power of 40 kW/m, 360°C inlet, and 150°C coolant temperature rise.

[d] Expansion may have been caused by localized sodium bond boiling

[e] Data ambiguous.

size of gas bubbles and initial surface tension effects, and (4) the magnitude of the pin plenum pressure resisting expansion. Basically, axial expansion occurs when fission gas present in molten fuel expands until its pressure equals that of the pin plenum. The onset of fuel expansion coincides with significant fuel melting.

The same basic modeling implemented in COBRA/EXP was used to calculate axial expansions in all M-series tests but with significantly different concentrations of available fission gas assumed for U-Fs vs IFR fuel types. Measured expansions in U-Fs fuel were well predicted in timing, overall magnitude, axial distribution, and burnup dependence with the assumption of a maximum fission gas concentration in small bubbles of 5 μ-moles/g-fuel (or total gas generated in about 0.5 at.% of burnup). This assumed peak concentration, equal to about one-fourth of the peak whole-pin average amount, corresponded closely to measured gas concentrations at hottest axial locations.

By contrast, IFR fuel test data require rather different assumptions about fission gas availability. Using the same concentration of fission gas in the analysis of U-Fs fuel leads to predictions of expansion magnitudes which are too large and a burnup dependence that is too strong (similar to U-Fs fuel). It is noted, however, that the IFR fuel had smaller grain size and was irradiated at significantly higher linear power and temperature than the U-Fs fuel. Thus, the high temperature regions of IFR fuel which contribute most to axial expansion might contain little, if any, dissolved gas.[6] In view of this, measured expansions in IFR fuel were reproduced assuming a model where only gas trapped in large bubbles within the fuel porosity was available for expansion.

The behavior of the single fresh U-Fs pin tested provided interesting counterpoint to the above discussion of irradiated fuel. Without benefit of any dissolved fission gas there was evidence of ~4% local expansion near the top of the fuel at peak power, which collapsed rapidly upon power shutdown. Post-test examination showed evidence of large bubbles in the top region of the fuel. Local boiling of bond sodium entrained within molten fuel is a possible driving mechanism for this observed expansion.

7. Cladding Failure

Post-test examination has provided evidence for two principal mechanisms for cladding damage in metal fuel: overpressure and clad thinning. Because of the low mechanical strength of metal fuel, pin plenum pressure provides the primary source of pressure loading and stress on the cladding. Cladding stresses, however, reflect not only the pin plenum pressure but also thinning by formation of low-melting iron-uranium alloy compositions. Integrating these two damage mechanisms within a single analytical model to compute pin failure in metal fuel has been described in Ref. 11 under the assumption that both mechanisms act "independently".

Calculated times of cladding failure as performed in the COBRA/EXP module are reported in Table IV.3, expressed in terms of overpower level on the actual ~8-sec period power transient (the calculations being extended, if necessary, beyond the time of experiment termination). In conjunction with cladding failure observations, thermal calculations indicate that at overpower levels of about four times nominal the temperature of the fuel cladding interface exceeds a "threshold" value of 1075°C, where eutectic penetration into the cladding becomes very rapid (associated with the melting of a protective solid iron-uranium composition).

Post-test examination suggests that the survival of the U-Zr pin to 4.8 times nominal overpower was due to less-than-expected penetration of the cladding by eutectic. This reduced penetration might have been caused by the binary fuel's high solidus temperature of 1225°C. By contrast, in all other metal fuel tested thus far, lower solidus values insured an entire fuel cross section molten and in contact with the cladding when the threshold for rapid melt penetration (~1075 °C) was reached at the fuel-cladding interface.

General studies with the present cladding failure model indicate that, for the fuel burnups and heating rates employed in M-series tests, pins tend to fail at or near the threshold point of rapid eutectic penetration. Different modeling issues and questions arise concerning lower cladding damage rates at lower temperatures. Extending model validation into these areas will require testing higher burnup fuel and/or overheating test fuel to lower temperatures for longer times.

It is worthy of note that metal fuel subjected to an 8-sec period transient overpower event fails at approximately four times nominal power. Figure IV.7 shows an experimental comparison of the performance of both metal

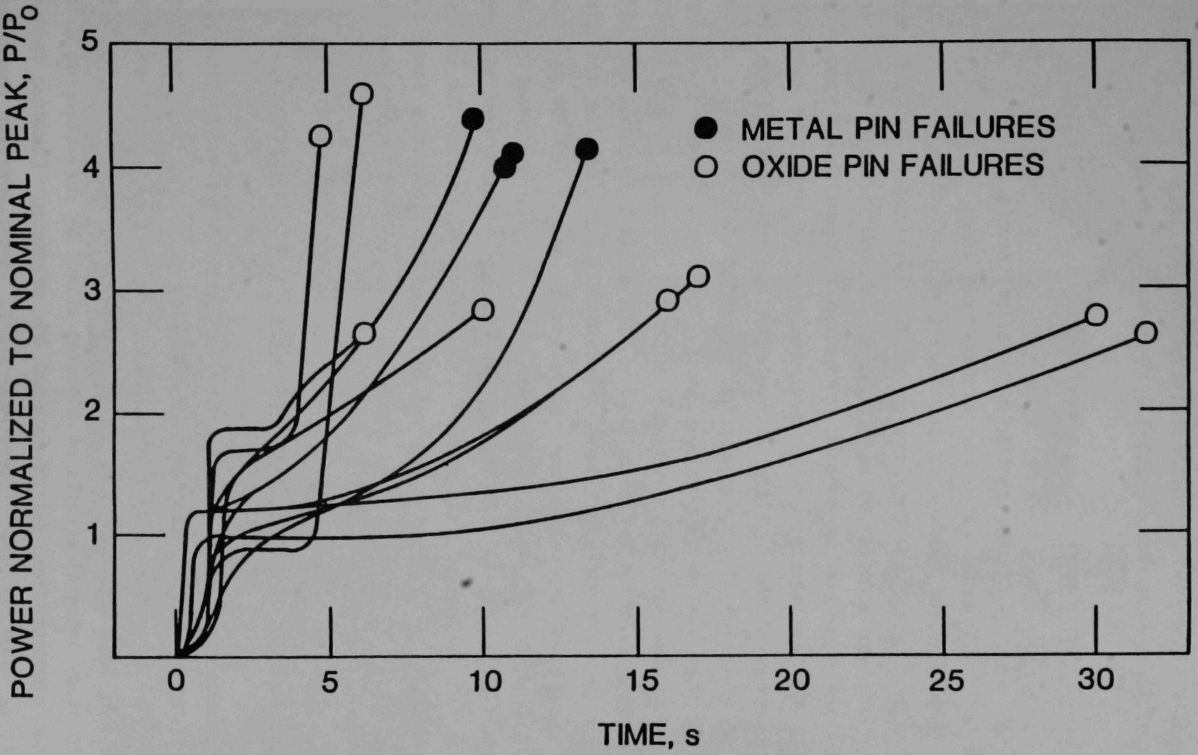

Fig. IV.7. Summary of Metal and Oxide Transient Overpower Experiments in TREAT and oxide fuel in austenitic stainless steel cladding subjected to transient overpower events in the TREAT reactor. Except for very fast transients, the oxide fuel failed at approximately 2.5-3.5 times nominal power.

8. Post-Failure Events

When cladding failed, similar post-failure events characterized the behavior of all fuel types tested. In each case about half of the fuel inventory, corresponding roughly to the fuel's melt fraction, was ejected rapidly through a small cladding breach at the fuel top. In all cases cladding failure was accompanied by a sudden, temporary reversal of inlet coolant flow and rapid coolant voiding. Measured pressure spikes were minor (less than 2 MPa) and were generally about one order of magnitude less than the plenum pressure of the failed pin. Fuel ejection from a failed pin could be driven by expansion of trapped fission gas and/or sudden boiling of the liquid sodium bond within the fuel. Ejected fuel then dispersed rapidly, combining with cladding and structural materials into a highly mobile low-melting point form and traveling upward with coolant to locations well downstream of the original fuel zone. Hodoscope data indicates the time period of significant disruption and removal to be around 100-200 ms. This timing of disruption is also in agreement with measured perturbations of pressure and flow. The post-failure coolant flow was about 2/3 of its pre-failure flow rate indicating only partial flow blockage. Because the coolant channel environment in the tests was not optimized to simulate a large pin bundle, only qualitative conclusions should be drawn concerning dispersal of materials from failed pins.

9. Transient Fuel Testing in the Whole Pin Furnace Test Apparatus

To meet technical fuel testing needs beyond the capabilities of TREAT tests, a new radiant-furnace test facility in a hot cell has been prepared for testing whole, EBR-II-irradiated pins. The apparatus is called the Whole Pin Furnace test apparatus and is shown in Fig. IV.8. Tests will be performed to study integral effects of cladding attack by fuel-cladding alloy formation and cladding creep due to internal pin pressure. Cladding failure margins will be measured under lower-temperature, longer-duration conditions

Fig. IV.8. Whole-pin Furnace Test Apparatus (ANL Neg. No. 7773) than achievable in TREAT. Pins of a variety of fuel/cladding compositions and burnups will be tested. An appropriate axial temperature gradient in the test fuel will be generated. Fission gas released from the pin upon failure will be collected and measured posttest. Operational checkout of the apparatus has been completed.

F. Severe Accident Mitigation

A preliminary series of molten fuel quench tests has been carried out in order to study the breakup and interaction behavior of kilogram quantities of uranium alloys in sodium.[12-14] Figure IV.9 shows the test apparatus. These tests provided data on fragmentation, heat transfer, solidification, and impingement heat flux necessary for reactor safety analysis. The uranium metals (3 kg) were melted inductively with a 30-kW 10,000-Hz TOCCO Motor generator. A ZrO_2 plug was removed pneumatically from a MgO crucible to initiate the downward pour of the melt into 600°C sodium in a 192-mm ID container. The parameters which were varied in the tests were: (i) melt superheat (10 to 800°C), (ii) injection velocity (2 and 10 m/s), (iii) injectant diameter (12.5 and 25 mm), (iv) sodium depth (0.15 to 1.2 m), and (v) injectant material (U, U-5 wt% Zr, U-10 wt% Zr, U-10 wt% Fe). The melt superheat is based on the liquidus temperature of the U-5 wt% Zr (1246°C) and the U-10 wt% Zr (1360°C), the U melting point (1133°C), and the melting point of the U-10 wt% Fe eutectic.

For sodium depths as low as 0.3 m the uranium pour stream broke up and the fragments solidified before reaching the bottom of the interaction vessel. The particles were typically about 10 mm in size and settled to form a bed with about 90% voidage. Thermal equilibrium determined from an enthalpy balance between the sodium and the pour stream material generally occurred in 2 to 3 sec reflective of the high thermal conductivity of these materials. The initial (4 sec) temperature response of a 25-mm steel baseplate of the sodium container behaved as a semi-infinite medium contacted by a porous uranium metal medium with 90% voidage.

It is evident from calculations based on typical bed conditions observed in these tests that the debris from a meltdown of a metal-fuel pool

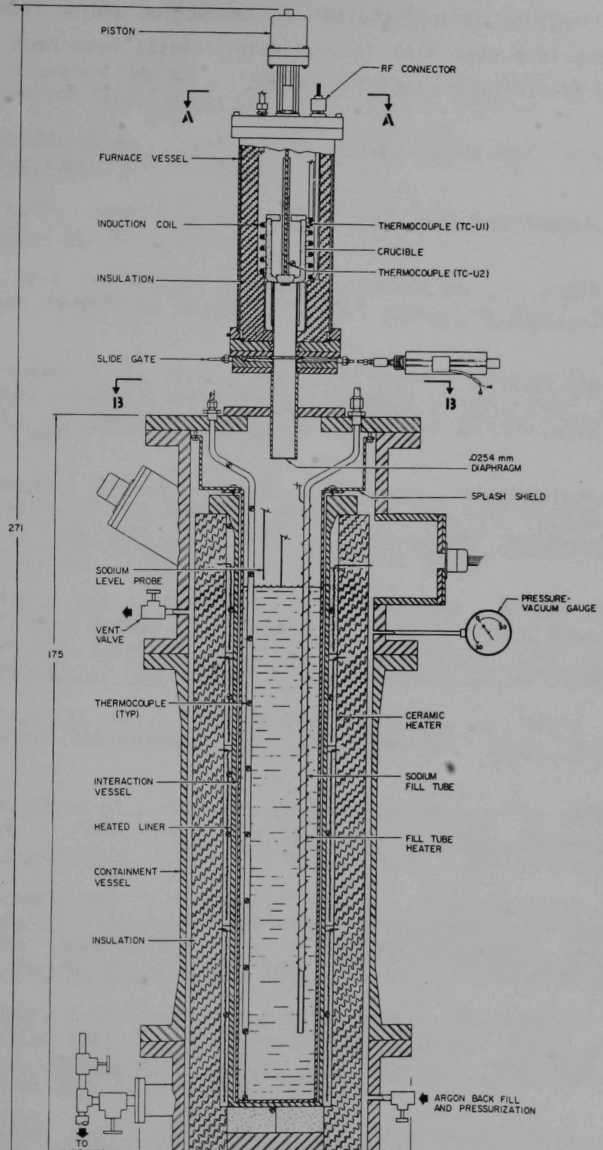

Fig. IV.9. Apparatus for Molten Fuel Stream Breakup Experiments reactor will likely be largely coolable by conduction and/or free convection provided a long term heat sink is available. Tests have been designed to experimentally assess the coolability limits.

References for Section IV

1. H. P. Planchon et al., "Implications of the EBR-2 Inherent Safety Demonstration Test," Nucl. Eng. Des., 101, 75 (1987).

2. G. H. Golden et al., "Evolution of Thermal-Hydraulics Testing in EBR-II," Nucl. Eng. Des., 101, 3 (1987).

3. D. J. Hill, "SASSYS Analysis of EBR-II SHRT Experiments," Trans. Am. Nucl. Soc., 55, 421 (1987).

4. D. J. Hill and R. A. Wigeland, "Validation of SASSYS Core Radial Expansion Reactivity Feedback Model," Trans. Am. Nucl. Soc., 56, 380 (1988).

5. G. R. Fenske, E. E. Gruber, and J. M. Kramer, "Fission Gas Retention in Irradiated Metallic Fuel," Trans. of the 9th Intl. Conf. on Structural Mechanics in Reactor Technology, Lausanne, Switzerland, Vol. C, 3, (August 1987).

6. J. M. Kramer, T. H. Hughes, and E. E. Gruber, "Validation of Models for the Analysis of the Transient Behavior of Metallic Fast Reactor Fuel," Trans. of the 10th Intl. Conf. on Structural Mechanics in Reactor Technology, Vol. C, 65, Anaheim, CA (August 1989).

7. T. H. Hughes and J. M. Kramer, "The FPIN2 Code - An Application of the Finite Element Method to the Analysis of the Transient Response of Oxide and Metal Fuel Elements," Proc. of the BNES/ENS/ANS Conf. on the Science and Technology of Fast Reactor Safety, Guernsey, UK, 427 (1986).

8. A. DeVolpi et al., "Fast-Neutron Hodoscope at TREAT: Methods for Quantitative Determination of Fuel Dispersal," Nucl. Tech., 56, 141 (1982).

9. A. E. Wright et al., "Mark-III Integral Sodium Loop for LMFBR Safety Experiments in TREAT," Proc. of the Conf. on Fast, Thermal, and Fusion Reactor Experiments, Salt Lake City, UT, Vol. I, 174 (April 1982).

10. P. H. Froehle and T. H. Bauer, "COBRA-PI: An Extension of the COBRA-3M Code Dynamically Dimensioned to Accept Pin Bundles of Any Size", Advances in Reactor Computations, Proc. of the ANS Mathematics and Computation Division Topical Meeting, Salt Lake City, UT, 211 (March 1983).

11. T. H. Bauer, G. R. Fenske, and J. M. Kramer, "Cladding Failure Margins for Metallic Fuel in the Integral Fast Reactor," Trans. of 9th Intl. Conf. on Structural Mechanics in Reactor Technology, Lausanne, Switzerland, Vol. C, 31 (August 1987).

12. J. D. Gabor, R. T. Purviance, R. W. Aeschlimann, and B. W. Spencer, "Dispersion and Thermal Interactions of Molten Metal Fuel Settling on a Horizontal Steel Plate through a Sodium Pool," ANS Proc. 1989 National Heat Transfer Conf., 4, 291, Philadelphia, PA (August 1989).

References for Section IV
(Contd.)

13. J. D. Gabor, R. T. Purviance, R. W. Aeschlimann, and B. W. Spencer, "Breakup and Quench of Molten Metal Fuel in Sodium," Proc. of the Intl. Topical Meeting on Safety of Next Generation Power Reactors, 838, Seattle, WA (May 1988).

14. J. D. Gabor, R. T. Purviance, R. W. Aeschlimann, and B. W. Spencer, "Characterization of IFR Metal Fuel Fragmentation," Trans. Am. Nucl. Soc., 54, 251, Dallas, TX (June 1987).

V. CORE DESIGN DEVELOPMENT

A. Design for Passive Reactivity Shutdown

The goal of passive safety is to so design the reactor that in the event of an off normal condition, it brings itself to a safe shutdown condition by reliance on "inherent processes" i.e., without reliance on devices requiring switching or outside sources of power. Passive reactivity shutdown can be achieved by designing the reactors for favorable relationships among the power, power/flow, and inlet temperature coefficients of reactivity, for high internal conversion ratio (yielding small burnup control swing), and for a primary pump coastdown time appropriately matched to the delayed neutron hold back of power decay upon negative reactivity input. In the following paragraphs we first identify what these favorable relationships among reactivity coefficients should be; then we discuss the design choices which produce these relationships.

The reactor core can be influenced by external events only through changes in the coolant inlet temperature and flow rate or through externally induced reactivity changes owing to control rod motion or seismically-induced core geometry changes. Of these three communication paths, the balance of plant (BOP) can influence the core only through coolant inlet temperature. These three all-encompassing paths by which external changes can influence the reactor are embodied in the three generic anticipated transient without scram (ATWS) events: loss-of-flow (LOF) without scram, loss-of-heat-sink (LOHS) without scram, and rod runout transient overpower (TOP) plus two overcooling accidents, pump overspeed and chilled T_{in}. (It is assumed that the reactivity consequences of seismic-induced core geometry changes can always be scoped by an appropriate rod runout TOP initiator and a degradation in radial expansion negative feedback.)

Given the limited ways the core can be influenced by external events, it is useful to write a quasi-static reactivity balance as

$$0 = \Delta\rho = (P-1)A + (P/F-1)B + \delta T_{in}C + \Delta\rho_{ext} \qquad (1)$$

where

P, F = normalized power and flow, respectively,

δT_{in} = change from normal coolant inlet temperature,

$\Delta\rho_{ext}$ = externally-imposed reactivity,

A, B, C = integral reactivity parameters that are measurable on the operating plant via perturbations introduced through the communication paths,

C = inlet temperature coefficient of reactivity (¢/°C),

$(A+B)$ = reactivity decrement experienced in going to full power and flow from zero-power isothermal at coolant inlet temperature (¢),

B = power/flow coefficient (¢/100% power/flow), and

A = net (power-flow) (¢) reactivity decrement (¢).

In transients which are slow enough to preclude nonequilibrium stored energy in the fuel pins and delayed neutron nonequilibrium, Eq. (1) can be solved for the new power level after inherent adjustment of the reactor core to a new set of externally-controlled conditions of coolant flow, inlet temperature, and externally induced reactivity. The power adjusts up or down to compensate through the power coefficient any reactivity change caused by external events.

When this analysis approach is taken for all possible external perturbations which the core can experience through these communication paths to the external world; i.e.:

1. Primary-pump-induced events (changes in flow)
    a. LOF
    b. pump overspeed

2. Control-rod-induced events (changes in external reactivity)
    a. "slow" TOP

3. BOP-induced events (changes in inlet temperature)
    a. LOHS
    b. chilled inlet temperature

the asymptotic core outlet temperatures which result from the balance of reactivity, [Eq. (1)] can be expressed as simple ratios of the measurable integral parameters (see Table V.1). It is seen in Table V.1 that the asymptotic incremental change in core outlet temperature relative to its normal value (expressed in units of full power steady state coolant temperature rise, ΔT_c) is always determined by three dimensionless ratios of the measurable, integral reactivity parameters; specifically,

A/B,

$C\Delta T_c/B$,

and

$\Delta\rho_{TOP}/B$,

where

$$\Delta\rho_{TOP} = \frac{\text{BOEC hot excess}}{\text{number of operational rods}} \times \left(\begin{matrix}\text{first rod out}\\ \text{interaction factor}\end{matrix}\right), \qquad (2a)$$

with

$$\begin{matrix}\text{BOEC hot}\\ \text{excess}\end{matrix} = (\text{burnup control swing}) + (\text{excess to cover uncertainties}) \qquad (2b)$$

In Eq. (2a) and Table V.1, a single rod runout TOP has been assumed.

TABLE V.1. Quasi Static Reactivity Balance Results for Unprotected Accidents

	Asymptotic State				Intermediate State	Indicated Trend for Inherent Shutdown*	
	P	F	δT_{in}	δT_{out}			
LOHS	~ 0	1	$\frac{A+B}{C}$	$\left(\frac{\frac{1+A/B}{C\Delta T_c}}{B} - 1\right)\Delta T_c$	Monotonic transition to asymptotic	A+B C	Small Large
TOP	~ 1 (after rise in T_{in} due to BOP heat removal limit)	1	$\frac{\Delta\rho_{TOP}}{-C}$	$\delta T_{out} = \delta T_{in}$ $= \left(\frac{\Delta\rho_{TOP}/B}{-C\Delta T_c/B}\right)\Delta T_c$	Initial rise at constant T_{in} $P = 1 + \frac{-\Delta\rho_{TOP}/B}{1 + A/B}$ $\delta T_{out} = \left(\frac{-\Delta\rho_{TOP}/B}{1 + A/B}\right)\Delta T_c$	A+B C $\Delta\rho_{TOP}$	Large Large Small
LOF	~ 0	Natural Circulation	0	$(A/B)\Delta T_c$	Overshoot relative to delayed neutron hold-back of power decay minimized if $\lambda\tau(1+A/B)^2\lvert B\rvert >> 1\$$	A B τ	Small Large Long
Chilled Inlet	$1 - \frac{C\delta T_{in}}{A+B}$	1	$\lvert -\delta T_{in}\rvert \le (T_{inlet} - T_{Na\ freeze}) \approx 1.5\ \Delta T_c$	$\left(\frac{C\Delta T_c/B}{1 + A/B} - 1\right)(-\delta T_{in})$	Monotonic transition	C A+B	Small Large
Pump Overspeed	$\frac{1 + A/B}{1/F + A/B}$ (always > 1)	F>1	0	$\left[\frac{1}{1 + \frac{A/B}{1+A/B}(F-1)}\right]\Delta T_c$ (always < 0)	Monotonic transition	A B	Negative Negative

*Conflicts are seen to exist between desirable trends for different ATWS events. Resolution of these conflicts is discussed in the text.

Of all of these unprotected accident scenarios, it is only in the first few tens of seconds of a LOF that the quasi-static reactivity balance is seriously in error. During that short time following initiation of a LOF, the delayed neutron hold back time, $1/\lambda$, of the power decay may be longer than the pump coastdown time, τ, thereby causing a power/flow overshoot which yields a core outlet temperature overshoot relative to the asymptotic value given in Table V.1. The size of this overshoot can be controlled by choice of the pump time constant, τ; specifically overshoot relative to the asymptote is reduced, the larger is the value of the quantity,

$$\tau\lambda\ (1 + A/B)^2|B|,$$

relative to 1$.

Examination of Table V.1 shows that all possible unprotected accident scenarios* which are initiated through the three all-encompassing communication paths to the reactor will lead to acceptable asymptotic core outlet temperatures if the following sufficient (but not necessary) ranges for the measurable integral reactivity parameters are met:

$$A/B \leq 1,\ 1 \leq \frac{C\Delta T_C}{B} \leq 2\ ,\ \text{and}\ \frac{\Delta\rho_{TOP}}{|B|} \leq 1\ , \tag{3a}$$

where A, B, C are all negative. The peak overshoot in the LOF will be minimal if

$$\tau\lambda(1 + A/B)^2|B| > 1\$. \tag{3b}$$

Under these conditions, the incremental increase in the outlet temperature above its normal full power, full flow condition never exceeds one ΔT_C.

The value of the quasi-static approach is that it provides a conceptual

---

*The assumptions of the quasi-static approach will be violated in TOPs with periods of a size comparable to or shorter than the fuel pin and fluid time constants, which are in the range of 1 to 5 sec. Otherwise, the above results are general.

framework for guiding design decisions in a direction favoring passive safety features. The values of the ratios, A/B, $C\Delta T_c/B$, and $\Delta\rho_{TOP}/B$ can be substantially affected by the choices made in the core design. Knowing what the trends should be to promote inherent shutdown and to suitably decouple the reactor core from the BOP, we can optimize the core design choices to achieve the desired trends.

The definitions of the reactivity parameters, e.g., $B = \partial\Delta\rho/(\partial P/F)$, $C = \partial\Delta\rho/\partial T_{in}$, etc., are used to express A, B, and C in terms of physical reactor phenomena such as Doppler coefficient of reactivity (α_D), sodium density coefficient (α_{Na}), fuel axial expansion coefficient (α_E), etc. The resulting definitions of A, B, and C in terms of physical reactivity components are displayed in Table V.2. For example, A is equal to the Doppler plus fuel axial expansion coefficients of reactivity multiplied by the incremental temperature rise of the fuel relative to the coolant.* The dimensions of A are expressed in dollars of reactivity, and A ranges in value from 25 cents to 2 dollars for current LMR designs. The P/F coefficient, B, and the inlet temperature coefficient, C, like A, contain terms due to Doppler and fuel axial expansion, but also contain terms tied to coolant temperature at the inlet and outlet plena such as sodium density and grid plate and above core load pad thermal dilation (core radial expansion). Table V.2 indicates the size ranges of the individual terms for typical LMR modular cores fueled with mixed oxide and fueled with U-Pu-Zr metal alloy fuels; all values of α have units of dollars per degrees Celsius and all except α_{Na} are negative.

It is evident that the three integral reactivity parameters, A, B, and C and the TOP initiator, [(Eq. 2)], are all closely interrelated--any core design choice will affect the values of them all--sometimes in conflicting ways. Making design choices so as to achieve the trends which promote inherent shutdown (small A and $\Delta\rho_{TOP}$ and large B and C) requires a global core design strategy with the compromises clearly in view. The introduction of the

---

*Whether α_e goes in A or not depends on whether the fuel is free of the clad (fuel elongation depends on fuel temperature and α_e goes in A) or is linked to the clad (fuel elongation depends on clad i.e., coolant temperature and α_e does not go in A). For metal fuel, linkage to the clad occurs after several atom percent burnup.

metallic fuel provides the key design variable enabling a design solution to enhance inherent shutdown performance. Specifically, A and $\Delta\rho_{TOP}$ can be made small by choice of the metallic fuel and B and C can be made large by core layouts which enhance axial and radial leakage. The fuel Doppler and fuel axial expansion coefficients affect the values of B and C (which should be made large) as well as A (which should be made small). However, the incremental temperature rise in the fuel $\overline{\Delta T}_f$, which acts on these reactivity coefficients, appears in A only:

$$A = -(\alpha_D + \alpha_E)\overline{\Delta T}_f$$

and is used as the key design variable to achieve a low value of A. Because of the factor of 10 higher thermal conductivity of metal fuel relative to oxide and because of the sodium bond, metallic fuel pins enjoy a very low $\overline{\Delta T}_f$ at characteristic LMR conditions (e.g., with ~0.30-in. pins and at ~15 kW/ft peak linear heat rating, $\overline{\Delta T}_f \simeq 150^\circ C$). For comparable LMR designs, the net (power-flow) coefficient (A) can be reduced by factors of 6 or so (from 1.50 dollars to 25 cents) by employing the metallic fuel vs oxide fuel.

The P/F coefficient, B, and the inlet coefficient, C, rely on the same physical feedback mechanisms (see Table V.2). A strategy to make them large is to design for large net negative core radial expansion plus sodium density coefficients. Both the sodium density and the radial expansion coefficients can be made more negative by designing the core to enhance axial leakage; the positive sodium density coefficient is reduced by increasing the negative leakage component through the use of appropriate height-to-diameter (H/D) ratio and also by use of heterogeneous layouts. The negative radial expansion coefficient (due to increasing core interassembly gap upon core support thermal dilation) becomes more negative as the axial leakage fraction is increased and is thus also sensitive to H/D.

The TOP initiator could be made small either by increasing the number of control rods or by designing for reduced burnup control swing. The design strategy is to achieve high internal conversion by maximizing the ^{238}U content of the core and maximizing the effective η of the fuel (neutrons released per neutron absorbed in the fuel) by hardening the spectrum. High internal

TABLE V.2. Components of Power and Power/Flow Reactivity Decrements and of T_{in} Coefficient of Reactivity

A (¢) = $\{$	α_D +	$\left[\begin{array}{ll}0 & \text{Bonded to Cladding}\\ \alpha_\ell & \text{Free of Cladding}\end{array}\right.$			$\}$ * $\overline{\Delta T_f}$ (ave. fuel - ave. coolant temperature)
B (¢) = $\{$	α_D +	α_ℓ	+ α_{Na} +	$2\alpha_R$	$\}$ * $\frac{\Delta T_c}{2}$ (ave. coolant- T_{inlet} temperature)
C (¢/°C) = $\{$	α_D +	α_ℓ	+ α_{Na} +	α_R	$\}$
	Doppler	Fuel axial expansion	Na density	Radial expansion	
Typical Size (¢/°C)	-0.05 to -0.1	-0.1	+0.15 to 0.02	-0.2 to -0.3	
	Associated with fuel temperature	?	Associated with coolant temperature		

conversion designs are favored by various combinations of large pins, internal blankets, hard spectrum, and low enrichment. Again the IFR metallic fuel provides unique advantages in both high effective ^{238}U number density and in large effective η. For example, in an internal blanket assembly with 50% fuel volume fraction, U-Zr metallic alloy pins at 85% smear density provide 35% more ^{238}U atoms than will UO_2 pins at 93% smear density and 97.7% pellet density. In addition, the harder spectrum achievable in a metal fueled core provides 20% more excess neutrons available for breeding (because of smaller fissile α and more fertile fast fissions) than are available in the softer oxide spectrum.

The design strategy elaborated above has been used to produce the metal fueled core whose safety performance in ATWS accidents has been displayed in Section IV.C. There it is shown that because of the favorable ratios among power, power to flow, and inlet temperature coefficients, the reactors do indeed passively shut themselves down in response to unscrammed accident scenarios.

B. Uncertainty Reduction in Passive Safety Response

The reactivities involved in passive shutdown are numerically extremely small--i.e., several cents--and moreover they derive not only from the traditionally-considered temperature dependencies of densities and of Doppler broadening but also from very subtle geometrical displacements. For example a 10°C temperature rise at the grid plate dilates a 2-m-diameter core by only 4 mm and yet it comprises one of the important reactivity feedbacks for passive shutdown. In a generic way:

$$\begin{aligned} \Delta\rho &= \Delta T * \left(\frac{\partial\rho}{\partial T}\right) && \text{Na density \& Doppler} \\ &+ \Delta T * \left(\frac{\Delta\ \text{Position}}{\Delta\ \text{Temperature}}\right) * \left(\frac{\partial\rho}{\partial\ \text{Position}}\right) && \text{radial and axial expansion \& bowing} \qquad (4) \end{aligned}$$

In view of the small sizes of the reactivities involved and of the subtleness of the thermo/structural processes on which major components of the reactivity feedbacks depend, one might anticipate that unavoidable uncertainties in the values of nuclear and thermo/structural properties present a hopeless situation as regards reliability of passive shutdown. However, this is not so because two principal features mitigate the impact that uncertainties and variability of key neutronics, thermohydraulic, and structural properties impute to passive shutdown performance.

First, as summarized in Table V.1, the passive shutdown performance depends not on individual reactivity coefficients but rather on groupings of feedbacks, A, B, C, which are measurable on the operating reactor. Thus, irrespective of the pre-construction level of uncertainty in individual reactivity coefficients, and irrespective of the core-to-core variability of manufactured equipment and of aging effects which change in-core equipment, it will always be possible to monitor the actual values of the inlet temperature coefficient, C, the power reactivity decrement, (A+B), and the flow coefficient of reactivity, B, on any operating reactor. Given the measured values of A, B, and C (and the measurement precision), one can ascertain from the formulas in Table V.1, and the criteria of Eq. (3) whether or not the passive shutdown performance will be capable of maintaining the core in a safe condition. A requirement on the frequency of measuring the integral parameters and on the allowed bands into which their values must fall will provide a means to assure that either the feedbacks do, in fact, provide for safety, or that the reactor must be shut down or derated until safety can be assured.

Second, the asymptotic core outlet temperature changes required to passively shut down ATWS events are insensitive to variations in the values of individual reactivity coefficients which comprise the overall integral parameters, A, B, and C defined in Table V.2. This is because the same reactivity effects contribute both to the reactivity addition which accompanies power reduction and to the reactivity subtraction which accompanies core isothermal temperature rise; and these reactivities cancel by definition in passive shutdown. Consider, for example, core radial expansion coefficient in the LOHS event. As the inlet temperature goes up, the grid plate dilates, causing a negative reactivity insertion from the radial expansion coefficient of reactivity. On the other hand, as the power is reduced, the coolant ΔT rise across the core is reduced, the above core load pads cool causing the top of the core to contract relative to the bottom of the core, and this leads to a positive reactivity input from the radial expansion coefficient. Since the radial expansion coefficient of reactivity contributes to both the reactivity addition and the reactivity subtraction processes--which asymptotically cancel--uncertainties or variations in this reactivity coefficient tend to self cancel also. In a mathematical sense, the uncertainties in the components of the numerator and denominator of the formulas for δT_{out} in Table V.1 are positively correlated, tending to reduce their impact on the variance of δT_{out}. This will happen not only for the neutronics reactivity coefficients, but also for the thermo/structural components [see Eq. (4)] of the reactivity feedbacks comprising the global reactivity parameters A, B, and C. As a result of the partial self cancellation of individual reactivity coefficient uncertainties or variations, the power reactor will experience less variation in its passive shutdown performance in response to unavoidable variations in composition and geometry which derive from manufacturing tolerances and aging effects.

There are two key places where the partial self cancellation of uncertainties as they affect passive shutdown consequences fail to take place. The first is for the TOP ATWS event where the uncertainties of the components comprising the BOEC hot, all-rods-out, reactivity excess are poorly correlated with those of the reactivity feedback coefficients. Here, the initial* core outlet temperature increase in response to an unprotected single rod runout is given by:

$$\delta T_{out} = \Delta T_c \left(\frac{\text{BOEC Excess}}{A+B}\right)\left(\frac{\text{First Rod Out Interaction Factor}}{\text{No of primary rods}}\right) \qquad (5)$$

---

*If the initial power rise is large enough to boil dry the steam generator, then a loss of heat sink on top of the TOP will determine the asymptotic state.

with (BOEC Excess) given by Eq. (2b). In Eq. (2b) the (Excess to Cover Uncertainties) component of the BOEC Excess is provided for by over-enrichment of the manufactured assemblies to cover contingencies such as:

$$\text{(Excess to Cover Uncertainties)} = \begin{bmatrix} \text{(uncertainty in burnup control swing)}^2 \\ + \text{(uncertainty in cold to hot reactivity defect)}^2 \\ + \text{(uncertainty in cold critical mass)}^2 \\ + \text{(uncertainty due to fuel manufacturing tolerance)}^2 \end{bmatrix}^{1/2} \quad (6)$$

It is evident that the uncertainties in Doppler, sodium density, and radial and axial expansion temperature coefficients of reactivity which comprise the (A+B) factor in the denominator of Eq. (5) are but loosely correlated with the uncertainties in the factors determining the burnup control swing in the numerator of Eq. (5). Thus, one does not expect a partial uncertainty self cancellation as was enjoyed for the other ATWS events.

The second instance where uncertainties relevant to passive shutdown performance are poorly correlated with those of the reactivity feedback coefficients is for the local power peaking factor which is a necessary factor for converting the global core mixed mean coolant outlet temperature rise to a local, hot channel, value required in an actual assessment of margin to core damage in response to the passive shutdown of ATWS events.

$$\begin{aligned} \delta T_{out}\,\text{(local)} = {} & \delta T_{out}\,\text{(core mixed mean)} \\ & * \text{[Local Peaking Factor (Burnup State, Rod Position)]} \\ & * \text{[Local/Ave Flow Redistribution]} \end{aligned} \quad (7)$$

During the licensing phase of a new reactor type, the measurability of the A, B, and C parameters cannot be exploited and predictions of accident outcomes must be based on calculations. And while uncertainty cancellation occurs, the two exceptions discussed above give rise for a need for further uncertainty reduction in the inputs to the calculations. Prior to power reactor construction, in order to reduce the neutronics uncertainties which importantly impact calculational predictions of passive shutdown performance, we use critical experiment measurements; and the formal data fitting methodology is used to apply the critical experiment results to the design. This methodology updates a multigroup cross section vector, $\underline{T}$, having covariance matrix, $\underline{M}$, to a revised set, $\underline{T}'$ and $\underline{M}'$, by using least squares fitting to find that set of cross section revisions ($\underline{T}'-\underline{T}$) which minimizes the square of the deviation between an ensemble of criticals measurements, $\underline{R}$, and calculations of those measurements, $\underline{C}(\underline{T})$, based on the original cross sections, $\underline{T}$. The formal results are given by:

$$\underline{T}' - \underline{T} = \underline{MG}^{T}\, \underline{W}\, (\underline{C} - \underline{R}) \tag{8}$$

$$\underline{M}' = \underline{M} - \underline{AWA}^{T} \tag{9}$$

where

$$\underline{W} = [\underline{GMG}^{T} + \underline{V}]^{-1}$$

$$\underline{A} = \underline{MG}^{T}$$

and

$\underline{M}$ = covariance matrix for the cross section, $\underline{T}$

$\underline{V}$ = covariance matrix for the criticals measurements, $\underline{R}$

$\underline{G}$ = matrix of sensitivity coefficients = $\dfrac{\%\text{ change in R}}{\%\text{ change in }\sigma}$

(computed using unadjusted cross sections, $\underline{T}$).

The data fitting methodology improves the calculational predictions of the critical experiment results to which the fitting is done, yielding new predictions:

$$\underline{C}' = \underline{C}(\underline{T}) + \underline{G}^{T}(\underline{T}'-\underline{T})$$

and reduces their variance to a value which is near that of the criticals measurements--which are generally of a higher precision than can be calculated:

$$\begin{aligned}(\overline{\underline{C}'^2} - \overline{\underline{C}'}^2) &= \underline{G}\ \underline{M}'\underline{G}^T \\ &= \underline{GMG}^T - (\underline{GMG}^T)^T\ \underline{W}\ (\underline{G}^T\underline{MG}) \\ &= \underline{GMG}^T\ \ \{\underline{I}-\underline{I} + (\underline{GMG}^T + \underline{V})^{-1}\underline{V}\} \\ &\simeq \underline{V}\end{aligned}$$

if $\underline{V} << \underline{G}^T\underline{MG}$.

It is noted that the cross sections per se are not necessarily improved either by a movement of their values closer to physical truth or by a reduction of their uncertainties. It is the predictions as calculated using a specified modeling and computer code set which improve.

The strength of the data fitting methodology is that if the dependences on cross sections of the power reactor are "the same" as those of the ensemble of critical experiments, the improvement in prediction and the reduction in uncertainty which is achieved for the criticals carry over to the power reactor as well. For example, for a power reactor having a sensitivity matrix, $\underline{S}$, relating quantities of interest to cross sections, the adjusted cross sections yield corrected power reactor calculational predictions:

$$\underline{C}'_{\text{power}} = \underline{C}'(\underline{T})_{\text{power}} + \underline{S}^T(\underline{T}'-\underline{T}) \tag{10}$$

and whereas the original uncertainties in calculationally-predicted quantities are

$$\underline{S}^T\underline{MS}$$

after data adjustment they are reduced to

$$\underline{S}^T\underline{M}'\underline{S} = \underline{S}^T\underline{MS} - (\underline{GM}^T\underline{S})^T\ \underline{W}(\underline{GM}^T\underline{S}). \tag{11}$$

so that if the projection of $\underline{G}$ on $\underline{S}$ is large, the data fitting will lead to a reduction in uncertainty of power reactor quantities. This property of the data fitting methodology to replace the ad hoc uncertainty estimates of the bias factor method with estimates which are rigorously founded in the mathematics of least squares fitting is uniquely important in a licensing regime where credit is being given for passive shutdown properties. Moreover, the formal data fitting methodology permits us to reduce uncertainties on even those reactor performance quantities which are not directly measurable on a critical experiment. To the degree that the projection of the power reactor's sensitivity vectors, $\underline{S}$, onto those of the critical, $\underline{G}$, is large, the critical experiments help to reduce uncertainty in unmeasurable quantities. The salient example here is burnup reactivity swing. Even though a burnup reactivity swing cannot be measured on a critical assembly, the uncertainty in its value can be reduced by measurements such as c^{28}/f^{49}, $(1 + \alpha^{49})$, and small sample worth, ρ^{28}/ρ^{49}. As an example, Table V.3 indicates that dramatic reductions in the burnup reactivity swing uncertainty for a 900 MWth core design have been achieved by use of this methodology.

TABLE V.3. Use of Data Adjustment to Critical Experiments to Reduce Uncertainty in Burnup Reactivity Swing

	Burnup Swing and Standard Deviation (% Δk)
Before Adjustment	0.185 ± 0.250
After Adjustment	0.520 ± 0.073

C. Core Restraint Design and Its Sensitivity to Design and Manufacturing Variations

The core restraint design selected for the Advanced LMR is the limited-free-bow concept similar to that used by FFTF, MONJU, and CRBR. This concept uses a rigid circumferential ring in conjunction with full circumference load pads to provide a firm limit on the radial expansion at the top of the assemblies as well as a firm limit on the core compaction at an elevation just above the core. The restraint ring, located at the top elevation of the core assemblies, is sized to allow sufficient gap in the array for refueling while preventing excessive displacement of the assemblies during a seismic event. It must also ensure that the core assemblies are fully compacted at full power-to-flow ratio. The above core load pads must be sufficiently stiff so that additional forces due to thermal bow of the assemblies do not further compact the core.

Limited-free-bow core restraint designs rely on the dominate negative radial thermal gradients which exist in the core at power to lock individual assemblies in place. The assemblies take an "S" shape as their free thermal bow (concave out) is restrained by the top ring, the load pad plane, and the nozzle support. Higher temperatures cause the above core load pad plane to expand and steeper thermal gradients cause a more pronounced "S" shape. Both of these phenomena result in expansion of the core and thus lead to negative reactivity feedback.

Efforts under the IFR program have focused on developing simplified models of core radial expansion which are valid in the power-to-flow range greater than unity. Because the models are analytical, as opposed to numerical, they provide a clear understanding of the relationship between the underlying physical parameters and the magnitude of the resulting core expansion, and moreover, facilitate a quantification of the sensitivity of core expansion to various design parameters and to the uncertainties in the underlying physical parameters.

The Single Assembly Models

The single assembly models are based on analysis of the deformation of a single driver assembly at the core boundary. It assumes that at full power-to-flow ratio, the planes of load pads above the core and interior to the core boundary are fully compacted. It also assumes that the top load pads exterior to the core boundary form a continuous load path to the restraint ring. These assumptions are justified by test results and detailed analysis for many such core restraint designs. Moreover, the maximum displacement reactivity worths and the maximum thermal gradients occur at the outer driver assembly.

The following parameters are then used to formulate the radial displacement of the assembly at the midcore elevation: the assembly length, the midcore elevation, the core height, and the location of the above core load pad; the assembly bending stiffness, the load pad stiffness, the gap size at the above core and top load pads; the core inlet temperature, the outlet temperature, the maximum temperature gradient, the temperature of the restraint ring, and the thermal expansion coefficient for the various materials. Finally, the initial shape of the assembly due to creep, swelling, or manufacturing tolerances is included. Two forms of the single assembly model have been considered; one assumes the nozzle has a pin support at the grid plate while the other assumes cantilever support.

The solution to the Bernouli-Euler beam equations for the single driver assembly gives the radial displacement at the mid-core elevation. This solution can be collected into terms proportional to the core inlet temperature, to the core temperature rise, and to the restraint ring temperature, which correspond to various time scales during accident scenarios.

Some of the conclusions we have reached using this model include:

(1) The radial expansion coefficients of grid plate temperature and core temperature rise are both positive and approximately equal for a broad range of designs.

(2) The effect of restraint ring temperature increases is to compact the core but the magnitude is small.

(3) For most designs the core expansion due to thermal growth of the plane of the above core load pads represents 50-70% of the total, the remainder is due to bowing of the assemblies.

(4) It is essential that the above core load pads be sufficiently stiff relative to the bending stiffness of an assembly so that the plane of load pads does not compact due to bowing forces. Full circumference loads pads are sufficiently stiff.

(5) Cantilever support at the nozzle end leads to reduced radial expansion.

(6) The gaps in the model can be used to represent uncertainties due to manufacturing tolerances in the load pads. While achieving core lockup is sensitive to these gaps, the magnitude of core expansion, once lockup has been achieved, is not.

The simple analytical model provides a method for formal propagation of underlying uncertainties in temperatures, material properties, and dimensions into uncertainties in radial expansion reactivity. This is done by choosing a nominal design, estimating the uncertainties in the design parameters, and using partial derivatives of the temperature coefficients of radial expansion to determine the resulting uncertainties in radial expansion. Our studies have shown that uncertainties in temperature are the largest contributor to radial expansion reactivity. Uncertainties in the structural portions of the model also contribute significantly to the uncertainty in reactivity change due to core temperature rise. Core physics uncertainties along with structural model uncertainties are smaller contributors to reactivity changes due to rise in the grid plate temperature. Geometric uncertainties, including rather large uncertainties in the available gaps, play only a minor role.

Three Assembly Model

Under some circumstances the single assembly model may not be valid. One example is where reverse thermal bow may occur in steel radial reflector assemblies due to the presence of outboard B_4C shield assemblies. In this circumstance a continuous load path may not exist between the top of the outer driver and the restraint ring. To address this phenomenon, a three assembly model was developed modeling the outer driver, the steel reflector and the B_4C shield assembly. A simplified model of irradiation creep and swelling was also added so that the topology of the core restraint could be modeled through the various regimes.

Stiffness of the reflector assembly becomes an important parameter under these circumstances. We found that a ducted reflector with the same stiffness as the driver results in a 10% loss in radial expansion due to core ΔT early in the life of the radial blanket assemblies. When the radial reflector begins to creep and swell this 10% loss is recovered. For a more flexible reflector, the reverse thermal bow is overcome by bowing forces of the driver assemblies, and no loss in radial expansion occurs above full power-to-flow except for a short period during the life of the core.

D. Trade Studies on Sodium Void Reactivity Reduction

Systematic analyses of alternative methods for reducing the sodium void worth for plutonium-fueled liquid metal reactors (LMRs) have been performed. The analyses were performed on various core designs in the 450 to 1200 MWt size range that make use of metal alloy fuel. The design alternatives encompass changes in composition and geometry. A self-consistent and comprehensive evaluation has been made of the void worth reduction achievable by various methods and of the associated core physics performance tradeoffs. The performance penalties caused by design changes that significantly reduce the void worth (ρ_{NA}) have been quantified and the relative merits of each design option have been assessed.

The design methods that were found to permit significant decreases in ρ_{NA} are (1) replacement of a fraction of the fuel content by moderator (e.g., BeO), (2) substantially increasing the sodium volume fraction in the core, (3) reducing the core volume, (4) "spoiling" core geometry by reducing the height-to-diameter ratio (H/D), (5) introducing absorbing material above the core, and (6) use of thick blanket regions to separate driver regions in the core. In general, reducing the void worth was found to cause a deterioration in core performance characteristics (e.g., a smaller breeding ratio, and larger burnup swing, fissile requirement, and core radius). However, different design options can have different quantitative effects on a specified core performance parameter for a fixed reduction in ρ_{NA}. Thus, the tradeoff between void worth and each core performance feature generally depends on the design option producing that tradeoff; certain options for reducing void worth can produce a smaller penalty in a particular performance parameter than alternative options.

Results of the neutronic evaluations indicated that the various design options for reducing ρ_{NA} consistently lead to an undesirable increase in the burnup reactivity swing. Fundamentally, design changes that reduce ρ_{NA} have an adverse effect on neutron economy and, therefore, on the internal breeding efficiency. For example, the introduction of moderating material (effective in reducing the spectral component) is harmful to the neutron economy because it displaces heavy metal and softens the energy spectrum. Similarly, a large reduction in H/D degrades the neutron balance by increasing leakage. The results of a large number of cases display this tradeoff in Fig. V.1. Based on the results, as summarized in the figure, there appears to be a lower bound on the burnup swing achievable for a given void worth; this bound decreases as ρ_{NA} increases. This "minimum burnup swing line" quantifies the best achievable tradeoff between burnup reactivity and ρ_{NA}; the slope of this line is approximately $(0.1\%\Delta k/(kk'))_{NA}/(0.16\%\Delta k)_{BU}$ or a \$1.60 increase in burnup swing by for a \$1.0 decrease in ρ_{NA}.

Many core designs (e.g., a conventional homogeneous core) fall above the minimum burnup swing line. For such cores, it is clearly possible to reduce ρ_{NA} without increasing burnup reactivity. On the other hand, the tightly coupled heterogeneous cores typical of current designs in the US appear to fall on the minimum burnup swing line, indicating that a reduction in ρ_{NA} cannot be accomplished without an increase in burnup swing. For an initial design point falling on (or near) the minimum burnup swing line, the best options for reducing ρ_{NA} are H/D reduction, moderator substitution, and increasing the thickness of blanket regions separating core zones in heterogeneous designs. Design options producing points above the minimum burnup swing line include increasing the core sodium fraction and increasing the diameter of the central blanket region of annular cores. However, for high burnup swings (>3.0%Δk), annular core layouts (with a large central blanket zone) and high-sodium-fraction cores move closer to the minimum burnup swing line and could be competitive methods for reducing ρ_{NA} and minimizing the burnup swing penalty.

The tradeoff between ρ_{NA} and breeding ratio for the various designs has also been analyzed. The trends suggest that the best tradeoff between void worth and breeding ratio is provided by cores with substantial external

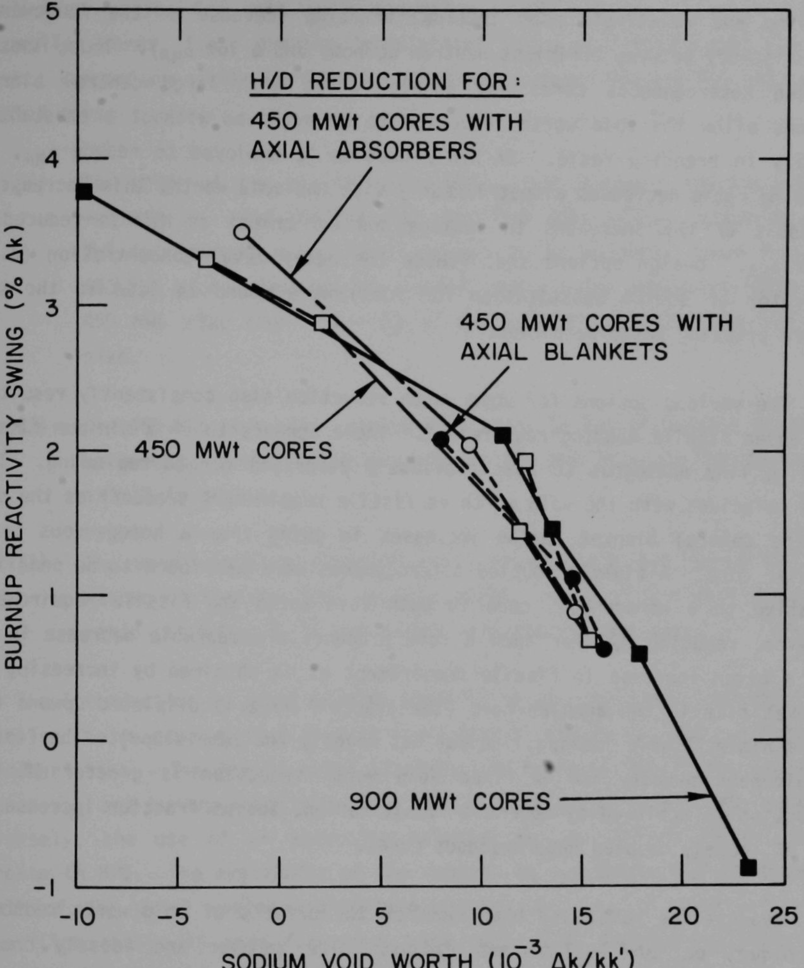

Fig. V.1. Comparison of Void Worth to Burnup Swing Trade-Offs for 900 and 450 MWt Core Sizes breeding and relatively poor internal breeding (because of the fundamental inconsistency between efficient neutron economy and a low ρ_{NA}). Thus, loosely coupled heterogeneous cores and annular cores with large central blanket regions allow the void worth reduction to be achieved without a substantial penalty in breeding ratio. If H/D reduction is employed to reduce ρ_{NA}, the breeding ratio decreases almost linearly with the void worth; this decrease is a result of the increases in leakage and enrichment as H/D is reduced to lower ρ_{NA}. Design options that reduce the heavy metal concentration (e.g., moderator or sodium substitution for fuel) were found to lead to the most severe breeding ratio penalties.

The various options for void worth reduction also consistently result in increased fissile loading requirement. There appears to be a minimum fissile loading line analogous to that previously described for burnup swing. This line coincides with the void worth vs fissile requirement tradeoff as the size of the central blanket region increases in going from a homogeneous to an annular core. A tightly coupled heterogeneous core was found to be penalized relative to a homogeneous core in both void worth and fissile requirement. However, reducing H/D for such a core produces a comparable decrease in ρ_{NA} for a given increase in fissile requirement as is obtained by increasing the blanket size in the annular core (the tradeoff line is displaced upward from the minimum fissile loading line but has roughly the same slope). The fissile requirement penalty for a fixed void worth reduction is greater if this reduction is achieved by moderator substitution, sodium fraction increase, or use of loosely coupled heterogeneous cores.

Evaluations have also been made of the effects of void worth reduction techniques on core volume and radius. The annular and loosely coupled concepts lead to large increases in both volume and radius, while the reduction of H/D preserves volume but leads to a large increase in core radius. On the other hand, material substitutions (e.g., sodium or moderator for fuel) performed for a fixed core geometry enable void worth reduction with no penalty in core volume or radius.

Another option for void worth reduction is the use of (a larger number of) smaller cores; i.e., greater "modularity" for a specified total thermal output. Comparison of the performance tradeoffs between 450 and 900 MWt cores revealed that:

(1) The slope of the tradeoff between ρ_{NA} and burnup swing (as H/D is varied) is very similar for the two core sizes, although the "minimum burnup swing line" appears to be slightly lower for the 450 MWt size. However, the lowest burnup swing achievable with the 450 MWt size (for $H/D \simeq 1$) is not as small as with the 900 MWt size.

(2) The 450 MWt core size results in a slightly less favorable tradeoff between ρ_{NA} and fissile requirement per MWt than the 900 MWt size as H/D is varied.

(3) The void worth vs breeding ratio trends with H/D variation are rather similar for the two core sizes. However, a higher breeding ratio (at $H/D \simeq 1$) is achievable with the 900 MWt size.

The introduction of axial blanket material or absorbing material into the above- and below-core regions affects the tradeoff between ρ_{NA} and performance characteristics. The use of axial blankets was found to affect the tradeoff between ρ_{NA} and burnup reactivity in a manner similar to an increase in H/D. Conversely, the use of an absorbing material has an effect similar to a decrease in H/D. The magnitudes of the changes in ρ_{NA} and burnup swing (as a result of the axial region composition change) are greater when the axial composition change is made for cores with small H/D, fundamentally because axial leakage increases with decreasing H/D. The principal benefit of axial blanket use is the improved tradeoff between ρ_{NA} and breeding ratio. However, axial blanket use would make other tradeoffs less favorable (for example the tradeoff between ρ_{NA} and core radius). Conversely, the use of absorbing material above and below the core permits a decrease in core radius for a specified void worth but also results in less favorable tradeoffs between void worth and other performance parameters such as fissile requirement and breeding ratio.

To summarize, our results indicate that

(1) The penalties in burnup reactivity swing and fissile requirement can be minimized by use of a "tightly-coupled" radially heterogeneous configuration of minimum volume consistent with fuel rating limits and by adjusting the core height-to-diameter ratio to a value sufficiently small to yield an acceptable void worth. For a 450 MWt core, reduction of H/D from 0.6 (36 in. core height) to 0.25 (20 in. height) with the core volume fixed reduces ρ_{NA} from \$3.60 to 0, but also increases the burnup reactivity swing by 1.5% δk (~\$4.50), increases the fissile mass requirement by 25%, reduces the breeding ratio from 0.98 to 0.73, and increases the core radius by 10 in.

(2) The reactor breeding ratio penalty can be minimized by the use of loosely coupled heterogeneous cores or annular cores with a large central blanket region. However, the tradeoff between ρ_{NA} and burnup reactivity or fissile inventory is generally less favorable than for H/D reduction. In addition, the use of thick blanket regions leads to increased core volume and heavy metal requirement, and can result in control difficulties and power shape instability if individual core regions are excessively decoupled.

(3) Penalties in core radius and core volume can be minimized by composition changes, specifically replacement of a fraction of the fuel (or steel) by sodium or a moderating material. However, the removal of heavy metal has been found to result in particularly severe core performance penalties.

Since no design option appears to be superior for all performance characteristics, choice of a "best" method for reducing void worth depends on the importance attached to the various characteristics in a particular design effort. Such a choice must also be based on broader considerations related to technical feasibility, economic viability, and overall safety.

E. Core Physics of Transuranic Self-Consumption in the Closed IFR Fuel Cycle

The IFR closed fuel cycle offers a number of favorable features for management of actinides (transuranics). These favorable features stem principally from three facets of the IFR fuel cycle. First, in the pyrochemical processing step, all transuranics naturally follow the plutonium product stream in separating the transuranics from uranium and the fission products. Thus, nearly all of the transuranic elements are routinely returned to the reactor in the closed fuel cycle. The remaining small amount of the transuranics which accompany the salt waste stream (which contains the rare earth fission products) can potentially be stripped out of the salt waste and returned to the reactor--at the expense of some rare earth fission product carryover back to the reactor. This waste stream cleanup step is currently undergoing experimental confirmation.

Second, the incremental fission product carryover to the product stream which is an unavoidable consequence of scrubbing the small amount of transuranics from the salt waste stream does not result in an incremental cost in the fuel refabrication step because the injection casting based refabrication is already done remotely. Remote processing has been utilized in the reference IFR fuel cycle because of both the inherently incomplete fission product separation in the main pyroprocessing step and the minor actinide neutron emitters resulting from continuing recycle in the closed IFR cycle.

Finally, the metallic fuel form (i.e., absence of light scattering atoms) in the reactor core leads to a particularly hard core neutron spectrum. The hard neutron spectrum enhances actinide burning through two important effects:

1. Actinides are preferentially fissioned, not converted to still higher actinides because the fission-to-capture ratio upon neutron absorption in actinide isotopes increases at high neutron energies (i.e., all transuranics became fuel--even the even mass isotopes).

2. The negative impact on core performance of the unavoidable fission product carryover from the waste stream scrubbing operation is minimal because the capture cross sections of the fission products are reduced at higher energies.

The actinide management features of the IFR fuel cycle which are listed above have important potential payoffs which are currently under investigation. First, by stripping all transuranics from the IFR waste streams and recycling them for fission in the reactor, the engineering and licensing aspects of sending IFR reprocessing wastes to a geologic repository are expected to be eased. Second, the energy content of the minor actinides can be used for resource extension because they are fissionable in the fast neutron spectrum, and when combined with the flexibility in breeding ratio of IFR designs, they can be used to provide for either a steady-state or a growing IFR energy economy. Finally, IFR designs potentially provide for a means to "burn" transuranics from a source external to the IFR cycle.

The core physics aspects of transuranic consumption in the IFR cycle have been examined; for these analyses a fissile self-sufficient (breeding ratio ≃ 1.0) 450 MWe tightly coupled radially heterogeneous core design was utilized. The fuel cycle was modeled by recycling 100% of the transuranic elements and 11% of the rare-earths as impurities. A two-year ex-core cooling, reprocessing, and refabrication interval was assumed, and the makeup feed consisted of only depleted uranium tails. The actinide isotopes ranging between U^{234} and Cm^{246} were modeled in the burnup chains. The calculation models the core behavior in the equilibrium steady state--i.e., once each isotope has reached its equilibrium level for the in-core and ex-core phases of the fuel cycle. Thus, the equilibrium cycle composition for the closed fuel cycle is one in which the production and losses exactly cancel for each isotope over the whole of the closed cycle. Table V.4 shows the resulting equilibrium cycle core discharge composition.

The relative concentrations of the transuranic isotopes from the equilibrium 450 MWe IFR discharge fuel shown in Table V.4 were compared to those for LWR once-through discharge fuel. Since the capture-to-fission ratio decreases with increasing neutron energy, the concentrations of the higher actinides, relative to their source nuclei, are lower in the IFR spectrum than in an LWR spectrum for the majority of the higher actinides. As a result, the ratio of masses of the minor actinide to the mass of fissile plutonium which is attained at equilibrium in the closed IFR cycle is a factor of six lower than that which is attained in a LWR once-through cycle. Since minor actinides dominate the very long-term waste risk potential, the IFR cycle working

TABLE V.4. LWR and IFR Transuranic Isotopics

Isotopic values are the weight fraction of the individual isotope in the total transuranic mass.

Isotope	LWR Discharge	LWR +3.17 y Cool	IFR Discharge	IFR +2.0 y Cool	$\frac{\text{LWR +3.17 y Cool}}{\text{IFR +2.0 y Cool}}$
Np-237	5.35-2	5.40-2	6.16-3	6.19-3	8.7
Pu-236	2.41-7	1.12-7	6.12-8	4.08-8	2.7
Pu-238	9.08-3	1.01-2	6.27-3	6.19-3	1.6
Pu-239	0.503	0.508	0.747	0.747	0.68
Pu-240	0.201	0.199	0.200	0.200	1.0
Pu-241	0.157	0.134	2.13-2	1.96-2	6.8
Pu-242	3.93-2	3.88-2	8.49-3	8.49-3	4.6
Am-241	3.44-3	2.51-2	6.94-3	8.63-3	2.9
Am-242m	1.14-4	1.11-4	5.11-4	5.07-4	0.22
Am-243	2.51-2	2.48-2	1.74-3	1.74-3	14.0
Cm-242	1.31-3	9.73-6	3.56-4	2.36-5	0.41
Cm-243	8.55-5	7.86-5	1.93-5	1.85-5	4.2
Cm-244	6.32-3	5.52-3	7.96-4	7.44-4	7.4
Cm-245	5.15-4	5.08-4	1.63-4	1.63-4	3.1
Cm-246	6.42-5	6.31-5	4.72-5	4.72-5	1.3
MA/fiss. Pu	0.137	0.172	0.022	0.024	7.2
MA/Pu	0.099	0.124	0.017	0.018	6.9
Np-237/MA	0.591	0.490	0.368	0.343	1.4
Am-241/MA	0.038	0.228	0.415	0.478	0.48
Am-243/MA	0.278	0.225	0.104	0.096	2.3
Np-chain	0.214	0.213	0.034	0.034	6.3

MA = sum of minor actinides
fiss.Pu = Pu-239 + Pu-241
Np-chain = Np-237 + Am-241 + Pu-241

inventory exhibits a significant reduction in long-term risk potential per unit mass of transuranics as compared to the LWR spent fuel which supplied that working inventory.

The reduction in the capture-to-fission ratios as the neutron spectrum hardens relative to an LWR has important core performance benefits in the IFR--specifically, all transuranics become fuel. In particular, Am^{241} and Am^{243} have very large thermal capture cross sections and in an LWR consume more neutrons than gained by their fissions. Conversely, in the fast spectrum of the IFR their reduced capture to fission ratios lead to a slightly positive neutron balance for absorption in these nuclides. Threshold fission in fertile species such as Pu^{240} is an even more dramatic example of this effect. Thus, the minor actinides act as a poison (neutron sink) in an LWR but as a fuel in an IFR.

The IFR's hard spectrum minimizes the impact on core performance of the carryover fission products which result from the reprocessing. Estimates of the decontamination factor (DF) for elimination of rare-earth impurities in pyrometallurgical reprocessing including the salt waste scrubbing step range from 3 to 10. The neutronic effects of varying the rare-earth DF in the IFR fuel cycle model were analyzed. Increased rare-earth recycle was observed to lower the internal breeding ratio and slightly increase the burnup swing; however, the overall effect of the recycled rare earth fission products is extremely small (e.g., only a 0.077% Δk reactivity swing increase at the upper limit--25% rare earth recycle). This implies that scrubbing steps which further improve the actinide recovery from the waste but which increase the fission product impurity carryover to the reactor would easily be tolerated with the core neutronics properties.

The results which are discussed above suggest a potential in the IFR cycle to burn transuranics from an external source. Actinide burning is commonly defined in terms of amount of transuranics consumed per year. However, in the closed IFR fuel cycle only U^{238} is consumed--and transuranic fuel is created at a rate sufficient to maintain a self-sufficient fuel cycle (or--in a breeding ratio >1 design--to create excess plutonium which could be used to start up additional IFRs). The other transuranic isotopes follow plutonium in the fuel cycle and reach their own respective equilibrium level. If the IFR cycle were to be used as a net consumer of transuranics from an external source (such as LWR once-through spent fuel or from decommissioned IFR siblings), one of two approaches would be required; (1) build a sequence of new IFR fissile self-sufficient complexes and "store" the transuranics from the external source in the working inventories of a growing number of IFR facilities or (2) build IFR complexes with breeding ratios less than one and genuinely burn the transuranics by fissioning them. Both options are readily achievable from the core physics point of view and without major modifications to the core design.

The results of the studies indicate that the IFR concept potentially allows considerable flexibility with regard to management of the transuranic inventory. As the demand for energy varies, IFR's could be used to increase, maintain, or decrease the nation's transuranic inventory--while concurrently producing power, and while creating waste streams largely stripped of transuranic content.

VI. FUEL CYCLE DEMONSTRATION

From the outset of the IFR Program, an important goal has been to provide a low-cost demonstration of the pyroprocess fuel cycle at a scale which could easily be related to a future commercial operation. Refurbishment and provision of process equipment for the Hot Fuel Examination Facility-South (HFEF/S), formerly the EBR-II Fuel Cycle Facility (FCF), is currently underway to fulfill that goal. The schedule calls for facility modifications to be complete and process equipment to be installed by October 1990. Following a checkout period, it is anticipated that fuel cycle operations will begin in early 1991.

When the renewed HFEF/S is in operation there will be two main facility missions: (1) to demonstrate the entire IFR fuel cycle in conjunction with EBR-II and (2) to provide the facilities and equipment to optimize the IFR pyroprocess. The operating, maintenance, and safety record of this demonstration will be essential in establishing proof of IFR fuel cycle economics and safety.

Also, early in the IFR program (1985), a conceptual design of a commercial fuel cycle facility was developed to estimate the economic potential of reprocessing and refabricating metallic LMR fuel using the pyroprocess. The information and experience gained through the fuel cycle demonstration will be used to refine this conceptual design.

This Section reviews the status of this demonstration project, and the conceptual design and cost estimate for the commercial facility.

A. HFEF/S Modifications Project

1. Status of Facilities Modifications

The HFEF/S facility is well-suited to the IFR fuel cycle demonstration task. Like the early reprocessing of EBR-II fuel conducted in the period 1964 to 1969,[1] the new IFR process will be a relatively low-decontamination process. The process must be carried out in hot cells, with all operations and most maintenance carried out remotely. The facility was originally designed for this type of operation, but there are a number of modifications required to meet current standards for plutonium processing.

The facility consists of two shielded cells and the supporting systems. Both hot cells are highly shielded (approximately 1.5 m of high density concrete). Each cell has windows and master/slave manipulators at most of the normal work stations and both are equipped with overhead lifting and handling systems that include bridge-mounted remotely-operated cranes and electromechanical manipulators. (See Fig. VI.1.) The rectangular cell (4.6 m x 14.3 m) is an air-atmosphere cell. The larger argon cell is an inert-atmosphere cell shaped to provide an annulus about 5 m wide for process operations. The outer diameter is approximately 19 m. Operations are normally conducted from the work station windows that face the surrounding corridor. Special viewing and limited-operation work stations are available, however, in an operating area accessible from the basement and located in the center of the cell.

Though the building was constructed to U.S. Uniform Building Code criteria, a detailed dynamic seismic analysis has shown that no significant structural damage would occur as a result of the site-specific design basis earthquake (DBE). The seismic resistance of the building is primarily due to the massive, rigid cell structure which provides shielding for the operators, and which anchors the entire facility. It may be noted that the DBE for the Argonne-West site is relatively modest, with a zero-period acceleration of 0.21 g.

As mentioned above, analyses of the effect of potential natural phenomena indicate that no significant deficiencies exist in the basic facility structure. However, these calculations did indicate that an existing repair area for contaminated equipment (which was added to the roof of the facility after original construction) would not withstand the design basis wind or earthquake without loss of confinement. Furthermore, structural analysis indicated that hardening of this structure to survive such events would not be feasible. Therefore, one of the major modifications in progress

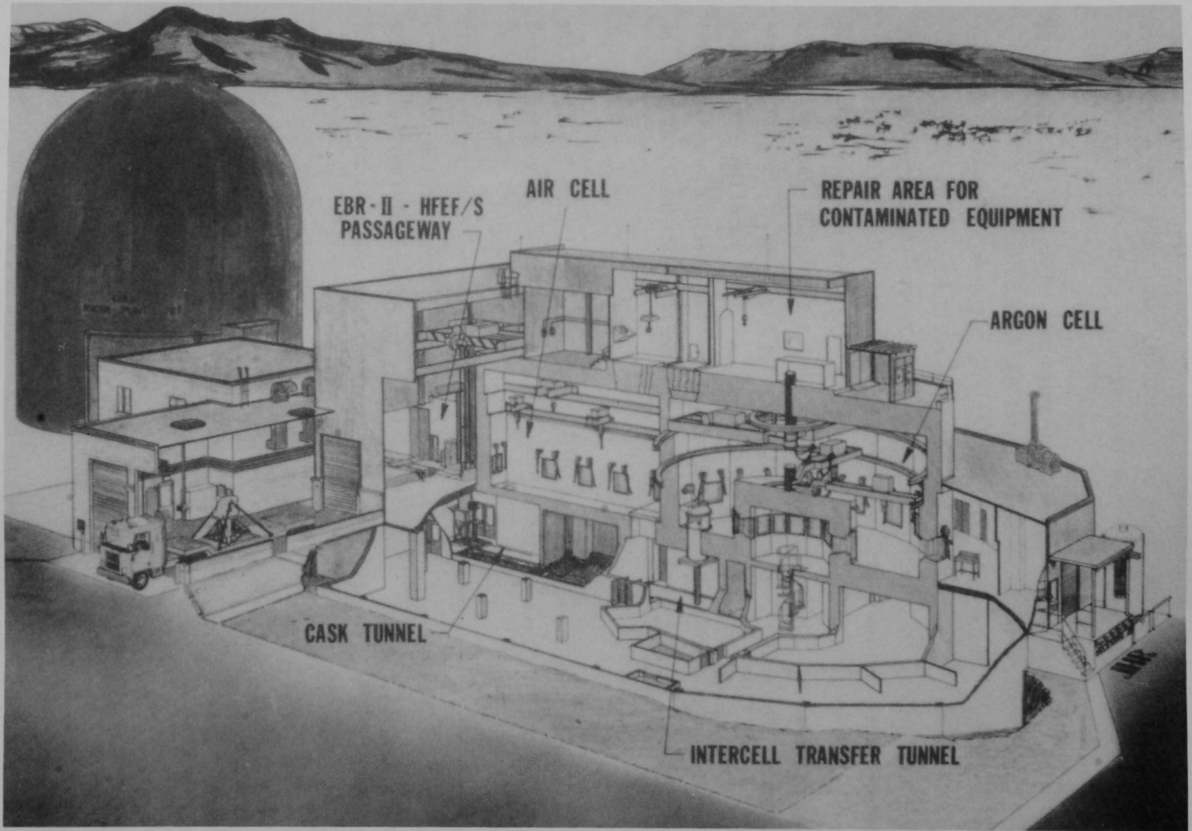

Fig. VI.1. Hot Fuel Examination Facility/South is provision of adequate facilities for repair of contaminated equipment. This is being done in the basement of the existing facility.

The in-cell equipment is being designed, to the extent possible, for in-situ repair. When this is not possible, modules or components (or in a few instances, entire pieces of equipment) will be brought to the new repair area for repair or disposal. The hot repair facility (HRF) will include provisions for remote transfer of equipment from either cell, remote decontamination, shielded glove wall and special-purpose glovebox access to equipment, direct access to equipment by personnel in protective clothing, a special pit area for crane trolley and electromechanical manipulator carriage repair, and the capability for bag-transfer of equipment and low-level contaminated waste into or out of the area (see Fig. VI.2).

Confinement improvements involve two basic forms. The first form is that of physical barriers and the second is air flow and/or filtration system improvements. The most significant physical barrier type of confinement improvement is sealing of utility penetrations and provision of sealed master/slave manipulators in the air atmosphere cell (for confinement the air cell currently relies on maintaining negative pressure with respect to the operating floor). The most significant flow and filtration improvement is provision of a safety-grade exhaust system to assure that there is no unfiltered release from the argon cell even in the very unlikely event of an accident or earthquake that causes a breach in the cell boundary.*

To provide needed emergency electrical power new safety-grade redundant diesel-powered electrical-generators (375 kW each) will be installed in a new seismic- and tornado-hardened building adjacent to HFEF/S. These generators will power the electrical loads in the facility which are important

---

*Even though seismic analysis early in the project lifetime established the basic integrity of the cell structures during a DBE, there are numerous extensions of the cell boundaries (e.g., the argon cell cooling ducts that extend into the subcells). Establishing seismic resistance for all these extensions is very difficult. For this reason, a limited breach is assumed, and a safety exhaust system is being installed to maintain confinement in spite of it.

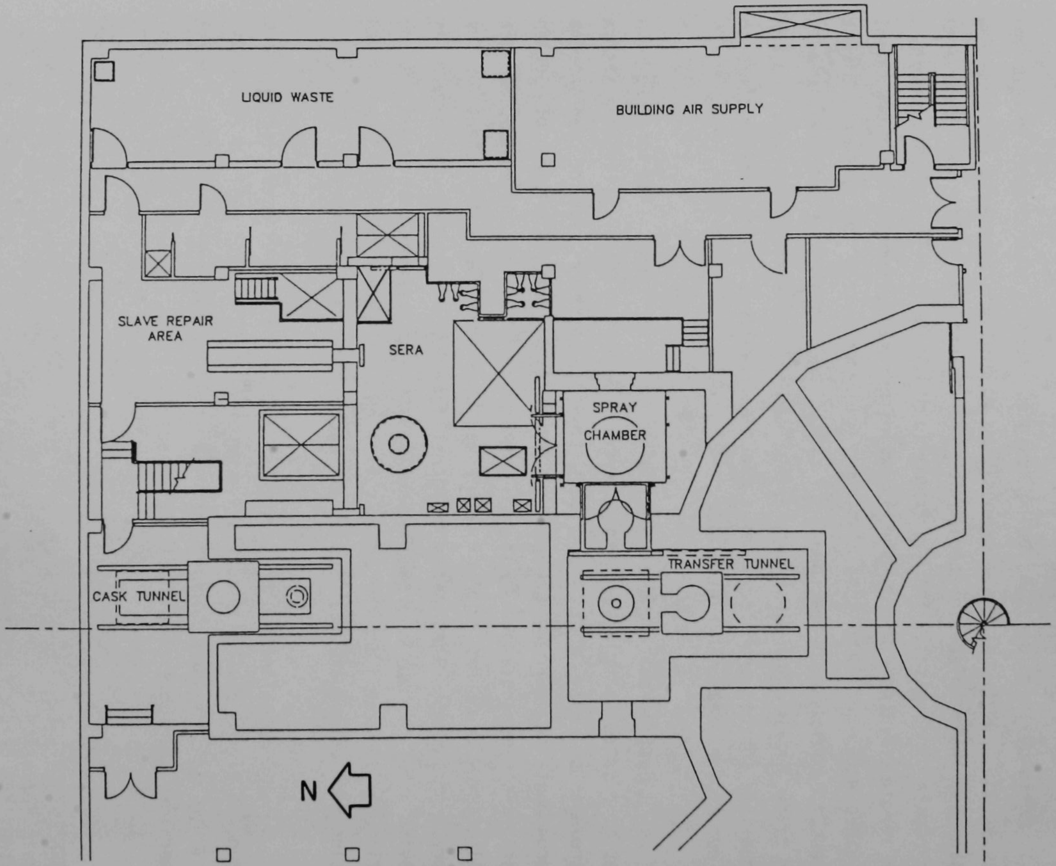

Fig. VI.2. Hot Repair Facility Plan View to safety. A battery system will also be provided to supply uninterruptable power to systems (controllers, sensors, monitors and alarms) which should not be without power even for the short time required for the diesel generators to start.

With this overview of the facility modification requirements in mind, the progress and status is summarized below.

To make room for the new hot repair facility now being constructed in the basement, an obsolete spray chamber and contaminated equipment repair area was thoroughly decontaminated and demolished. Demolition of obsolete mechanical systems in the basement and subcells was also completed, early in 1988. This included a large radioactive liquid waste tank that was removed and shipped to an on-site waste reduction facility.

All piping and ventilation ducts that interfered with construction of the HRF were relocated. A temporary steam supply was constructed so that contaminated asbestos insulation could be removed from the existing piping. Contaminated cask and transfer carts and rail systems were removed from the cask tunnel and transfer tunnel. Highly contaminated components from the argon gas purification system were removed to reduce the radiation background. In anticipation of extensive modifications, ventilation systems were modified so that the argon cell, transfer tunnel and air cell could be ventilated independently of each other, and atmospheric barriers were established to prevent cross-contamination between the areas.

Following this preparatory work a contractor specializing in facility decontamination was hired to clean the construction areas to the point where further work would not be severely hindered by radiological control measures and items for disposal (especially the soil to be excavated from below the basement floor) would be uncontaminated.

The cask tunnel was heavily contaminated because routine transfers into and out of the cell were made without the protection of bagged transfers, a technology implemented at the Hot Fuel Examination Facility-North, and one which is being installed as part of the modifications. The floor in this area was to be removed to increase head height so about 0.36 to 0.6 cm of the top surface of the concrete was chipped away (scabbled) using a special purpose machine. The walls of the cask tunnel were decontaminated using a system similar to a sand blaster but which used steel shot, continuously vacuumed it up, separated the concrete, recycled the shot and filtered the exhaust.

The transfer tunnel was the most highly contaminated area in the basement with hot spots reading up to 3000 mR beta/gamma and 500 mR gamma following the initial decontamination. After the equipment was removed, the floor was scabbled and the walls and ceiling abrasive-blasted to reduce the background levels for construction workers. The walls and ceiling were then finished, sealed, and painted to fix any residual contamination. The concrete floor which was to be removed to increase the handling height in the tunnel was sawed flush with walls using a wall saw and then cut into small sections for ease of removal.

To provide the vertical clearance necessary to construct the HRF, it was necessary to remove a significant portion of the basement floor in the northwest corner of HFEF/S and excavate down to a level approximately 5 m below the pre-existing floor level. In the original construction of HFEF/S, the basement floor was used to support several of the basement walls. Therefore, before the floor could be removed, bracing was installed to counteract the force of back-fill on those walls. Analysis of the support columns for the air cell* also indicated that removal of the floor required addition of horizontal reinforcing between the two middle columns. To provide this, pipes were driven under the air cell and tension rods were installed to tie the column on the north side to the column on the south side.

A number of holes were bored through the basement floor to allow soil sampling for contamination and to provide reliable information on the floor thickness. No evidence was found that contamination had migrated through cracks or construction joints into the soil below.

---

*The argon cell structure rests on a continuous cylindrical foundation wall. The air cell structure rests on six support columns, four of which can be seen on Fig. VI.2.

To minimize the potential for contamination of the soil during floor cutting, cuts were made only 90% of the way through the floor with the remainder fractured after cleanup of the water. After the concrete was removed, soil samples were taken, counted for radiation and analyzed for the presence of toxic materials. All analyses for toxic material were below allowable limits. When radioactive contamination was detected, the material was hand excavated until contamination free samples were obtained. Approximately 700 m^3 of soil and rock were removed from the basement with 90% being disposed of as uncontaminated.

Structural and architectural design of the hot repair facility complex was completed in April 1989, and fabrication of embedments to be placed in the new walls and floors was started immediately. Approximately 350 holes were core-bored in existing walls and columns for installation of rebar anchors to provide horizontal supports for new concrete walls. The construction contract was completed in September 1989 with the placement of 230 m^3 of concrete.

Modifications of the air atmosphere cell to improve contamination control required removal of all irradiated material and contaminated equipment. The cell was then decontaminated using a combination of remote and contact decontamination techniques. Present dose rates are 10 to 20 mR/hr beta-gamma. After the cell was decontaminated, the air cell cranes and electromechanical manipulators were refurbished and electrical wiring to the lights was replaced.

New floor shielding plugs were installed in the air cell to allow transfers between the air cell and shielding casks to be conducted through plastic sleeves for contamination control (the bagged-transfer technique mentioned above). To replace the unsealed master slaves with the sealed variety dual 0.46-m diameter holes were drilled through the shield wall at eight work stations, and larger seal tubes were installed. Utility penetrations are being either sealed closed or modified so that the penetration plug will provide an atmosphere seal.

A constant air flow will be maintained through the air cell by the ventilation system. However, because the master slave and utility penetrations are being sealed, all inlet air will be drawn into the cell through HEPA filters. This will prevent the escape of contamination if an abnormal condition creates a pressure-driven air flow reversal.

The argon cell was decommissioned in 1978, and a decontamination effort conducted. All accessible surfaces of the argon cell were remotely vacuumed and remotely washed down with a foam-type decontamination agent. After the remote decontamination operation, personnel entered the cell to vacuum inaccessible areas and wash the cell using high pressure water. Approximately 30 Ci of water-soluble ^{137}Cs and 32 Ci of other miscellaneous fission products were removed in the process. After that effort was completed in 1981, the argon cell was closed and not used subsequently.

In January 1989 argon cell radiation levels were measured at 1000 to 2000 mR beta and 100 to 200 mR gamma with hot spots to 30,000 mR beta and 5000 mR gamma. Analysis indicated that the zinc coated floor was still highly contaminated with ^{137}Cs and ^{90}Sr.

Decontamination tests were conducted on surrogate samples of zinc coated steel plates using a warm (49°C) dilute solution of nitric and phosphoric acid with dissolved non-radioactive potassium and strontium to act as hold-back agents to prevent re-adsorption of the dissolved fission products. After the successful laboratory tests and decontamination of one trapezoidal section of the argon cell floor, the entire cell floor was cleaned using the technique. Approximately 4000 ℓ of radioactive liquid waste were generated. Most of the fission products were precipitated from this solution and 11 barrels of waste were solidified for disposal as solid waste. The liquid remaining was evaporated by standard techniques. The beta levels were reduced by a factor of 10 and the gamma levels were reduced by a factor of approximately 2 with the result that beta and gamma levels are now equally limiting on exposure time.

After review of the preliminary safety analysis report, the DOE required the argon cell exhaust system and its emergency power supply to be designed and constructed to safety class standards. Therefore, the design of the emergency power system was modified to include redundant safety-class diesel generators and power distribution components for the argon cell exhaust and stack monitoring systems. Emergency power to all other non-safety class equipment will be supplied by the same diesel generators, but the feeders will be buffered by safety-class circuit breakers to protect against ground faults in non-safety-class portions of the emergency power distribution system. The diesel generators and argon cell exhaust system will be located in a new seismically hardened building (about 15 m square). Construction of a tunnel to connect HFEF/S to the new building has begun.

2. Status of Process Equipment Design/Fabrication

Most of the process equipment required for the demonstration is currently in final design or in fabrication and checkout. All process equipment is scheduled for installation by October 1990, the same time that facility modifications are scheduled for completion. Figure VI.3 shows the in-cell arrangement of this equipment in the two fuel cycle facility process cells. The discussion below follows the process from the first of the refining and refabrication steps to assembly of the newly fabricated elements into subassembly hardware for reactor use. This latter operation uses the same equipment as is used to disassemble the spent fuel prior to refining.

The first major item of equipment in reprocessing is the fuel element chopper which renders the intact fuel elements suitable for electrorefining by chopping them into short segments to expose the fuel and remove unwanted scrap such as the spacer wire, end caps, and plenum sections from the process flow stream. Fuel elements are received at the chopper 35-40 at a time in a cylindrical magazine and individual elements are dispensed through a slot in the side. They are grasped by a motorized collet and advanced along the transport mechanism into a set of cutting dies mounted in a solenoid-operated punch press. The press is activated and the bottom fitting is chopped off, severing the lower attachment of the spacer wire. The fitting falls through a hole in the lower platen of the press into a container mounted on a motor-driven turntable located in the hood below the press. A pair of winding dies then tightly coils the wire wrap around the upper end of the

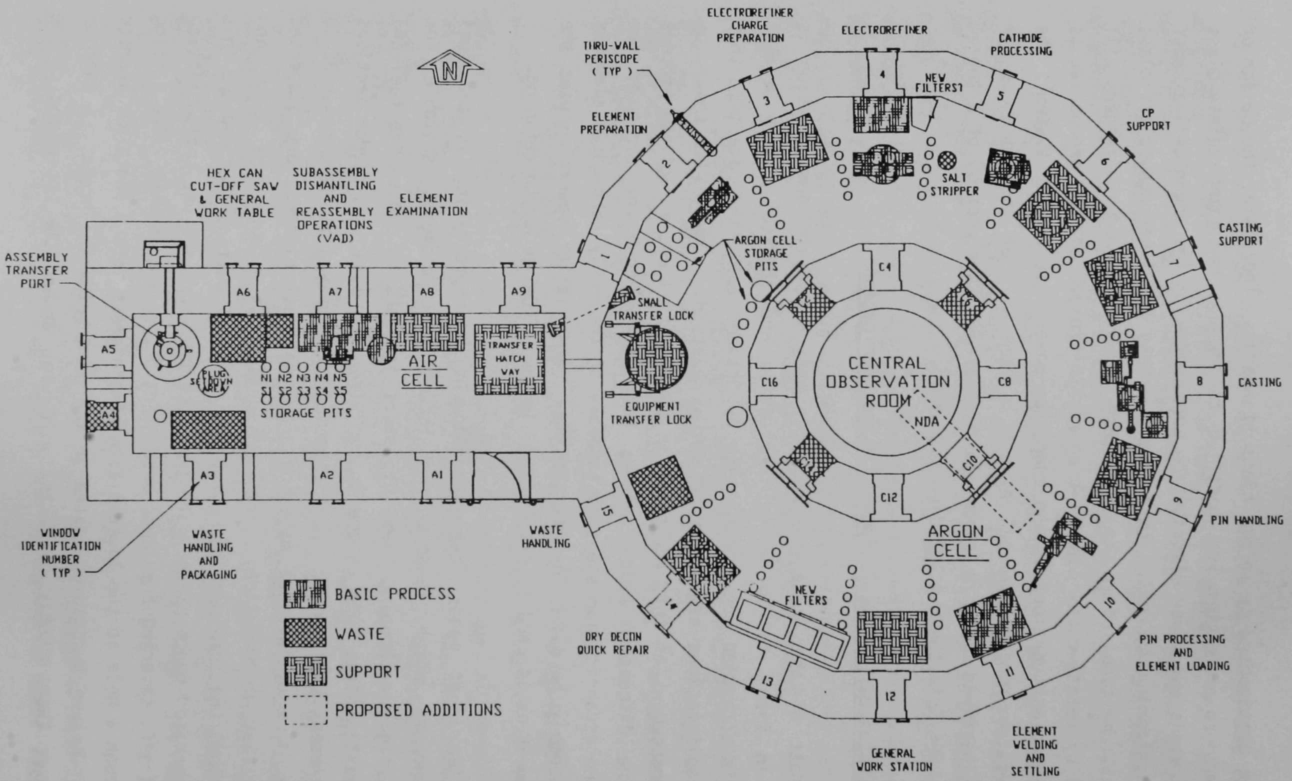

Fig. VI.3. Air and Argon Cell Proposed Equipment Locations plenum section. The element is then advanced into the cutting dies. Short segments are chopped off and allowed to fall into a container on the turntable inside the hood. When chopping of the active fuel length of the element is complete, the plenum section of the element, with the wire-wrap coiled around it, is released to fall into a collector tray. The next element is dispensed from the magazine by rotating the element holder inside the magazine to the next position, and the process is repeated.

When a sufficient number of segments have been collected in containers inside the hood, the operation is interrupted, and the containers are removed for transfer to the electrorefiner staging area for makeup of anode assemblies. Samples for chemical analysis may be collected at any point in the chopping operation by rotating the turntable in the hood to a different position, at which a sample container is located.

The hood prevents dispersal of large amounts of particulate material from the chopping operation into the cell. A small pump draws cell atmosphere into the hood through the small opening afforded by the cutting dies and the flow is filtered before discharge back into the cell. Since the cell atmosphere contains enough oxygen and moisture to oxidize and/or hydrolyze the bond sodium in the fuel segments, thus eventually introducing oxygen into the electrorefiner, the segment containers are opened only while being filled.

To date, all major assemblies except the turntable and the element magazine operating mechanism have been fabricated either as prototypes or as final parts. The two remaining assemblies are in final design.

Electrorefining operations will occupy two workstations in the argon cell: the electrorefiner station, and a staging station, The electrorefiner (Fig. VI.4) is a 102-cm-diameter by 99-cm-deep cylindrical vessel containing the molten cadmium and electrolyte salts. A flat top cover has four large ports for electrodes and several smaller ports for other components. The vessel sits in a support stand that also supports the heaters for the vessel. The four legs contain leveling jackscrews and vertical support posts upon which are mounted the electrode assemblies via motor-driven elevating and rotating assemblies. The elevating and rotating assemblies raise and rotate

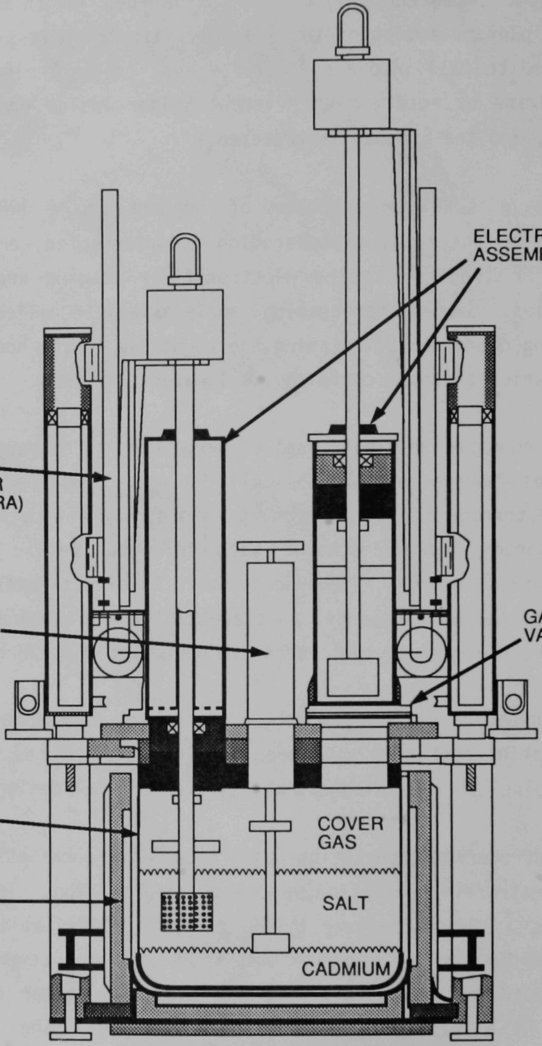

Fig. VI.4. Electrorefiner

the electrode assemblies over the lip of the vessel, and lower them through the ports in the top cover.

The highly deliquescent electrolyte must be provided with a higher purity argon cover gas to prevent oxygen from slowly combining with the heavy metal in the electrorefiner. In order to prevent excessive degradation of cover gas purity during electrode insertion and withdrawal operations, each electrode is kept enclosed in a bottom-loading container. This container is mounted on a large diameter slide valve attached to the electrorefiner cover, and the electrode is lowered through the throat of the valve. While the system is not pressure tight in an absolute sense, it does prevent rapid interchange of the cell atmosphere and the electrorefiner cover gas.

Electrodes are made up and disassembled at the staging work station. At this station, anodic dissolution baskets full of chopped fuel are received from the element chopper and placed in an assembly fixture. The containers are opened, and the baskets are attached to an electrode shaft and withdrawn into the electrode container for transport to the electrorefiner. Uranium-zirconium cathode rods are received from the fuel pin processor,* attached to an electrode shaft and withdrawn into an electrode assembly container for transfer to the electrorefiner. The disassembly procedure is much the same, in reverse order. The cathode deposit is removed and placed in a container for transfer to the cathode processor. Empty anode baskets are removed for recycle back to the element chopper.

All major functional requirements of the electrorefiner and its staging station have been determined. Preliminary designs are in hand for most of the subsystems and final engineering bid packages have been prepared for two major items, the electrorefiner vessel and the elevator/rotator assemblies. Detail drawings for the electrical brush/slip-ring assemblies have been completed, and the support stand is in final design. A prototype

---

*The cathode mandrels for deposition of refined uranium will be made from uranium-zirconium rods cast in the injection casting furnace. This provides a means for internal recycle of casting scrap and eliminates the requirement for removal of the cathode deposit from the mandrels.

slide valve has been manufactured and is being prepared for testing. A plywood and metal-frame mockup has been built to ensure dimensional fitups and clearances.

The cathode processor is designed to remove residual electrolyte and cadmium from both uranium and uranium/plutonium cathodes from the electrorefiner and to produce fuel ingots satisfactory for use in the fuel casting operations. The cathode processor consists of an inductively heated furnace region and a condenser region. Cadmium metal and salts are vaporized in the furnace, and flow as vapor into the condenser where they are condensed and collected in a receiver crucible. The fuel remains in the process crucible, is consolidated into ingots, and continues on through the fuel cycle. Details of the cathode processor internals are illustrated in Fig. VI.5. The furnace region has been designed to operate at temperatures up to 1375°C. The furnace is separated from the condenser by a transition zone, which is designed to withstand the necessary large temperature differential. Both crucibles are accessed by lowering the interior components of the cathode processor from the operation position and moving them horizontally to the service position in front of the adjacent workstation.

Supporting research efforts have provided verification of the cathode processor concept and continue to provide necessary design information. Conceptual and preliminary design reviews have been completed. Final design is nearly complete. The final design review process began in November 1989.

The reprocessed fuel ingots from the cathode processor are fabricated into new fuel pins by injection casting in an inductively heated furnace. (See Fig. VI.6.) The fuel ingots are combined with the desired makeup material (zirconium and enriched uranium or plutonium alloy) and recycle material (fuel pin casting heels and recycle fuel pin pieces) in a graphite crucible. The crucible is then placed inside the induction coil of the furnace. All normal handling and loading operations are conducted through a single 25-cm-diameter quick-opening flange at the top of the furnace pressure vessel. More extensive disassembly for cleanout or repair is also possible. To minimize the loss of fissile material by oxidation, the furnace

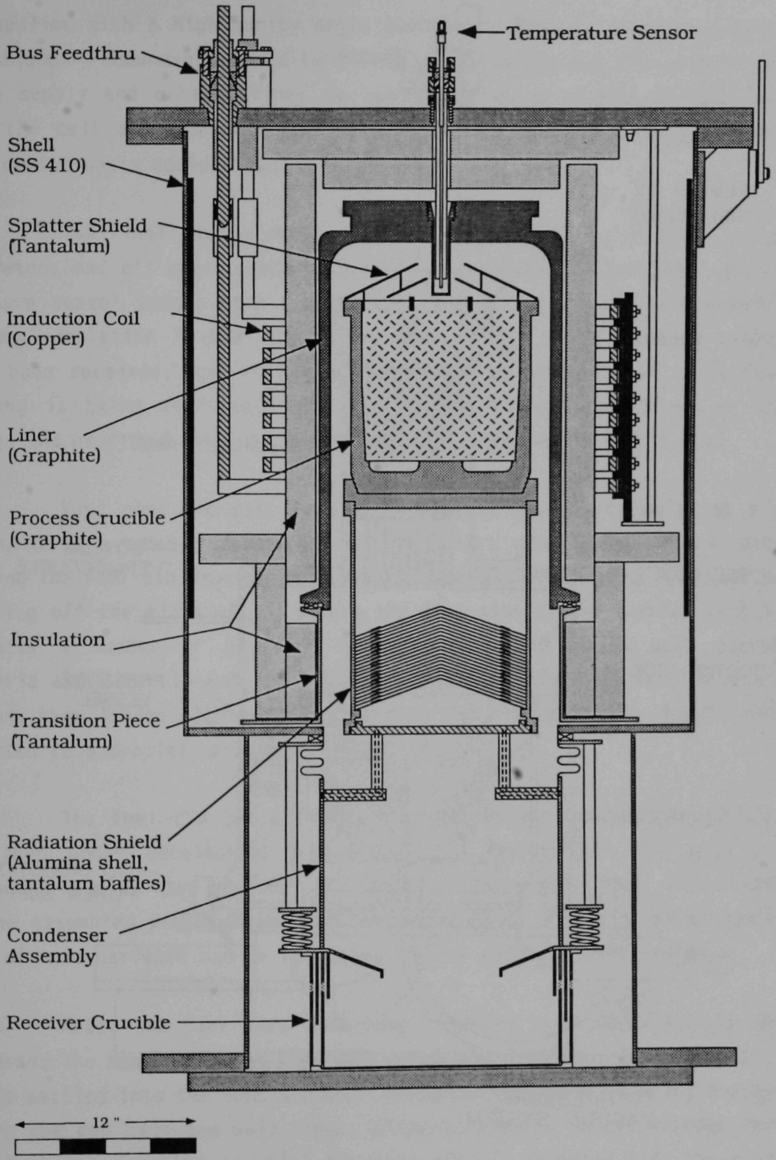

Fig. VI.5. Cathode Processor

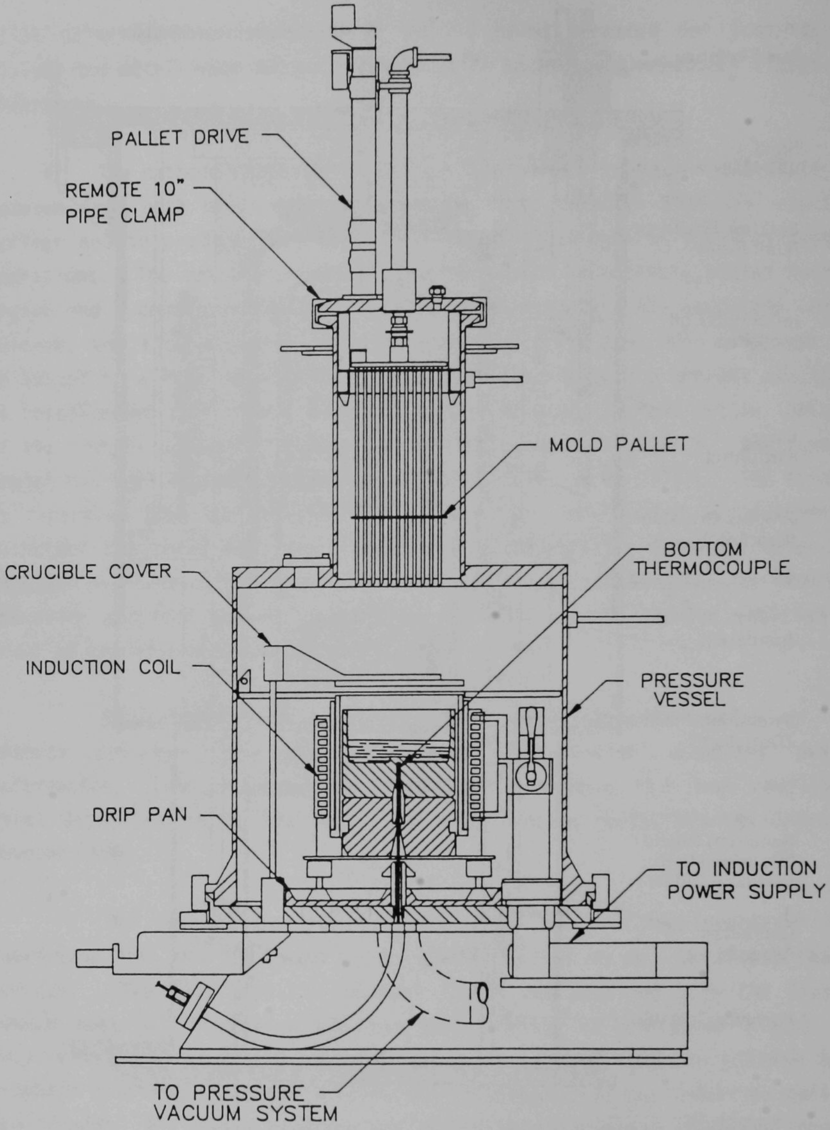

Fig. VI.6. Injection Casting Furnace

is supplied with a high purity argon atmosphere for all elevated temperature operations. Redundant, normally closed isolation valves are present on all argon supply and exhaust lines to assure isolation of the furnace contents from the cell atmosphere in the event of a loss of cell integrity resulting from design basis accidents.

The final design review process for the casting furnace is nearly completed, and all major components are in fabrication. The power supply and pressure vessel orders have been placed, and the induction coil assembly is nearing completion in the fabrication shop. Most control system components have been received, and instrumentation will be ordered soon. Development testing is being conducted with an existing furnace, which is of similar design and used routinely for fabrication of unirradiated EBR-II fuel.

Fuel pins are cast into approximately 150 quartz molds at a time. The molds are removed from the casting pallet and loaded into a magazine feeding the fuel pin processing machine. This machine demolds the fuel pin by breaking off the glass molds, shears the fuel pins to the correct length, and conducts a number of physical inspections. Pins which meet acceptance criteria are directly and automatically inserted into new cladding which has already been loaded with sodium to provide the thermal bond. Reject pins are diverted to a special carrier for recycle.

The fuel pin processor is a complex electromechanical device that has been under development since early in the project and most of its component modules have now been fabricated in prototype form. Initial testing of the assembled prototype modules has gone well, and it is anticipated that most of this hardware can be installed in-cell without modification.

After the fuel pins have been inserted in the cladding by the pin processor the top end cap is inserted and welded into the jacket, and the fuel pin is settled into the bond sodium. Automated equipment is being designed to insert the end caps and weld them. Elements will be welded without removing them from the magazine in which the fuel pin was inserted into the cladding. The fuel pin will also be settled down through the sodium by simple heating before removal from this magazine.

Following welding and settling, the element ends and the magazine are decontaminated and then transferred into the air cell. The magazine is unloaded and the elements are inspected on a new automated inspection system. The elements are then installed into reactor subassembly hardware on the vertical assembler/dismantler. This is an existing machine in the air cell that has been extensively refurbished over the past two years, and the last modifications are now in fabrication and qualification. This machine is used for assembly of newly fabricated fuel elements into subassembly hardware for transfer to EBR-II and for disassembly of the spent fuel subassemblies after receipt from EBR-II.

Additional process support equipment is also being designed, fabricated and/or checked out. Examples include temporary storage racks, television viewing systems and in-cell decontamination equipment.

3. Waste Handling and Processing

A number of radioactive waste streams will be generated during the fuel cycle demonstration. Because not all process parameters have been established, precise volumes and radioactivity levels of these waste streams are not available, but broad waste categories and their characteristics can be described. This section provides a description of the waste streams and outlines handling and storage strategies. An important aspect of the fuel cycle program is the development and demonstration of waste processing methods. Process development is ongoing to permit demonstration of actinide recycle and complete removal of transuranics from the electrolyte waste and perhaps other wastes.

Important considerations for waste are transuranic content (TRU), whether they qualify as "hazardous" because of their chemical composition (cadmium content for example), curie content, the radiation dose rate at the container surface, the heat production rate, the fissile mass and the presence of elemental sodium.

Without special treatment to remove transuranics, salt wastes will be TRU and will have very high activity levels due to the presence of alkali and alkali-earth fission products, mostly Cs and Sr. Treatment to remove transuranics to sufficiently low levels to produce a non-TRU waste is planned.

Noble metal fission products accumulate in the cadmium pool of the electrorefiner. When the electrorefiner salt is "stripped" of its uranium or plutonium, most of the rare earth fission products are also transferred to the cadmium. Presently, the extent of treatment of the cadmium wastes has not been decided. Removal of the transuranics is under consideration and the cadmium will be recycled to the extent practical. Final disposition will be determined by the results of the processing applied. Other metallic wastes include cladding hulls and used anode baskets.

Radioactive liquids are generated during spent fuel subassembly washdown prior to transfer in-cell and by equipment or facility decontamination. The wash liquids are collected in tanks and evaporated to produce a solid waste product for disposal.

Miscellaneous wastes include contact handled wastes (which generally consist of contaminated equipment and disposable waste items including gloves, filters, shoe covers, tools, light structural materials, and discarded equipment); hex cans and top and bottom hardware from the fuel subassemblies; the upper ends of the fuel elements; and ceramic wastes which are mostly used crucibles and broken glass molds from the pin casting process. Some of these will be disposed of using existing approved methods and/or new improved processes and packaging methods that are being developed. These processes will be demonstrated as appropriate.

Because of low generation rates and extremely low radiotoxicity, it is planned that gaseous wastes from pyroprocessing will, at least initially, be released to the atmosphere via the stack. However, in order to demonstrate processing representative of future commercial practice, a demonstration fission gas recovery system involving cryogenic condensation of krypton will be added later.

4. Process Control and Accountability

A preliminary design of the process control and accountability systems has established the overall functional requirements and design criteria. These design criteria have been divided into four different areas: logic controllers, operator control stations, central data logging and mass tracking. An overview of the information which will be shared among the different areas and the general system configuration is shown in Fig. VI.7. The overall system can be characterized as a distributed control system where different tasks are done on separate central processing units and the individual central processing units are interconnected with data networks.

The logic controllers are the primary interface between process equipment and the overall control system. The logic controllers have two major components: Programmable logic controllers (PLCs) and input/output modules. All instrumentation and control devices are connected to the input/output modules, and control algorithms, signal conditioning and operational interlocks reside there. For reliability and flexibility, there will be nine programmable logic controllers one for each major piece of equipment. The control algorithms will use ladder logic programming. Procurement has been completed on four of the programmable logic controllers and programming has been started for two of them.

The operating technicians will control and monitor all important process parameters through the operator control station (OCS). All normal control functions such as turning equipment on or off, changing setpoints, initiating and terminating control sequences, acknowledging alarms, and monitoring data streams will be done through the operator control stations. The operator control stations will also provide a means of monitoring trends in process variables, and will create operator logs, alarm logs and event logs. Dynamic color graphics will display the operating information in an easy to read format. Different levels of access will be provided to protect the integrity of the data base and allow operators and supervisors to only change and control data and machines which they are qualified and authorized to operate. Communications between the operators and the mass tracking system will also occur through the operator control stations. Each work station in

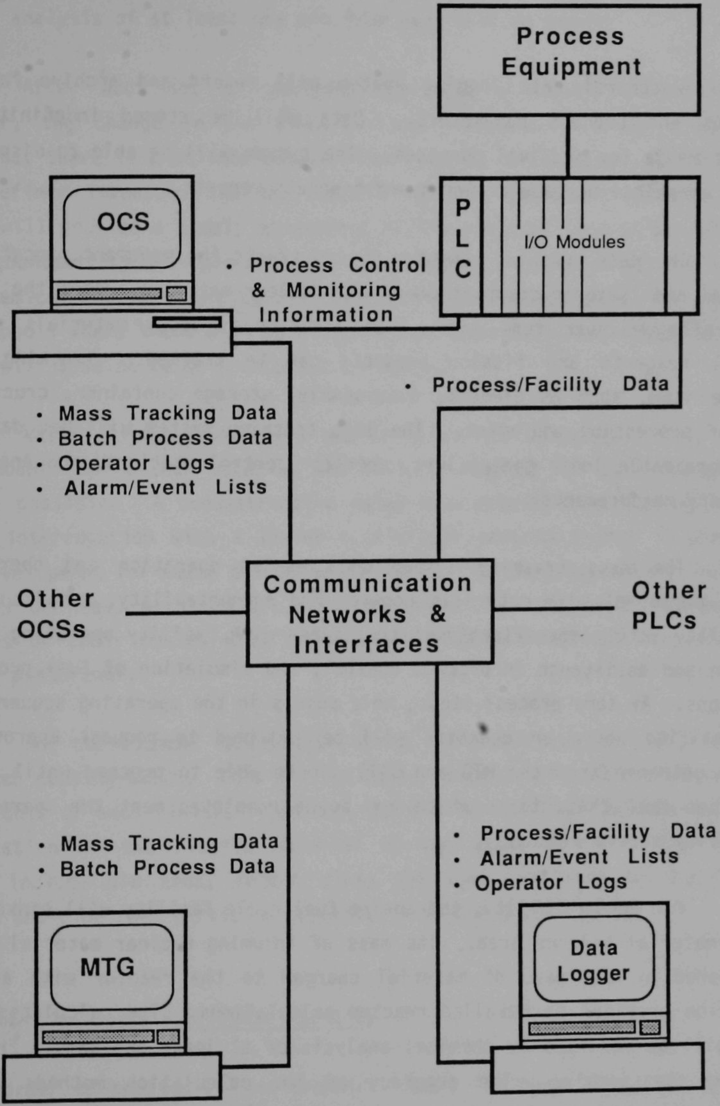

Fig. VI.7. Preliminary Control System Layout the facility will have the capability of accommodating an operator control station.

A central data logging system will record and archive facility, equipment and process parameters. Data will be stored indefinitely on magnetic media for archival purposes. The system will be able to display the data in graphical or tabular forms and generate reports.

The mass tracking computer system tracks the movement, location and elemental and isotopic composition of all nuclear material inside the air and argon cells in near real time. In addition, process materials such as chemical reagents and fission products can be tracked. Tracking is by discrete item, such as element, subassembly, storage container, crucible or piece of processing equipment. The mass tracking system will use data from the programmable logic controllers, operator control stations, and Analytical Laboratory measurements.

The mass tracking system will assist operation and operations-support personnel with materials control and accountability; compliance with criticality safety specifications; compliance with facility operating limits; guidance and assistance in process control; and simulation of fuel processing operations. At some process steps, hold points in the operating sequence will be identified where an operator will be required to request approval and receive guidance from the MTG and will not be able to proceed until the MTG determines that the actions which are to be completed meet the operating or criticality safety limits.

For accountability, the entire fuel cycle facility will constitute a single material balance area. The mass of incoming nuclear material will be established by the mass of material charged to the reactor with a burnup correction provided by detailed reactor calculations. The calculated burnup value will be verified by chemical analysis of at least one sample from each incoming subassembly. The accuracy of the calculation methods will be verified in separate experiments with detailed sampling and analysis of representative subassemblies. The nuclear material mass of fabricated elements will be established by weighing each newly fabricated fuel pin and by chemical analysis of at least one pin from each casting batch.

After each set of cathodes has been processed in the cathode processor, the change in the electrorefiner inventory will be checked to assure that there is a balance between the input to the chopper, the change in electrorefiner inventory and the output from the cathode processor. This balance will provide a timely assessment of the chemical separation steps for both accountability and process control purposes. As part of the balance data, chemical analysis samples will be taken from the electrorefiner salt and cadmium pools where there will be a significant amount of in-process material. Samples will also be taken from product ingots.

Waste streams, including quartz molds and cladding hulls, contain small amounts of nuclear material and will be sampled for chemical analysis wherever possible. A nondestructive assay measurement method using pulsed-neutron interrogation with a 14-MeV accelerator neutron source is presently under development for waste stream measurements. Holdup, especially insoluble particles of heavy metal oxides, will be present in some waste streams and estimates of their masses will be obtained from calculations normalized by periodic measurement.

For the element fabrication steps, a material balance will be made after each casting batch. This will be based on chemical analysis of one fuel pin, weights of each finished fuel pin, weights of all recycle material and a determination of the fissile material in the waste stream. The recycle streams include pin ends, reject pins, the heel remaining in the casting crucible and fine fuel particles separated from the broken molds.

B. Commercial-Scale Fuel Cycle Facility

In order to provide a firm technical basis for quantifying the IFR fuel cycle economics, a detailed conceptual design of a commercial-scale IFR fuel cycle facility was developed in 1985 in conjunction with the industrial innovative LMR design projects: PRISM, designed by General Electric, and

SAFR, designed by Rockwell International. The throughput capability assumed for the design was sufficient to support a 1200-1400 MWe generating capacity, equivalent to nine PRISM reactor modules or four SAFR modules. Reprocessing and refabrication of all the fuel and blanket materials needed for this generating capacity was assumed.

The basic design goals for development of the concept were to provide a high level of inherent safety; achieve a low cost design, with high reliability, operability and maintainability of all facility systems particularly the in-cell process equipment and handling systems; permit no radiological release under normal operating conditions; maintain a high degree of diversion resistance throughout the entire fuel cycle; and meet licensability requirements. The fuel cycle facility was to be designed for colocation with the reactors and therefore, some sharing of general site services and facilities was considered acceptable providing it did not compromise any of the basic design goals. Location of such a facility on a separate site is feasible with the major differences being in the transportation requirements and the addition of any services shared with the reactor when co-located.

As illustrated in Fig. VI.8, the fuel cycle facility concept is very compact: 29.3 m x 32 m, with a height of 13.4 m. The key part of the facility concept is the inert-atmosphere process cell, which is only 164 m^2 in area and 4.3 m in height. Overhead handling systems have been eliminated through the use of both process and repair robots. The process cell configuration was developed with robots on transporters traveling on floor-mounted tracks. The same configuration could be equally well-serviced with gantry-mounted robots although this would increase the cell height requirements. The robots are expected to be an adaptation of commercial systems used in conjunction with automated process equipment in preprogrammed mode for routine process operations and manual control mode for maintenance and non-routine tasks. A separate special purpose heavy duty repair robot was also included in the concept.

The design of the fuel cycle facility is intended to meet all codes and standards for a commercial reactor plutonium-fuel reprocessing facility. The

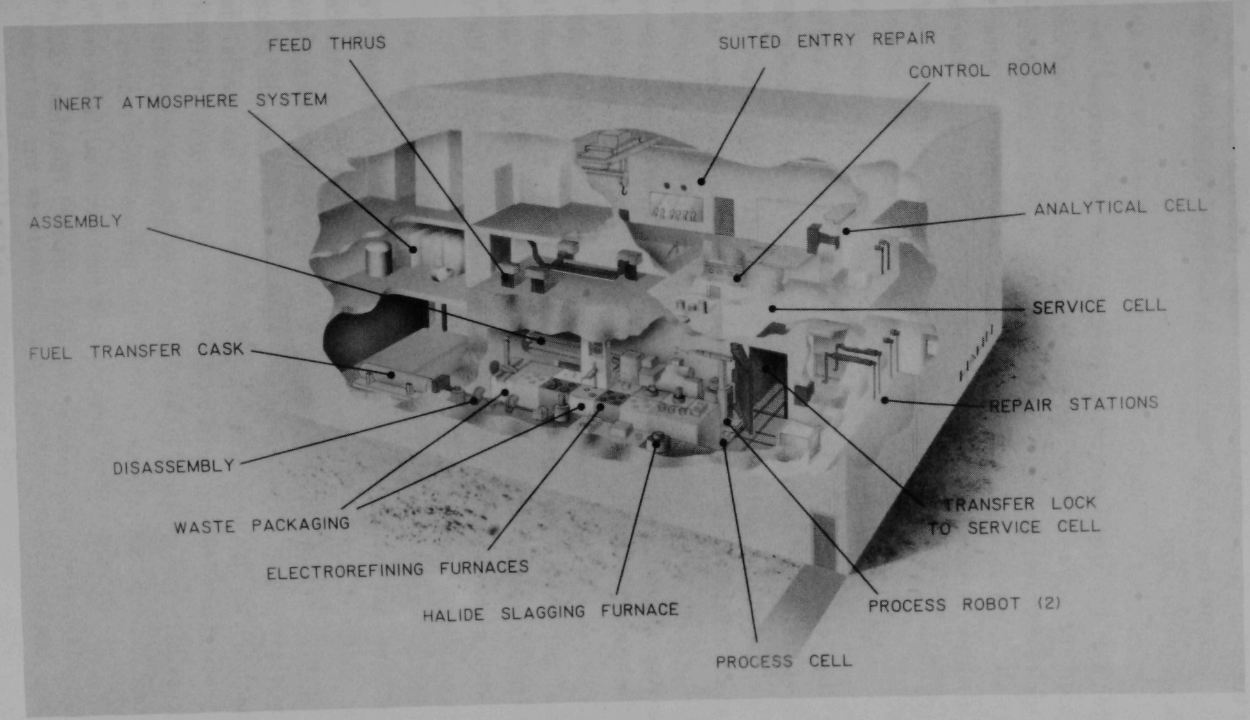

Fig. VI.8. Commercial-scale IFR Fuel Cycle Facility
(ANL Neg. No. 900-85-93K Rev. 2)

fuel cycle building is a three-level reinforced concrete structure. The ground-level floor is the top surface of a 0.9-m-thick foundation slab that supports the entire building.

All materials enter and leave the building through one location, the cask receiving room. Rail tracks enter the building at this location and connect to the reactor building(s) and waste building. Cask handling, transfers, and process cell wall transfer ports are horizontal. All personnel enter and leave the building through a security access-control location. Emergency exits are provided at appropriate locations to meet industrial safety requirements.

In the fuel cycle building there are three hot cells which would be operated and maintained by remote means only. These are the process cell, the service cell, and the analytical cell. The largest is the steel-lined, gas-tight, argon atmosphere process cell which has inside dimensions 16.8 m long, 9.8 m wide, and 4.3 m high. Two walls and the ceiling are of 1.8 m thick 2.4 density concrete, and the operating corridor and cask transfer room walls are 1.2 m thick 3.5 density concrete. On the ground-level adjoining the process cell is an air atmosphere service cell where equipment may be decontaminated and remotely repaired. An analytical cell is on the second-level and is separated into four sections. There are two window workstations with master-slave manipulators in the process cell, two in the service cell, and four in the analytical cell.

A 7.3 m high suited-entry repair room is on the second-level, and decontaminated equipment may be transferred to the room from the service cell for further repair or preparation for disposal. The room has a shielded glove wall and an adjacent master slave manipulator repair room. Above the process cell on the second-level is the process utilities room which has special gas-tight floor penetrations to the cell. All utilities and control circuits enter the process cell through these penetrations. The process utilities room is the interface between the process cell and the ground-level process- and building-systems control room. Other areas in the fuel cycle building are for facility support equipment and special process support functions such as fission gas collection, cell atmosphere purification, radioactive liquid waste processing, and process materials storage and preparation.

The process- and building-systems control room is the "heart" of the fuel cycle building. Computer automated control is used extensively for all activities within the cells and the building. In the room are the computer operator consoles and a high-security stand-alone safeguards terminal and mini-computer, which is assigned to monitor the process and provide verifiable accounting for all special nuclear materials in process or storage.

In the initial facility concept, the capability for waste handling and natural-convection cooled temporary storage was included as a separate building. With more recent developments, it is expected that concept refinement studies would show that a common building would provide advantages including cost reduction.

The waste building is located on the fuel cycle facility site near the fuel cycle building. The waste building provides: (1) interim storage and final canister encapsulation of the high level waste, (2) secondary packaging and off-site shipment of intermediate level waste, and (3) interim storage of fission-gas cylinders. The waste building has storage vaults, shielded cells for various handling and preparation activities, and a cask loading area. The building is 40.5 m long, 17.1 m wide and 9.8 m high.

The fuel cycle facility is very small compared to a conventional PUREX based fuel cycle facility of the same capacity. Therefore, a large relative capital cost reduction is expected for the IFR fuel cycle facility, in comparison with the PUREX facility. The preliminary estimate indicates that the capital costs of this IFR fuel cycle facility would be about $75 million. This includes construction of the buildings, provision of engineering and construction services during construction, and the procurement and installation of equipment for reprocessing, fabrication, waste packaging, and interim storage. The annual operating and maintenance cost is estimated at only $14 million/yr, excluding the cost associated with assembly hardware supplies. The low capital cost of the fuel cycle facility, combined with a low operating and maintenance cost, promises a very competitive fuel cycle cost even for a small-scale deployment of the IFR fuel cycle.

Reference for Section VI

1. C. Stevenson, The EBR-II Fuel Cycle Story, American Nuclear Society (1987).

VII. LIST OF PUBLICATIONS

The technical papers on the IFR Program activities, which have been published through the end of FY 1989, are listed below. The publications are categorized into the following subject areas: IFR Concept, Metal Fuel Performance, Pyroprocessing, Safety, Neutronics and Core Design, and Fuel Cycle Demonstration.

IFR Concept

1. Y. I. Chang, "The Integral Fast Reactor," Nucl. Tech., 88, 129 (November 1989).
2. Y. I. Chang, M. J. Lineberry, L. Burris, and L. C. Walters, "Integral Fast Reactor Shows Its Mettle," Nucl. Eng. Intl., 32, 23 (November 1987).
3. C. E. Till, "Advanced Reactor Development," Technical Note--Ann. Nucl. Energy, 16(6), 301 (1989).
4. C. E. Till and Y. I. Chang, " Evolution of the Liquid Metal Reactor: The Integral Fast Reactor (IFR) Concept," American Power Conference, 51, 688 (April 1989).
5. C. E. Till and Y. I. Chang, "The Integral Fast Reactor," Advances in Nuclear Science and Technology, Plenum Publishing Corporation, 20, 127 (1988).
6. C. E. Till and Y. I. Chang, "The Integral Fast Reactor Concept," American Power Conference, 48, 688 (April 1986).

Metal Fuel Performance

1. M. C. Billone, Y. Y. Liu, E. E. Gruber, T. H. Hughes, and J. M. Kramer, "Status of Fuel Element Modeling Codes for Metallic Fuels," Proc. of the Intl. Conf. on Reliable Fuels for Liquid Metal Reactors, p. 5-77, Tucson, AZ (1986).
2. L. K. Chang, J. F. Koenig, and D. L. Porter, "Whole-Core Damage Analysis of EBR-II Driver Fuel Following SHRT Program," Nucl. Eng. and Design, 101, 67 (1987).
3. D. C. Crawford, "An Investigation into the Use of Untempered End Plug Welds on HT9-clad Fuel Elements in the Integral Fast Reactor," M.S. Thesis, University of Washington (1986).

Metal Fuel Performance (Contd.)

4. P. G. Happoldt, "Application of an Atomic Mobility Model for Intrinsic Diffusion in Ternary Alloys," M.S. Thesis, Purdue Univ. (May 1988).

5. G. L. Hofman, A. L. Hins, D. L. Porter, L. Leibowitz, and E. L. Wood, "Chemical Interaction of Metallic Fuel with Austenitic and Ferritic Stainless-steel Cladding," Proc. of the Intl. Conf. on Reliable Fuels for Liquid Metal Reactors, pp. 4-121 to 4-131, Tucson, AZ (1986).

6. G. L. Hofman, R. G. Pahl, C. E. Lahm, and D. L. Porter, "Swelling Behavior of U-Pu-Zr-Fuel to High Burnup," Symp. on Irradiation-Enhanced Materials Science, TMS Fall Meeting, Chicago, IL, in press, Met. Trans. A., (September 25-29, 1988).

7. D. D. Keiser, "Fuel/Cladding Chemical Interaction Effects on the Mechanical Properties of Stainless Steel Cladding," M.S. Thesis, Univ. of Idaho (February 1988).

8. C. E. Lahm, "Determination of Temperature and Phase Distributions in Irradiated U-Pu-Zr Fuel," M.S. Thesis, Univ. of Idaho (February 1988).

9. C. E. Lahm, J. F. Koenig, P. R. Betten, J. H. Bottcher, W. K. Lehto, and B. R. Seidel, "EBR-II Driver Fuel Qualification for Loss-of-Flow and Loss-of-Heat-Sink Tests Without Scram," Nucl. Eng. and Design, 101, 25 (1987).

10. L. Leibowitz and R. A. Blomquist, "Thermoconductivity and Thermal Expansion of Stainless Steels D9 and HT9," Intl. J. Thermophysics, 9, 873 (1988).

11. L. Leibowitz, R. A. Blomquist, and A. D. Pelton, "Thermodynamics of the Uranium-Zirconium System," J. Nucl. Mat., 167, 76 (1989).

12. L. Leibowitz, E. Veleckis, R. A. Blomquist, and A. D. Pelton, "Solidus and Liquidus Temperatures in the Uranium-Plutonium-Zirconium System," J. Nucl. Mater., 154 (1988).

13. R. G. Pahl, C. E. Lahm, D. L. Porter, G. L. Batte', and G. L. Hofman, "Irradiation Performance of Metallic Fuels," Trans. Am. Nucl. Soc., 60, 304, San Francisco, CA (November 26-30, 1989).

14. R. G. Pahl, C. E. Lahm, D. L. Porter, and G. L. Hofman, "Experimental Studies of U-Pu-Zr Fast Reactor Fuel Pins in EBR-II," Symp. on Irradiation-Enhanced Materials Science, TMS Fall Meeting, Chicago, IL, in press, Met. Trans. A., (September 25-29, 1988).

15. D. L. Porter, C. E. Lahm, and R. G. Pahl, "Fuel Constituent Redistribution During the Early Stages of U-Pu-Zr Irradiation," Symp. on Irradiation-Enhanced Materials Science, TMS Fall Meeting, Chicago, IL, in press, Met. Trans. A., (September 25-29, 1988).

16. D. L. Porter, G. L. Hofman, B. R. Seidel, and L. C. Walters, "Factors Controlling Metal Fuel Lifetime," Proc. of the Intl. Conf. on Reliable Fuels, pp. 4-75 to 4-90, Tucson, AZ (1986).

Metal Fuel Performance (Contd.)

17. B. R. Seidel, G. L. Batte', C. E. Lahm, R. M. Fryer, and J. F. Koenig, "Off-Normal Performance of EBR-II Driver Fuel," Proc. of the Intl. Conf. on Reliable Fuels for Liquid Metal Reactors, pp. 6-48 to 6-66, Tucson, AZ (1986).

18. B. R. Seidel, D. L. Porter, L. C. Walters, and G. L. Hofman, "Experience with EBR-II Driver Fuel," Proc. of the Intl. Conf. on Reliable Fuels for Liquid Metal Reactors, pp. 2-106 to 2-121, Tucson, AZ (1986).

19. B. R. Seidel and L. C. Walters, "Progress in the Development of Metallic Fuel for Fast Reactors," Trans. Am. Nucl. Soc., 56, 68, San Diego, CA (June 12-16, 1988).

20. B. R. Seidel, L. C. Walters, and Y. I. Chang, "Advances in Metallic Nuclear Fuel," J. of Metals, 39(4), 11 (April 1987)

21. D. B. Tracy, S. P. Henslee, N. E. Dodds, and K. J. Longua, "Improvements in Fabrication of Metallic Fuels," Trans. Am. Nucl. Soc., 60, 314, San Francisco, CA (November 26-30, 1989).

22. T. J. Wonnell, "Characterization of Uranium-Based Alloy Fuels with Low Concentrations of Interstitial Impurities," M.S. Thesis, Univ. of California, Berkeley (August 1988).

Pyroprocessing

1. J. P. Ackerman, "Pyrochemistry of Fuel Recovery for the Integral Fast Reactor," Extended Abstract, AIChE Summer Meeting, Philadelphia, PA (August 20-23, 1989).

2. J. E. Battles and L. Burris, "The IFR Pyrometallurgical Process," Extended Abstract, AIChE Summer Meeting, Philadelphia, PA (August 20-23, 1989).

3. L. Burris, "Rekindled Interest in Pyrometallurgical Processing," Chem. Eng. Prog., 82(2), 35 (1986).

4. L. Burris, W. E. Miller, E. C. Gay, J. P. Ackerman, Zygmunt Tomczuk, J. E. Herceg, and W. J. Kann, "Update on Development of the IFR Pyroprocess," Trans. Am. Nucl. Soc., 56, 68, San Diego, CA (June 12-16, 1989).

5. L. Burris, M. Steindler, and W. E. Miller, "A Proposed Pyrometallurgical Process for Rapid Recycle of Discharged Fuel Materials from the Integral Fast Reactor," Proc. of Fuel Reprocessing and Waste Management, 2, 257, Jackson, WY (August 26-29, 1984).

6. L. Burris, R. K. Steunenberg, and W. E. Miller, "The Application of Electrorefining for Recovery and Purification of Fuel Discharged from the Integral Fast Reactor," AIChE Symp. Series, 83(254), 135 (1987).

Pyroprocessing (Contd.)

7. D. F. Fischer and T. R. Johnson, "Immobilization of IFR Salt Wastes in Mortar," Proc. Spectrum 1988, Pasco, WA (September 11-15, 1988).

8. T. R. Johnson, "Development of IFR Fuel Cycle," Proc. Sixth Annual Pyrochemical Workshop, Los Alamos, NM (October 1986).

9. T. R. Johnson, M. A. Lewis, and D. F. Fischer, "Management of IFR Wastes," Extended Abstract, AIChE Summer Meeting, Philadelphia, PA (August 20-23, 1989).

10. T. R. Johnson, M. A. Lewis, and D. F. Fischer, "Treatment of Wastes from Fuel Cycle of Integral Fast Reactors," Abstract, IAEA J., 20, Waste Management Research Abstracts (1989).

11. T. R. Johnson, W. E. Miller, and R. K. Steunenberg, "Proposed Methods for Treating High-Level Pyrochemical Process Wastes," Trans. Am. Nucl. Soc., 50, 206, San Francisco, CA (November 10-14, 1989).

12. M. A. Lewis and T. R. Johnson, "A Study of the Thermodynamic and Reducing Properties of Lithium in Cadmium at 773 K," submitted for J. of the Elec. Soc. publication (October 1989).

13. M. A. Lewis and D. W. Warren, "Gas Generation from the Irradiation of Mortar," submitted for American Ceramic Society publication (1989).

14. M. A. Lewis and D. W. Warren, "The Use of Additives for Reducing Hydrogen Yield in Mortar Containing Slag and Chloride Salts," submitted for Material Research Society publication (1989).

15. W. E. Miller, E. C. Gay, and J. E. Herceg, "Pyroprocessing Equipment and Operations for the IFR Fuel Cycle," Extended Abstract, AIChE Summer Meeting, Philadelphia, PA (August 20-23, 1989).

16. W. E. Miller, T. R. Johnson, and Z. Tomczuk, "Choice of Pyroprocess for Integral Fast Reactor Fuel," Trans. Am. Nucl. Soc., 50, 205, San Francisco, CA (November 10-14, 1985).

17. W. E. Miller, M. J. Steindler, and L. Burris, "Electrolysis Cell for Reprocessing Plutonium Reactor Fuel," U.S. Patent 4,596,647, June 24, 1986.

18. D. S. Poa, L. Burris, R. K. Steunenberg, and Z. Tomczuk, "Electrodeposition of Uranium Metal by Reduction of Uranium Oxides in Molten $LiF-KF-NaF-CaF_2-UF_4$," Extended Abstract, Electrochemical Society Fall Meeting, Hollywood, CA (October 15-20, 1989).

19. D. S. Poa, Z. Tomczuk, and R. K. Steunenberg, "Cyclic Voltammetric Study of the Reduction of Pu(III) to Plutonium Metal in Molten $LiCl-NaCl-CaCl_2-BaCl_2-PuCl_3$," Extended Abstract, Electrochemical Society Fall Meeting, Chicago, IL (October 9-14, 1988).

Pyroprocessing (Contd.)

20. D. S. Poa, Z. Tomczuk, and R. K. Steunenberg, "Cyclic Voltammetric Study of the Reduction of U(III) to Uranium Metal in Molten LiCi-NaCl-$CaCl_2$-$BaCl_2$-UCl_3," Extended Abstract, Electrochemical Society Fall Meeting, San Diego, CA (October 19-24, 1986).

21. D. S. Poa, Z. Tomczuk, and R. K. Steunenberg, "Voltammetry of Uranium and Plutonium in Molten LiCl-NaCl-$CaCl_2$-$BaCl_2$. I. Reduction of U(III) to Uranim Metal," J. of Elec. Soc., 135(5) (May 1988).

22. D. S. Poa, Z. Tomczuk, and R. K. Steunenberg, "Voltammetry of Uranium and Plutonium in Molten LiCl-NaCl-$CaCl_2$-$BaCl_2$. II. Reduction of Pu(III) to Plutonium Metal," J. of Elec. Soc. (1989) in process.

23. Z. Tomczuk, D. S. Poa, W. E. Miller, and R. K. Steunenberg, "Electrorefining of Uranium and Plutonium from Liquid Cadmium," Trans. Am. Nucl. Soc., 50, 204, San Francisco, CA (November 10-14, 1985).

Safety

1. T. H. Bauer, G. R. Fenske, and J. M. Kramer, "Cladding Failure Margins for Metallic Fuel in the Integral Fast Reactor," Trans. 9th Intl. Conf. on Structural Mechanics in Reactor Technology (SMiRT-9), C, 31, Lausanne, Switzerland (August 17-21, 1987).

2. J. E. Cahalan, "Safety Aspects of LMR Core Design," Proc. Topical Mtg. on Reactor Physics and Safety, NUREG/CP-0080, 1, 121, Saratoga, Springs, NY (September 1986).

3. J. E. Cahalan et al., "Integral Fast Reactor Safety Features," Proc. of the Intl. Topical Mtg. on Safety of Next Generation Power Reactors, 103, Seattle, WA (May 1-5, 1988).

4. J. E. Cahalan, R. H. Sevy, and S. F. Su, "Accommodation of Unprotected Accidents by Inherent Safety Design Features in Metallic and Oxide-Fueled LMFBRs," Intl. Topical Mtg. on Fast Reactor Safety, CONF-850410, 1, 29, Knoxville, TN (April 21-25, 1985).

5. L. W. Deitrich and D. P. Weber, "A Review of US Models and Codes for Analysis of Whole Core Transients and Accidents in Fast Reactors," Proc. of Conf. on the Science and Technology of Fast Reactor Safety, 1, 219, St. Peter Port, Guernsey, UK (May 12-16, 1986).

6. F. E. Dunn and D. J. Malloy, "LMR Centrifugal Pump Coastdowns," Proc. on Anticipated and Abnormal Transients in Nuclear Power Plants, VIII-21, Atlanta, GA, (April 1987).

7. F. E. Dunn, D. J. Malloy, and D. Mohr, "Liquid-Metal-Cooled Reactor Thermal-Hydraulic Calculations in the United States," Nucl. Sci. and Engng., 100(4) (December 1988).

Safety (Contd.)

8. F. E. Dunn, D. J. Malloy and D. Mohr, "LMR Thermal Hydraulics Calculations in the US," Intl. Topical Mtg. in Advances in Reactor Physics, Mathematics and Computation, 3, 1597, Paris, France, (April 27-30, 1987).

9. F. E. Dunn, F. G. Prohammer, D. P. Weber, and R. B. Vilim, "The SASSYS-1 LMFBR Systems Analysis Code," Intl. Topical Mtg. on Fast Reactor Safety, CONF-850410, 1, 999, Knoxville, TN (April 21-25, 1985).

10. G. R. Fenske, E. E. Gruber, and J. M. Kramer, "Fission Gas Retention in Irradiated Metallic Fuel," Trans. 9th Intl. Conf. on Structural Mechanics in Reactor Technology (SMiRT-9), C, 3-9, Lausanne, Switzerland, (August 17-21, 1987).

11. J. D. Gabor, R. T. Purviance, R. W. Aeschlimann, and B. W. Spencer, "Characterization of IFR Metal Fuel Fragmentation," Trans. Am. Nucl. Soc., 54, 251, Dallas, TX (June 7-11, 1987).

12. D. J. Hill, "SAS4A Validation and Analysis of In-Pile Experiments for Slow Ramp TOP's," Intl. Topical Mtg. on Fast Reactor Safety, CONF-850410, 1, 791, Knoxville, TN (April 21-25, 1985).

13. D. J. Hill, D. R. Pedersen, and J. F. Marchaterre, "Passive Safety and the Advanced Liquid Metal Reactors," 23rd Intersociety Energy Conversion Engineering Conf., 1, 473, Denver, Colorado (July 31 - August 5, 1988).

14. D. J. Hill and R. A. Wigeland, "Validation of SASSYS Core Radial Expansion Reactivity Feedback Model," Trans. Am. Nucl. Soc., 56, 380, San Diego, CA (June 12-16, 1988).

15. J. W. Holland, G. M. Teske, and J. C. Florek, "TREAT Experiment M2 Posttest Examination, " Trans. Am. Nucl. Soc., 52, 500, Reno, NV (June 1986).

16. J. M. Kramer, T. H. Hughes, and E. E. Gruber, "Validation of Models for the Analysis of the Transient Behavior of Metallic Fast Reactor Fuel," 10th Intl. Conf. on Structural Mechanics in Reactor Technology (SMiRT), C, 65, Anaheim, CA (August 14-18, 1989).

17. J. F. Marchaterre and R. J. Neuhold, "Status and Requirements of U.S. Safety R&D," Paper presented at closing session of Conf. on the Science and Technology of Fast Reactor Safety, St. Peter Port, Guernsey, UK, (May 12-16, 1986).

18. J. F. Marchaterre, R. H. Sevy, and J. E. Cahalan, "Integral Fast Reactor Concept Inherent Safety Features," ASME Winter Annual Meeting, 86-WA/NE-14, Anaheim, CA (December 7-12, 1986).

19. C. J. Mueller and J. M. Kramer, "Cladding Failure Probability Modeling for Risk Evaluations of Fast Reactors," Trans. 9th Intl. Conf. on Structural Mechanics in Reactor Technology (SMiRT-9), C, 39, Lausanne, Switzerland, (August 17-21, 1987).

Safety (Contd.)

20. C. J. Mueller and D. C. Wade, "Probabilities of Inherent Shutdown of Unprotected Events in Innovative Liquid Metal Reactors," Proc. of the Intl. Topical Mtg. on Safety of Next Generation Power Reactors, 704, Seattle, WA (May 1-5, 1899).

21. E. A. Rhodes, G. S. Stanford, and J. P. Regis et al, "Motion of IFR Metal-Alloy Fuel in TREAT Experiment M7," Trans. Am. Nucl. Soc., 56, 384, San Diego, CA (June 12-16, 1988).

22. W. R. Robinson, T. H. Bauer, A. E. Wright, E. A. Rhodes, G. S. Stanford, and A. E. Klickman, "First TREAT Transient Overpower Tests on U-Pu-Zr Fuel: M5 and M6," Trans. Am. Nucl. Soc., 55, 418, Los Angeles, CA (November 15-19, 1987).

23. B. W. Spencer, J. D. Gabor, J. C. Cassulo, and D. J. Kilsdonk, "Results of Scoping Experiments on Melt Stream Breakup and Quench," Proc. ANS Thermal Reactor Safety Mtg., 1, II8-1, San Diego, CA (February 2-6, 1986).

24. B. W. Spencer and J. F. Marchaterre, "Scoping Studies of Vapor Behavior During a Severe Accident in a Metal-Fueled Reactor," Intl. Topical Mtg. on Fast Reactor Safety, CONF-850410, 1, 151, Knoxville, TN (April 21-25, 1985).

25. A. M. Tentner et al," Analyzing Unprotected Transients in Metal Fuel Cores with the SAS4A Accident Analysis Code," Proc. of the Intl. Topical Mtg. on Safety of Next Generation Power Reactors, 799, Seattle, WA (May 1-5, 1988).

26. A. M. Tentner, G. Birgersson, J. E. Cahalan, F. E. Dunn, Kalimullah, and K. J. Miles, "SAS4A, A Computer Model for the Analysis of Hypothetical Core Disruptive Accidents in Liquid Metal Reactors," Paper presented at the 1987 Eastern Computer Simulation Conference, Orlando, FL (April 1987).

27. R. Tilbrook and D. Dever, "Comparison of Effect of Insulating Blockages on Metal and Oxide Fuel Elements," Trans. Am Nucl. Soc., 57, 151, Washington, DC (October 30-November 4, 1988).

28. R. B. Vilim, T. Y. C. Wei, and F. E. Dunn, "Generalized Control System Modeling for Liquid-Metal Reactors," Nucl. Sci. and Engng., 99, 183 (1988).

29. R. A. Wigeland and T. J. Moran, "Radial Core Expansion Reactivity Feedback in Advanced LMRs: Uncertainties and Their Effects on Inherent Safety," Proc. of the Intl. Topical Mtg. on Safety of Next Generation Power Reactors, 879, Seattle, WA (May 1-5, 1988).

30. A. E. Wright et al, "Techniques of Metal Fuel Transient Testing in TREAT," Proc. of the Intl. Topical Mtg. on Safety of Next Generation Power Reactors, 871, Seattle, WA (May 1-5, 1988).

Safety (Contd.)

31. A. E. Wright et al, "The IFR Overpower Test M7 in TREAT," Trans. Am. Nucl. Soc., 56, 383, San Diego, CA (June 12-16, 1988).

32. A. E. Wright, T. H. Bauer, R. K. Lo, W. R. Robinson, and R. G. Palm, "Recent Metal Fuel Safety Tests in TREAT," Proc. of Conf. on the Science and Technology. of Fast Reactor Safety, 2, 59, St. Peter Port, Guernsey, UK (May 12-16, 1986).

Neutronics and Core Design

1. P. J. Collins, C. A. Atkinson, W. P. Poenitz, R. M. Lell, R. W. Schaefer, and J. R. Liaw, "A Data Base for the Adjustment and Uncertainty Evaluation of Reactor Design Quantities," Proc. of the NEACRP Specialists' Meeting on Application of Critical Experiments and Operating Data to Core Design via Formal Methods of Cross Section Data Adjustment, Jackson Hole, WY, NEACRP-L-307, 77 (September 23-24, 1988).

2. P. J. Finck, "A Technique for Computing Bowing Reactivity Feedback in LMRBRs," Trans. Am. Nucl. Soc., 55, 581, Los Angeles, CA (November 15-19, 1987).

3. P. J. Finck and T. J. Moran, "Radial Expansion Feedback in LMRs: An Assessment of Neutronic Approximations," ANS 1988 Intl. Reactor Physics Conf., III, 297, Jackson Hole, WY (September 18-22, 1989).

4. R. N. Hwang, "Topics in Data Adjustment Theory and Applications," Proc. of the NEACRP Specialists' Meeting on Application of Critical Experiments and Operating Data to Core Design via Formal Methods of Cross Section Data Adjustment, NEACRP-L-307, 227, Jackson Hole, WY (September 23-24, 1988).

5. S. A. Kamal, "Three-dimensional Bowing Analysis of Radial Reflector Assemblies in Advanced LMRs," Trans. of the 10th Intl. Conf. on Structural Mechanics in Reactor Technology, E, 163, Anaheim, CA (August 1989).

6. S. A. Kamal and Y. Orechwa, "Bowing of Core Assemblies in Advanced Liquid Metal Fast Reactors," Proc. of the 1986 Joint ASME/ANS Nuclear Power Conf., 445, Philadelphia, PA (July 1986).

7. S. A. Kamal and Y. Orechwa, "Transient Bowing of Core Assemblies in Advanced Liquid-Metal Fast Reactors," Trans. Am. Nucl. Soc., 52, 648, Reno, NV (June 1986) and Proc. of the Topical Meeting of Reactor Physics and Safety, 1, 164, NUREG/CP-0080, Saratoga Springs, NY (September 1986).

8. H. S. Khalil, "Techniques for Computing Reactivity Changes Caused by Fuel Expansion in LMRs," ANS 1988 Intl. Reactor Physics Conf., III, 285, Jackson Hole, WY (September 18-22, 1989).

Neutronics and Core Design (Contd.)

9. H. S. Khalil and T. J. Downar, "Uncertainty in the Burnup Reactivity Swing of Fast Reactors," Proc. of the NEACRP Specialists' Meeting on Application of Critical Experiments and Operating Data to Core Design via Formal Methods of Cross Section Data Adjustment, NEACRP-L-307, 187, Jackson Hole, WY (September 23-24, 1988).

10. H. S. Khalil and E. K. Fujita, "The Effect of Blanket Assembly Shuffling on LMR Neutronic Performance," Trans. Am. Nucl. Soc., 55, 621, Los Angeles, CA (November 15-19, 1987).

11. H. S. Khalil, E. K. Fujita, S. Yang, and Y. Orechwa, "Fuel Management Studies of Small Metal and Oxide LMRs," ANS Topical Meeting on Advances in Fuel Mangement, 159, Pinehurst, NC (March 2-5, 1986).

12. T. J. Moran, "Core Restraint Contribution to Radial Expansion Reactivity," Proc. of the 1986 Joint ASME/ANS Nuclear Power Conf., 454, Philadelphia, PA (July 20-23, 1986).

13. T. J. Moran, "Core Restraint Design for Inherent Safety," Proc. of the 1988 Joint ASME-ANS Nuclear Power Conf., 223, Myrtle Beach, SC (April 17-20, 1988).

14. Y. Orechwa and H. S. Khalil, "Physics Implications of Oxide and Metal Fuel on the Design of Small LMFBR Cores," ANS Topical Meeting on Reactor Physics and Shielding, 323, Chicago, IL (September 17-19, 1984).

15. Y. Orechwa, H. S. Khalil, R. B. Turski, and E. K. Fujita, "Core Design and Performance of Small Inherently Safe LMRs," ANS Topical Meeting on Advances in Fuel Management, 152, Pinehurst, NC (March 2-5, 1986).

16. Y. Orechwa and Y. S. Yang, "Development of an LMR Core Design Using Metallic Fuel," ANS Intl. Conf. on Reliable Fuels for Liquid Metal Reactors, pp. 5-141 to 5-155, Tucson, AZ (September 7-11, 1986).

17. W. P. Poenitz and P. J. Collins, "Utilization of Experimental Integral Data for the Adjustment and Uncertainty Evaluation of Reactor Design Quantities," Proc. of the NEACRP Specialists' Meeting on Application of Critical Experiments and Operating Data to Core Design via Formal Methods of Cross Section Data Adjustment, NEACRP-L-307, 97, Jackson Hole, WY (September 23-24, 1988).

18. R. W. Schaefer, "Critical Experiment Tests of Bowing and Expansion Reactivity Calculations for LMRs," ANS 1988 Intl. Reactor Physics, Conf., III, 309, Jackson Hole, WY (September 18-22, 1989).

19. R. B. Vilim, "A Thermodynamic Analysis of Unprotected Steam Generator Blowdown Events in the Integral Fast Reactor," Amer. Instit. of Chem. Engrs. Heat Transfer Symp. Series, 85, 430, Philadelphia, PA (1989).

Neutronics and Core Design (Contd.)

20. D. C. Wade, "Uncertainty Reduction Requirements in Cores Designed for Passive Reactivity Shutdown," Proc. of the NEACRP Specialists' Meeting on Application of Critical Experiments and Operating Data to Core Design via Formal Methods of Cross Section Data Adjustment, NEACRP-L-307, 59, Jackson Hole, WY (September 23-24, 1988).

21. D. C. Wade, "Overview of Advanced LMR Design in the US," ANS 1988 Intl. Reactor Physics Conf., I, 159, Jackson Hole, WY (September 18-22, 1989).

22. D. C. Wade and E. K. Fujita, "Trends Versus Reactor Size of Passive Reactivity Shutdown and Control Performance," Nucl Sci. and Engng., 103, 182 (1988).

23. D. C. Wade and Y. I. Chang, "The Integral Fast Reactor Concept: Physics of Operation and Safety," Nucl. Sci. and Engng., 100, 507 (1988).

Fuel Cycle Demonstration

1. R. J. Forrester, et al., "Safety Aspects of the IFR Pyroprocess Fuel Cycle," Proc. Intl. Conf. on Safety of Nucl. Installation of the Next Generation and Beyond, Chicago, IL (August 1989) in press.

2. M. J. Lineberry, et al., "Modifications to HFEF/S for IFR Fuel Cycle Demonstration," Trans. Am. Nucl. Soc., 56, 70, San Diego, CA (June 12-16, 1988).

3. M. J. Lineberry and R. D. Phipps, "A Demonstration Facility for the IFR Fuel Cycle," Proc. Intl. Conf. Nuclear Fuel Reprocessing and Waste Mgmt., "RECOD 87," 1, 153 (1987).

4. M. J. Lineberry and R. D. Phipps, "Preparations for IFR Fuel Cycle Demonstration," Trans. Am. Nucl. Soc., 60, 170, San Francisco, CA (November 26-30, 1989).

5. R. H. Rigg, T. R. Johnson, and L. Burris, "A Waste Treatment Process for a Pyrochemical Fuel Reprocessing Facility," Proc. Intl. Mtg. Waste Mgmt. and Decon. and Decommissioning SPECTRUM '86, 2, 1755 (1986).